

University of Louisville

ThinkIR: The University of Louisville's Institutional Repository

Electronic Theses and Dissertations

5-2019

Automatic signal and image-based assessments of spinal cord injury and treatments.

Samineh Mesbah
University of Louisville

Follow this and additional works at: <https://ir.library.louisville.edu/etd>



Part of the [Biomedical Commons](#)

Recommended Citation

Mesbah, Samineh, "Automatic signal and image-based assessments of spinal cord injury and treatments." (2019). *Electronic Theses and Dissertations*. Paper 3174.
<https://doi.org/10.18297/etd/3174>

This Doctoral Dissertation is brought to you for free and open access by ThinkIR: The University of Louisville's Institutional Repository. It has been accepted for inclusion in Electronic Theses and Dissertations by an authorized administrator of ThinkIR: The University of Louisville's Institutional Repository. This title appears here courtesy of the author, who has retained all other copyrights. For more information, please contact thinkir@louisville.edu.

AUTOMATIC SIGNAL AND IMAGE-BASED ASSESSMENTS OF
SPINAL CORD INJURY AND TREATMENTS

By

Samineh Mesbah
M.Sc. Biomedical Engineering 2014

A Dissertation
Submitted to the Faculty of the
J.B. Speed School of Engineering of the University of Louisville
in Partial Fulfillment of the Requirements
For the Degree of

Doctor of Philosophy
in Electrical Engineering

Department of Electrical and Computer Engineering
University of Louisville
Louisville, Kentucky

May 2019

Copyright 2019 by Samineh Mesbah

All rights reserved

AUTOMATIC SIGNAL AND IMAGE-BASED ASSESSMENTS OF SPINAL CORD
INJURY AND TREATMENTS

By

Samineh Mesbah

M.Sc. Biomedical Engineering 2014

A Dissertation Approved On

April 23rd, 2019

By the following dissertation committee:

Dissertation Director

Ayman El-Baz, Ph.D.

Dissertation Co-Director

Tamer Inanc, Ph.D.

Susan Harkema, Ph.D.

Olfa Nasraoui, Ph.D.

Andre Faul, Ph.D.

DEDICATION

*This dissertation is dedicated to my parents
who have supported me and believed in me every step of the way.*

ACKNOWLEDGMENTS

I would like to thank my Ph.D. advisor Dr. Ayman El-Baz for his guidance and support throughout my Ph.D. program. I would also like to thank Dr. Susan Harkema for giving me the opportunity to collaborate with her team and providing valuable guidance and support over the past four years. I would also like to express my gratitude to my Ph.D. co-advisor Dr. Inanc and the other committee members Dr. Nasroaui and Dr. Faul for their valuable comments and assistance. I would like to express my gratitude to Dr. Enrico Rejc for his assistance and guidance towards completing my Ph.D. program. Also, many thanks to my dear friends Fati Sanii, Mariam Sarrafan, Maryam Mehrnezhad, Minoosoltani, Mahsa Geryloo and Marzieh Moradi for their support and inspiration. Finally, I would like to thank my family members Vajiheh Mesbah, Helya Mesbah, Saina Mortazavi and my grandmother and grandfather for their moral support, and my pets Melissa, Misha, Jessy, Barfi and Meshki for their companionship.

ABSTRACT

AUTOMATIC SIGNAL AND IMAGE-BASED ASSESSMENTS OF SPINAL CORD INJURY AND TREATMENTS

Samineh Mesbah

April 23rd, 2019

Spinal cord injury (SCI) is one of the most common sources of motor disabilities in humans with estimated annual global incidence of 40 to 80 cases per million population. The quality of life in individuals with severe and chronic SCI is often deeply impacted by the hardships of living with paralysis and high medical and living costs. Depending on the level and severity of the injury, these individuals can experience a wide range of secondary complications including muscle atrophy as a result of disuse and fat infiltration in skeletal muscles in paralyzed limbs that can lead to diabetes, cardiovascular diseases and metabolic syndrome and limit the motor function even if the neural recovery is sufficient. In recent years, spinal cord epidural stimulation (scES) along with activity-based training has shown astonishing results for re-enabling independent standing, walking over ground and voluntary movements of the paralyzed limbs in individuals with severe SCI even several years after the injury. The combination of proper parameter selection for epidural stimulation, i.e. frequency, intensity and electrode configuration, is one of the key factors in successful facilitation of the full weight-bearing standing, stepping and volitional control of lower limbs. Finding the most optimum scES

parameters selection for a given lower limb motor function in each SCI individual requires extensive assessments of muscle recruitment patterns below the injury level and their connections with the scES parameters. Furthermore, the physiological mechanism involved in performing motor tasks with scES in individuals with motor complete paralysis has remained vastly unknown.

In this dissertation, we have developed advanced engineering tools to address three distinct problems that researchers, clinicians and patients are facing in SCI research realm. Particularly, we have proposed a fully automated stochastic framework to quantify the effects of SCI on muscle size and adipose tissue distribution in skeletal muscles by volumetric segmentation of 3-D MRI scans in individuals with chronic SCI as well as non-disabled individuals. In this framework, subcutaneous adipose tissue, inter-muscular adipose tissue and total muscle tissue are segmented using linear combination of discrete Gaussians algorithm. Also, three thigh muscle groups were segmented utilizing the proposed 3-D Joint Markov Gibbs Random Field model that integrates first order appearance model, spatial information, and shape model to localize the muscle groups. The accuracy of the automatic segmentation method was tested on both SCI (N=16) and on non-disabled (N=14) individuals, showing an overall 93% accuracy for adipose tissue and muscle compartments segmentation based on Dice Similarity Coefficient. The proposed framework for muscle compartment segmentation showed an overall higher accuracy compared to ANTs and STAPLE, two previously validated atlas-based segmentation methods. Also, the framework proposed in this study showed similar Dice accuracy and better Hausdorff distance measure to that obtained using DeepMedic

Convolutional Neural Network structure, a well-known deep learning network for 3-D multi-modal MRI image segmentation.

In the second part of this research, we developed a novel framework for robust and automatic activation detection, feature extraction and visualization of the scES effects across a high number of scES parameters to build individualized-maps of muscle recruitment patterns of scES. This new method is designed to automate the current process for performing this task, which has been accomplished manually by data analysts through observation of raw EMG signals, a process that is laborious, time-consuming and prone to human errors. The proposed method provides a fast and accurate five-step algorithms framework including: conversion of the EMG signal into its 2-D representation by overlaying the located signal building blocks; de-noising the 2-D image by applying the Generalized Gaussian Markov Random Field technique; detection of the occurrence of evoked potentials using a statistically optimal decision method through comparison of the probability density functions of each segment to the background noise utilizing log-likelihood ratio; feature extraction of detected motor units such as peak-to-peak amplitude, latency, integrated EMG and Min-max time intervals; and finally visualization of the outputs as Colormap images. In comparing the automatic method vs. manual detection on 700 EMG signals from five individuals, the new approach demonstrated an average accuracy of 98.28% based on the combined false positive and false negative error rates. The sensitivity of this method to the signal-to-noise ratio (SNR) was tested using simulated EMG signals and compared to two existing methods, where the novel technique showed much lower sensitivity to SNR.

Finally, in the last part of this dissertation, we introduced an EMG time-frequency analysis framework that implements EMG spectral analysis and machine learning tools to characterize EMG patterns resulting in independent or assisted standing enabled by spinal cord epidural stimulation, and identify the stimulation parameters that promote muscle activation patterns more effective for standing. We initially compared three frequency transformations, fast Fourier (FFT), short-time Fourier (STFT) and continuous wavelet transform (CWT) and determined that CWT represent the power distribution of the EMG activities in time and frequency domains more effectively than FFT and STFT. The time-frequency features that we extracted from EMG signals have revealed that during independent standing condition, the coefficient of variation of the signal envelope, the median frequency and its standard deviation show a significant drop while the total power and mean peak power show significant increase compared to assisted standing in 11 individuals with motor complete paraplegia and 16 muscles. We then used the extracted feature vectors to classify the standing performances after performing non-negative matrix factorization for dimension reduction. Between the 4 classification methods that have been tested, K-nearest neighbor (KNN) performed better than Naïve Bayes, binary Support Vector Machine, and ensemble decision tree. We also demonstrated that the inclusion of wavelet-derived EMG frequency variables in the classification model results in an accurate classification (94.4%) of independent versus assisted standing, which is much higher than the classification accuracy that was obtained using only EMG time domain variables (83.7%). We finally applied the proposed analysis framework on EMG data collected from six research participants while they were testing the effectiveness of different stimulation parameters for standing. Although

the stimulation parameters applied did not lead to independent standing, the proposed prediction method scored effectiveness of each set of stimulation parameters tested for each muscle, based on the comparison between the EMG pattern characteristics promoted by each set of stimulation parameters and those resulting in independent standing.

The neurotechnological advancements proposed in this dissertation have greatly benefited SCI research by accelerating the efforts to quantify the effects of SCI on muscle size and functionality, expanding the knowledge regarding the neurophysiological mechanisms involved in re-enabling motor function with epidural stimulation, fast-tracking the selection of optimum stimulation parameters for performing motor tasks and consequently considerably reducing costs and labor work while helping the patients with complete paralysis to achieve faster motor recovery.

TABLE OF CONTENTS

DEDICATION.....	iii
ACKNOWLEDGMENTS	iv
ABSTRACT.....	v
LIST OF TABLES	xiv
LIST OF FIGURES	xv
CHAPTER I	
INTRODUCTION.....	1
A. Problem Statement	2
I) Effects of SCI on Skeletal Muscle Size and Functionality	2
II) Neurophysiological Mapping of Spinal Cord Epidural Stimulation	3
III) Neurophysiological Markers Predicting Independent Standing with scES	4
B. Spinal Cord Injury Overview	5
C. Quantitative Analysis of Medical Images	9
a. Medical Image Segmentation Methods	9
b. Applications of Image Segmentation in SCI Research.....	13
c. Limitations of Current Methods	14
d. Proposed Approach for MRI Segmentation	15
D. EMG Signal Processing	15
a. Time-domain Analysis	16
b. Frequency-domain Analysis	17
c. Limitations of Current Methods	20
d. Proposed Approach for Time-domain EMG Processing and Visualization	21
e. Proposed Framework for Spectral Analysis, Classification and Prediction	21

E. Dissertation Organization	22
 CHAPTER II	
NOVEL STOCHASTIC FRAMEWORK FOR AUTOMATIC SEGMENTATION OF HUMAN THIGH MRI VOLUMES AND ITS APPLICATIONS IN SPINAL CORD INJURED INDIVIDUALS	
	25
A. Introduction.....	25
a. Muscle Atrophy Assessment	26
b. Current Methods.....	26
B. Materials and Methods.....	28
a. MRI Scan Specifications and Characteristics of the Research Participants	29
b. Automatic Segmentation Framework	29
c. Segmentation Accuracy Metrics.....	37
d. Manual Segmentation, ANTs, STAPLE and DeepMedic algorithms	38
C. Results.....	40
a. Segmentation of SAT, IMAT and bone.....	40
b. Muscles Group Segmentation.....	42
c. Comparison with ANTs and STAPLE	43
d. Comparison with CNN	45
e. Comparison Between SCI and ND volumes	45
D. Discussion	47
E. Application: SCI Case study	53
F. Study Outcomes	56
 CHAPTER III	
ACTIVATION DETECTION AND COLORMAP REPRESENTATION OF EPIDURAL STIMULATION MAPPING OF SPINAL CORD.....	
	57
A. Introduction.....	57
Signal Change Detection Methods	58
B. Materials and Methods.....	60
a. Participants, Stimulation and Data Acquisition.....	60
b. Methodology.....	63
C. Results.....	77

a.	Performance Evaluation Using Manual Activation Detection	77
b.	Comparison with Other Activation Detection Methods	79
c.	Calculating Total Runtime of The Algorithms	83
D.	Discussions	84
E.	Application I: Finding optimized electrode configuration	87
F.	Application II: Repeatability Measures of Epidurally Induced Motor Evoked Potentials in Individuals with Spinal Cord Injury	90
a.	Linear Mixed-effects Models	92
b.	Comparison between Inter-Trial Variability of the Amplitude and Threshold Criteria	95
c.	Bootstrapping and Intra-class Correlation Coefficient	95
G.	Study Outcomes	97

CHAPTER IV

	Neurophysiological markers predicting independent standing enabled by spinal cord epidural stimulation	98
A.	Introduction	98
	Characteristics of Muscle Activation Patterns	99
B.	Materials and Methods	100
a.	Research Participants	100
b.	Surgical implantation of electrode array and stimulator	101
c.	Experimental Procedure	102
d.	EMG time and frequency domain analysis	104
e.	Classification	107
f.	Prediction	108
g.	Statistical analysis	110
C.	Results	111
a.	Standing motor patterns with and without scES	111
b.	Time- and frequency-domain EMG features can accurately classify assisted versus independent standing	113
c.	Physiological characteristics of muscle activation resulting in assisted or independent standing	117
d.	Ranking the effectiveness of EMG activity for standing	123
D.	Discussion	127

E. Study Outcomes	132
CHAPTER V	
CONCLUSIONS AND FUTURE DIRECTIONS.....	134
A. Conclusion	134
B. Future Directions	139
REFERENCES.....	140
CURRICULUM VITAE.....	154

LIST OF TABLES

Table 2.1 The average (\pm SD) accuracy measures (Dice’s coefficient (DC), Recall (R), and Precision (P) of the proposed fat segmentation approach for SCI (N=16) and ND (N=14) individuals.	42
Table 2.2 The average (\pm SD) accuracy measures (Dice’s coefficient (DC), Recall (R), Precision (P), and the Hausdorff distance (HD) for three methods (A1: proposed algorithm, A2: ANTs, and A3: STAPLE) for SCI and ND groups.	44
Table 3.1 Comparison with other activation detection methods. Comparison of the total accuracy for the new automated activation detection method with the TKEO and SODM methods based on five-number-summary.	80
Table 3.2 Runtime measurements. The runtime mean and RMSE of each steps of the proposed framework	84
Table 3.3. Estimated components of the total variation in $\log A$, σ , (approximate components of relative variation in A) and their 95% confidence intervals (CI) for surface and indwelling electrodes measurements.	93
Table 3.4. Estimated components of the total variation in I_t , σ , and their 95% confidence intervals (CI) for surface and indwelling electrodes measurements.	94
Table 4.1 Clinical characteristics of the research participants.	101

LIST OF FIGURES

- Fig 1.1** Exemplary MRI thigh images from axial, coronal and sagittal views of Non-disabled (left) and an individual with motor complete spinal cord injury (right) that shows the effects of muscle atrophy on the muscle size and adipose tissue distribution in the thighs after spinal cord injury..... 7
- Fig 1.2** (A) Schematic of the implanted 16-electrode array and its position on the spinal cord; (B) Activity based training positions that participants have performed after scES implant; (C) Typical recorded EMG signals from left leg muscles; and (D) Schematic of 16 leg muscles that EMG signals have been recorded from. 8
- Fig 1.3** Exemplary MRI volumes of thigh muscle in coronal, sagittal and axial views. The regions of interest are depicted with colors: Yellow: Extensor Muscles, Pink: Flexor Muscles, Red: Medial Muscles, Green: Subcutaneous adipose tissue (SAT), Dark blue: Extensors intermuscular adipose tissue (IMAT), Light blue: Flexors IMAT, and Orange: Medial IMAT. 14
- Fig 1.4** Flowchart depicting the structure of this dissertation. 23
- Fig 2.1** The proposed framework. The Block diagram of the proposed framework for muscles/fat segmentation and quantification based on MRI 3-D volumes..... 31
- Fig 2.2** An Example for applying LCDG algorithm MRI 3-D volumes. LCDG algorithm output on (a) depicts exemplary 3D FS-MRI image data; (b) probability density functions of the image voxels in Fig 2a, as determined empirically, and as approximated via LCDG using two dominant DGs; (c) the deviation (standard and absolute) between the empirical and estimated marginal probability density functions in Fig 2b; (d) LCDG algorithm output on the dominant and subordinate DGs in the image data in Fig 2a; (e) the final estimated LCDG model of the empirical density function; and (f) the final LCDG output of the conditional

probability density functions of light tissue (muscle) and dark tissue (fat) intensities and the empirical density function.....	32
Fig 2.3 Segmentation accuracy measures. (a) In the segmentation quality measurements, there are 4 regions to be considered as: True positive (TP), false positive (FP), true negative (TN), and false negative (FN). (b) The calculation of the HD between the red line X and the blue line Y.	38
Fig 2.4 Examples for the utilization of LCDG to segment the soft tissue volumes. (a) From left to right: gray scale MR images for FS+WS, WS and FS; (b) From left to right: binary mask of total thigh area, total fat and total muscle area; (c) From left to right: steps for segmenting the bone and bone marrow; (d) 3-D representations of the segmentation results for SCI (left) and ND (right) thigh; Grey: Muscle area, Yellow: SAT, Blue: IMAT, Red: bone.....	41
Fig 2.5 Examples of muscle group segmentation algorithm for four SCI subjects. (a) original cross sectional MR image; (b) automatic segmentation of muscle groups: blue area is extensor, red is flexor and yellow presents the medial compartment; (c) manually segmented muscle groups (cyan lines) overlaid on automatic segmentation for comparison; and (d) 3-D representation of automatic segmentation of muscle groups: blue volume is extensor, red is flexor and yellow presents the medial muscle group.	43
Fig 2.6 The boxplot representation of the calculated volumes and ratios for manual (black) and automatic (red) segmentation results. (a) Extensor volume; (b) Flexor volume; (c) Medial volume; (d) IMAT volume; (e) SAT volume; (f) Total muscle volume; and (g) IMAT /muscle.	46
Fig 2.7 Steps for muscle and adipose tissue segmentation of MR thigh images: (a) Top: original left and right MR thigh images, bottom: corresponding registered images; (b) Top: segmented subcutaneous fat, bottom: segmented intermuscular fat; (c) Top: bone segmentation, bottom: segmented muscle area; (d) Top: manual muscle group segmentation, bottom: automatic muscle group segmentation of left and right thigh images.	54

Fig 2.8 Comparison of the segmented volumes and volume ratios of manual (purple and orange lines) and automatic (blue and red lines) outputs for right and left thighs, respectively, at four different time points during the activity-based interventions. .	55
Fig 3.1 scES and EMG connections. Schematic representation of the epidural stimulation unit (16-electrode array, IPG unit and wireless programmer) and its connections to the EMG recording system.	62
Fig. 3.2 Block diagram of the proposed framework for visualization and activation detection of evoked potentials induced by scES.....	65
Fig 3.3 The steps for converting raw EMG signals into 2-D and 3-D images. (A) Raw EMG signal, (B) Signal segmentation using stimulation time intervals, (C) Overlaying all the segments and building the 3-D graph where X-axis is the evoked potentials duration (ms), the Y-axis is the stimulation voltage (V), and the Z-axis is the amplitude of the signals (μV) and (D) Converting the 3-D graphs into 2-D images using Colormap.....	67
Fig 3.4 EMG Denoising Using GGMRF. (A) Applying GGMRF method to 2D image (B) and an example of evoked potential before (black) and after (red) applying GGMRF method.....	69
Fig 3.5 Activation Detection. Calculation steps for activation detection algorithm. (A) A sample evoked potential (one segment of the EMG signal), (B) Histogram of the sample evoked potential (black) and its estimated Gaussian distribution (red), (C) Comparing the Gaussian pdf of evoked potential signal (red) to pdf of background noise (black), (D) Plotting the calculated LLR for all segments of the EMG signal and detect the activation threshold (arrow).....	73
Fig 3.6 Feature Extraction. Selected feature parameters for EMG activation signal. (A) Visual inspection: Number of peaks of the evoked potential, Activation onset and Latency, (B) Computer-based feature extraction of peak-to-peak amplitude (V_{pp}), Activation latency, Time interval between minimum and maximum values (T_{pp}) and Integrated EMG (summation of absolute values of all gray areas).	75
Fig 3.7 Colormap Visualization. Examples of converting 14 EMG signals into Colormap images for a voltage ramp-up and a frequency ramp-up experiment. (A) Raw EMG	

signals of 14 proximal and distal left and right leg muscles during voltage ramp-up from 0.1 to 10 V. (B) Raw EMG signals of same muscles during frequency ramp-up from 2 to 60 Hz. (C) Colormap image shows the corresponding peak-to-peak amplitudes (μV) with respect to each muscle and stimulation voltage after stimulation threshold detection. The gray area is presenting the pre-threshold part of the experiment where no activation was induced. (D) Colormap image shows the corresponding integrated EMG values with respect to 14 muscles and stimulation frequencies. 76

Fig 3.8 Performance Measures. Boxplot representation of performance measurements for comparing automated activation detection method with the manual ground truth. (A) Accuracy, (B) Sensitivity, (C) Specificity, (D) Dice Similarity 78

Fig 3.9 Examples of recorded EMG signals with high, medium and low SNRs and the performance comparison between three activation detection methods. (A) high SNR signal from right MH; (B) medium SNR signal from right GL and (C) low SNR signal from L GL. Detected activation windows for AGLR + MMGRF, AGLR and TKEO from left to right are shown as continuous and dashed black lines. De-noised signal is shown in light red and manually detected activation window as dashed red line..... 82

Fig 3.10 Comparison of the proposed activation detection algorithm with two other methods. Comparison of three activation detection methods, TKEO, SODM, and SODM with GGMRF on simulated signals as a function of SNR (dB). 83

Fig 3.11 Functional application of scES mapping and visualization technique. (A) Colormap figures for middle column configurations for 2 selected muscles (left and right RF and VL) used to identify optimal configurations for voluntary activity (knee extension) in a research participant. The white area in the images shows that at which stimulation voltage the experiment started and the gray area shows the pre-threshold part of the experiments. (B) SBP data with respect to stimulation configurations when the R VL muscle is off (left) and when it is on (right) (C) stick figure representing movement. (D) Successful but not optimal configuration designed for knee extension (E) Optimized configuration for knee extension. In the

graphical representation cathodes are black, anodes are graph and assigned electrodes are white..... 89

Fig 3.12 The recruitment curves of left VL, MH, TA and SOL muscles of Trial #1 and Trial #2 amplitude and threshold values with stimulation configuration (A) 5-//6+ rostral part of the electrode array; (B) 8-//7+ middle part of the electrode array; (C) 10-//9+ caudal part of the electrode array; (D) 4-/10-/15-//0+/5+/11+ wide-field configuration. 92

Fig 4.1 (A) The spinal cord epidural stimulation and its location on the human spinal cord; (B) Schematic view of the standing task; (C) Example of the recorded EMG signal from left SOL during one minute of assisted standing and (D) Independent standing. 104

Fig 4.2 Electromyography (EMG), hip and knee joint angle, and ground reaction forces recorded form research participant A59 during: (A) sit-to-stand transition and standing with external assistance for hips and knees extension (assisted standing) without spinal cord epidural stimulation (scES); (B) sit-to-stand transition and independent standing using scES. The participant held the hands of a trainer for balance control; (C) assisted standing with scES resulting from an overall continuous activation pattern (top) and from an EMG pattern characterized by the alternation of EMG bursts and little activation. Stimulation amplitude, frequency and electrode configuration (cathodes in black, anodes in red, and inactive in white) are reported for each participant. In **B**, the participant was stimulated with 3 programs delivered sequentially at 15 Hz, resulting in an ongoing 45 Hz stimulation frequency. EMG was recorded from the following muscles of the right lower limb: IL, iliopsoas; GL, gluteus maximus; MH, medial hamstring; VL, vastus lateralis; TA, tibialis anterior; SOL, soleus. 112

Fig 4.3 (A) Exemplary images of assisted standing (left) and independent standing (right). (B) EMG activity recorded from the left soleus (L SOL) of research participant A45 during assisted standing (left) and independent standing (right) with epidural stimulation, and related spectral power density calculated by Fast Fourier Transform (FFT), Short-Time Fourier Transform (STFT) and Continuous Wavelet

Transform (CWT) are plotted. Stimulation amplitude, frequency and electrode configuration (cathodes in black, anodes in red, and inactive in white) are reported 114

Fig 4.4 (A) The first three dimensions of standing data points (blue: independent standing; red: assisted standing) after normalization, dimension reduction and logarithmically transforming the EMG spectral feature vectors extracted from CWT, STFT and FFT. (B) Classification accuracy for feature vectors extracted from CWT, STFT and FFT and (C) classification accuracy for the combination of time features and CWT-extracted features versus time features only, when considering all muscles, all muscles except IL, flexor muscles, extensor muscles, and each muscle (left and right), separately. 116

Fig 4.5 (A) EMG signal recorded from left MH muscle during assisted standing with alternating bursting pattern; (B) EMG signal recorded from left MH muscle during assisted standing with continuous pattern; (C) EMG signal recorded from left MH muscle during independent standing with continuous pattern; (D-F) Low frequency envelopes of EMG signals presented in A-B; (G-H) Contour plots of the wavelet scalogram calculated for EMG signals presented in A-B; (J-L) Instantaneous median frequency feature extracted from the scalogram of EMG signals presented in A-B. 118

Fig 4.6 Paired statistical comparisons among individuals that achieved both standing with assisted and independent knees extension while their hip was assisted based on extracted total power, pattern variability, maximum power variability, average median frequency and median frequency standard deviation. Hip assisted (hA); knee assisted (kA); knee independent (kI). 120

Fig 4.7 Paired statistical comparisons among individuals that achieved standing with assisted and independent knees extension while hip was assisted, and independent hip and knees extension based on extracted total power, pattern variability, maximum power variability, average median frequency and median frequency standard deviation. Hip assisted (hA); hip independent (hI); knee assisted (kA); knee independent (kI). 121

- Fig 4.8** Paired statistical comparisons for standing with assisted and independent knees extension based on extracted total power, pattern variability, maximum power variability, average median frequency and median frequency standard deviation. Knee assisted (kA); knee independent (kI). 122
- Fig 4.9** Recorded EMG signals from left SOL during assisted (A) and independent (B) standing conditions, their 25 milliseconds zoomed-in view (C and D) and the corresponding instantaneous median frequency values (E and F). (G) Exemplary Morlet wavelet signals with high (40 Hz) and low (20 Hz) central frequencies (f_c). 123
- Fig 4.10** Two representative features (total power and median frequency) of the EMG data sets used to train assisted (red) and independent (blue) standing KNN models are plotted against each other for each investigated muscle. Trends of assisted and independent standing data points are overall similar across muscles, while the distribution pattern shows some inter-muscle variability (i.e. between SOL and TA). EMG data collected from 6 individuals during a total of 48 standing events aimed at testing the effectiveness of different stimulation parameters (green stars) were then fed to the prediction algorithm. While all these attempts resulted in assisted standing, the related EMG data points are spread across the plots, with some of them partially overlapping independent standing data points..... 125
- Fig 4.11** Ranking of individual muscle performances presented as colormaps (shades of red related to assisted standing and shades of blue related to independent standing). (A) Examples of two assisted standing events from subject A68 with 0.14 total prediction score (left) and 0.48 total prediction score (right). (B) Examples of two independent standing events from subject B30 with 0.81 total prediction score (left) and 0.97 total prediction score (right). (C) Examples of two partially assisted (one knee assisted and one knee independent) standing events from subject A60 with 0.28 total prediction score (left) and 0.50 total prediction score (right). 127

CHAPTER I

INTRODUCTION

This dissertation is focused on proposing neurotechnological advancements in the spinal cord injury (SCI) research domain by designing and implementing engineering tools that can facilitate and therefore accelerate the efforts towards assessment of SCI effects on size and functionality of skeletal muscles in humans with severe and chronic SCI. These tools can also help in expanding the knowledge regarding the neurophysiological mechanism involved in using electrical stimulation of the spinal cord for motor recovery in individuals with chronic complete SCI. This chapter of the dissertation is dedicated to address the motivations and the three distinct objectives of this dissertation followed by an overview of the SCI research and epidural stimulation of the spinal cord as the potential treatment for individuals with chronic SCI and the importance of advancing signal and image-based machine learning techniques to facilitate the rehabilitation process in this population. The previous studies that have been done in the medical image segmentation literature and electromyogram (EMG) signal processing techniques in machine learning domain and their limitations will be presented and our proposed approach to overcome them will be offered. The structure of the rest of this dissertation will be presented at last. By the end of this chapter, the reader will be familiarized with the purpose and objectives of this research and will have basic

understanding about the SCI research and the signal and image-based tools that are proposed to address some of the problems that researchers in this field are facing.

A. Problem Statement

In this dissertation, as a collaborative work with Kentucky Spinal Cord Research Center, we are targeting three distinct problems in the area of SCI research. The following subsections are presenting the motivation behind each problem and the specific objective that is going to be addressed in this dissertation.

I) Effects of SCI on Skeletal Muscle Size and Functionality

Motivation

Spinal cord injury is one of the leading causes of paralysis in the United States responsible for 27.3% of the population living with paralysis [1]. The prolonged disuse of the paralyzed limbs often leads to skeletal muscle deterioration and adipose tissue infiltration in individuals with chronic SCI. These negative adaptations can cause secondary complications such as diabetes, cardiovascular diseases and metabolic syndrome as well as limiting motor functions even if the neural recovery is sufficient. Therefore, it is crucial to quantify the effects of SCI on the size of the skeletal muscles and adipose tissue volumes and assess the efficacy of interventions that can help prevent or reverse these adaptations. The 3-D magnetic resonance images (MRIs) of the human thighs has been used traditionally for qualitative assessments of skeletal muscle and fat volumes. These images can be segmented into desired compartments to quantify the size of each muscle or muscle group volumes and the fat distribution in between the muscles. Although manual segmentation of muscle MRI volumes can be performed with high

accuracy, this method is laborious and lacks scalability as the number of subjects, image slices and regions of interest grow.

Objective

Automatic methods for medical image segmentation are the solution to quantitative imaging scalability problem. Therefore, the objective here is to develop a fully automated system that can segment each slice into extensor, flexor and medial muscle groups, bone, inter-muscular and subcutaneous adipose tissues and measure the volumes of each compartment and their ratio. Specifically, the challenges of shape-based segmentation of MRI scans when there exists limiting or no intensity differences between the shapes of interest, as well as high level of shape variability between subjects in SCI population will be addressed.

II) Neurophysiological Mapping of Spinal Cord Epidural Stimulation

Motivation

Although there is currently no cure for SCI, in recent years, spinal cord epidural stimulation (scES) along with activity-based training has shown promising results for regaining non-assisted standing, walking over ground and voluntary movements of the paralyzed limbs in individuals with severe SCI even several years after the injury. It has been shown that proper selection of stimulation parameters, i.e. electrode configuration, intensity and frequency, plays a significant role in successful facilitation of volitional movements and performing independent motor tasks. To achieve optimum parameter selection, the first step is the mapping of the muscle recruitment patterns using motor evoked potentials induced by scES. The detection of the evoked potentials inside the

recorded EMG signals and visualize the connections between the characteristics of the muscle response and the stimulation parameters is a challenging task and designing a tool that addresses this problem can significantly accelerate the process of searching for proper parameter selection.

Objective

The objective here is to develop a signal processing framework that can detect motor evoked potentials accurately from recorded EMG signals and visualize the process of mapping the motor pathways below the injury level and their connections with scES parameters. The challenge in accurately detecting evoked potentials in EMG signals is that the signal to noise ratio of the recorded EMG is unknown and varies between different muscles and experiments and the developed activation detection method has to be robust to the variation of the noise level in the signals.

III) Neurophysiological Markers Predicting Independent Standing with scES

Motivation

The ability to stand with independent lower limb extension is a key achievement towards the recovery of functional mobility in individuals with motor complete SCI and can subsequently lead to recovering over ground stepping and walking. It is known that the appropriate selection of individual-specific scES parameters is crucial to promote standing with independent lower limb extension in this population. However, to date there are no available algorithms or procedures that suggest the exact set of parameters to be applied for facilitating standing using tonic scES. Moreover, the characteristics of

muscle activation patterns leading to independent standing has remained poorly understood.

Objective

Finding the scES parameters that would lead to independent standing requires: 1) Extracting physiologically meaningful features from the recorded EMG signals and understanding what are the physiological characteristics of the lower limb muscle responses that lead to independent standing; 2) Designing computational models that can accurately discriminate between assisted and independent standing conditions for each muscle based on the extracted features; and 3) Using these models to predict if a set of scES parameters can lead to independent standing based on the muscle responses generated. One challenge here is to define the best neurophysiological features that can provide high level of differentiability between the two standing conditions while advancing the researchers knowledge of which neurophysiological conditions are responsible for independent standing in SCI population. The second challenge is to design the best classification and prediction framework that can classify the feature vectors with high accuracy and therefore provide accurate predictions regarding the stimulation parameters that can lead to independent extension in targeted muscles.

B. Spinal Cord Injury Overview

The human spinal cord is a collection of 31 pairs of nerves that are extended from the base of the brain down to the back. These nerves carry the signals from the brain that control the limbs, chest, and abdomen muscle functions and the function of organs such as heart, lungs, bowel and bladder. Spinal cord is very sensitive to injury and it does not have the ability to repair itself if damaged. Although protected by the bone structure of

vertebrae, spinal cord can be injured if the vertebrae are broken or dislocated due to trauma (the most common cause of SCI), compression from tumor or infection, or lack of blood supply. Injuries to the spinal cord can disrupt the communication between brain and the organs and body parts and lead to paralysis below the level of injury.

There are approximately 285,000 individuals currently in the United States living with SCI and about 17,700 new cases of SCI each year [2]. The average lifetime costs of each SCI patient can vary between 1,130,000 to 4,800,000 USD depending on the age at the time of injury, neurological level of injury, education and pre-injury employment [2]. Given the high costs and the hardships of living with disabilities caused by SCI, any potential treatment that can fully or partially offers recovery of motor abilities in the paralyzed limbs and/or improves cardiovascular and bladder functions is of great interest and importance.

Depending on the neurological level of the injury, SCI patients can also suffer from a wide range of acute and chronic secondary health-related complications. These secondary complications include respiratory, cardiovascular, urinary and bowel complications, spasticity, pain syndromes, pressure ulcers, osteoporosis and bone fractures [3]. Many patients experience severe muscle atrophy, bone loss and adipose tissue infiltration in the paralyzed limbs after SCI as a result of muscle disuse. Muscle atrophy can result in reduced metabolic rate and increase the risk of cardiovascular diseases and metabolic disorders such as type-2 diabetes [4, 5]. Figure 1.1 shows the effects of muscle atrophy on the thigh muscle and fat distributions using 3-D MRI images.

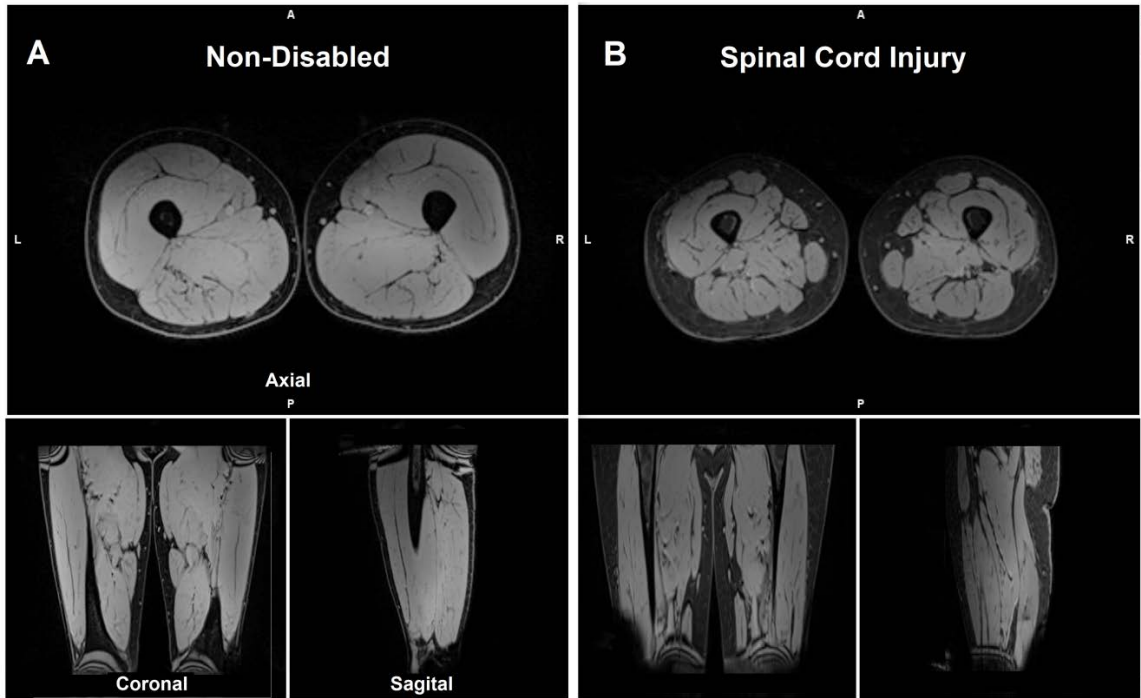


Fig 1.1 Exemplary MRI thigh images from axial, coronal and sagittal views of Non-disabled (left) and an individual with motor complete spinal cord injury (right) that shows the effects of muscle atrophy on the muscle size and adipose tissue distribution in the thighs after spinal cord injury.

Muscle atrophy can also severely limit motor function even if the recovery of neural control is sufficient to activate the muscle. Therefore, after the patient with SCI is stabilized, most of the rehabilitation efforts are focused on improving the functional level by physical and occupational therapies.

One of the potentially promising treatments for SCI that has offered promising results in recent years is the electrical stimulation of the lumbosacral spinal cord followed by extensive activity-based training, which has shown progressively re-enabling full weight-bearing standing and stepping [6, 7] [8-12] and volitional control of lower limbs in individuals with chronic motor complete paralysis [13, 14]. In this method, a 16-electrode

array was surgically implanted at the T11–L1 vertebral levels over the spinal-cord segments L1–S2 (Fig 1.2 A). The electrode array is connected to a pulse generator unit that is implanted in a subcutaneous abdominal pouch and sends stimulation pulses to the spinal cord [10]. Figure 1.2 B shows some of the positions in which participants have performed various motor tasks with spinal cord epidural stimulation (scES) after implantation. The EMG signals are recorded from 16 leg muscles (8 on each side) during the performance of motor tasks with scES (Fig 1.2 C and D). This study has been pioneered and led by Prof. Susan Harkema, the director of the Kentucky Spinal Cord Research Center at University of Louisville.

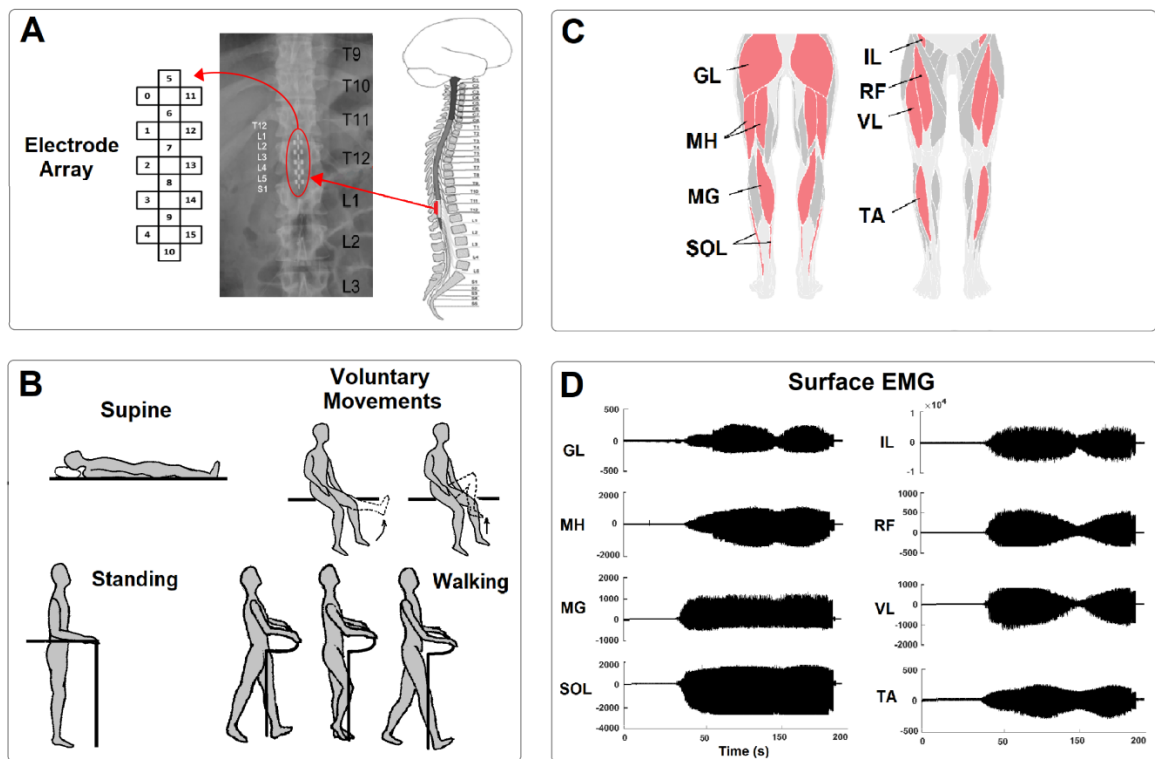


Fig 1.2 (A) Schematic of the implanted 16-electrode array and its position on the spinal cord; (B) Activity based training positions that participants have performed after scES

implant; (C) Typical recorded EMG signals from left leg muscles; and (D) Schematic of 16 leg muscles that EMG signals have been recorded from.

C. Quantitative Analysis of Medical Images

Developments of medical imaging techniques such as Computer Tomography and Magnetic Resonance Imaging (MRI) have offered great assistance in clinical diagnosis and monitoring treatments progress for various medical conditions. The automated quantitative analysis of medical images has provided effective tools for reliable assessment of medical conditions while reducing the analysis time and labor work and improving the accuracy and scalability in numerous medical applications [15].

a. **Medical Image Segmentation Methods**

The segmentation of various regions of interest in medical images is one of the crucial steps in quantitative analysis of medical images. The algorithms for performing automatic and semi-automatic segmentation tasks are classified into 4 main sub-categories according to their principal methodologies, namely the ones based on thresholding, classification or clustering techniques, deformable models and deep learning methods. These categories indicate progressive efforts towards more accurate and fully-automated medical image segmentation and the wide variety of methods that have been proposed in the literature can fit into these 4 categories.

Thresholding Methods

The first category is comprised of the simplest forms of image analysis based on intensity thresholds. Most of the algorithms that belong to this category make the assumption that the interested structures can be distinguished by image intensity or gradient magnitude

[16]. These methods look for pixels that satisfy the rules defined by the thresholds that have been selected manually using expert's knowledge or automatically through statistical modeling of the intensity distribution of images. The algorithms in this category use edge detection [17] or region detection [18] or a hybrid of both [16, 19]. Region growing algorithms use initial seeding and expand the region of interest based on the intensity of the neighboring pixels and homogeneity criteria until the total region is segmented [16, 20]. Post-processing steps such as morphological operations to connect the breaks in the detected edges or eliminate the holes in the segmented regions are often required for the outputs of these algorithms in the presence of noise and intensity inhomogeneity [16].

Pattern Recognition-based Methods

Supervised classification and unsupervised clustering methods based on pattern recognition techniques have also been used widely for segmentation in medical image applications. Main supervised classification algorithms include active appearance models support vector machines (SVM) and artificial neural networks (ANN) [21-23].

A training dataset, which includes the original and segmented images, is required for the algorithm to derive and learn nonlinear and complex patterns exist in the data. The extracted patterns from the training set provides important cues about the structures of the region(s) of interest such as intensity, position and shape, which can be then be used for the segmentation of test images. Algorithms based on classifiers have been widely applied to segment organs in medical images like cardiac and brain images. These methods are often sensitive to initial conditions and the number of training images and can be prone to overfitting [16].

Fuzzy C-means (FCM) and K-means algorithms [24], Iterative self-organizing data analysis technique algorithm [25] and unsupervised neural networks [26] are some of the popular unsupervised clustering algorithms. Instead of using a training dataset, these algorithms extract structural features from the classified points. The FCM algorithm is an iterative method that minimizes the intra-cluster variation while labelled pixels are assigned to the nearest clusters and the cluster centroid will then be updated and the labels are reassigned [24]. Unsupervised neural networks are based on unsupervised learning where the targets are the same as the inputs [16].

Deformable Models

The algorithms in the third category are based on deformable models which can be further categorized into parametric and geometric models. The parametric deformable models are made of initial contours and by using a moving equation, the contours would be driven to the boundaries of the object of interest while the external energy aims to drive the contour to the right direction based on prior image information. It can be proven that the balancing equilibrium of the moving contour under external and internal forces is the position of object's boundary. Compared to pattern recognition methods, deformable models are more flexible and can be used for complex segmentation tasks [16]. The Snake method is the first deformable model applied to the medical image segmentation [27]. Later developments aimed at minimizing the sensitivity of this algorithm to initial conditions and noise effects [28, 29].

The geometric deformable models are based on the level set method. The level set method is based on moving the contour implicitly into a higher dimensional level set function and view the contour as its zero-level set. Therefore, we can track the zero-level

set of the level set, instead of tracking the contour points. In the medical image segmentation, choosing parametric or geometric model depends on the applications: if structures have large shape variety or complicated topology, geometric deformable models are preferred; on the other hand, if the interested regions have open boundaries or the structures are thin or real-time processing is required, parametric models are preferred. Deformable models usually contain certain number of parameters and proper parameter selection is crucial to find the best performance but the task of finding optimum parameters for deformable models is usually time-consuming [16].

Deep Learning

The field of quantitative assessments of medical images and particularly the segmentation task has been significantly impacted in recent years by the emergence of deep learning neural networks. The increased access to large amounts of data, known as big data, availability of software and algorithms, and an explosion of compute power have enabled the use of deep neural networks [30]. The deep learning networks, and particularly the convolutional neural networks (CNNs), have started to outperform most of the other machine learning methods on several image analysis benchmarks [31]. Being able to extract complex features from the raw data, CNNs have also bypassed the tedious task of feature engineering [30]. The outperformance of deep neural networks however, comes with several costs and limitations such as an increased number of adjustable network parameters, substantial memory and computational costs and the black box nature of deep networks that make the debugging task and understanding the networks computational limitations very difficult [32-35]. Moreover, deep learning networks require substantial amount of training data in order to be properly trained. This can be a limitation in

medical applications in which the medical condition is not common and collecting large amount of data is not an easy task. Furthermore, in most medical applications, the manually selected features often provide researchers insights about the physiological and anatomical properties of a given condition which is critical for designing the next steps in the research or treatment. Therefore, having a network that can learn its own features, however powerful, would not always be an attractive choice for clinicians and researchers and might be a drawback in using deep neural networks in medical applications.

b. Applications of Image Segmentation in SCI Research

Magnetic resonance imaging (MRI) has been used by clinicians for examining the effects of SCI on skeletal muscle and adipose tissue distribution and determining the effectiveness of subsequent rehabilitative interventions for preventing or reversing muscle atrophy and adipose tissue expansion. Segmenting key muscle groups, such as knee extensors and flexors, and evaluating their volumes and ratios at different stages post SCI and during the progress of a given intervention in MR images is an important and delicate task that requires the expertise of a trained examiner in order to be done as accurately as possible. The regions of interest in a typical 3-D MRI volume are depicted in Fig 1.3. In addition to manual segmentation, different automatic and semi-automatic segmentation methods for MR images have been proposed in the literature. A concise background review of the automatic methods that are developed for the thigh MRI scans segmentation tasks in various medical applications has been presented in Chapter 2 of this dissertation.

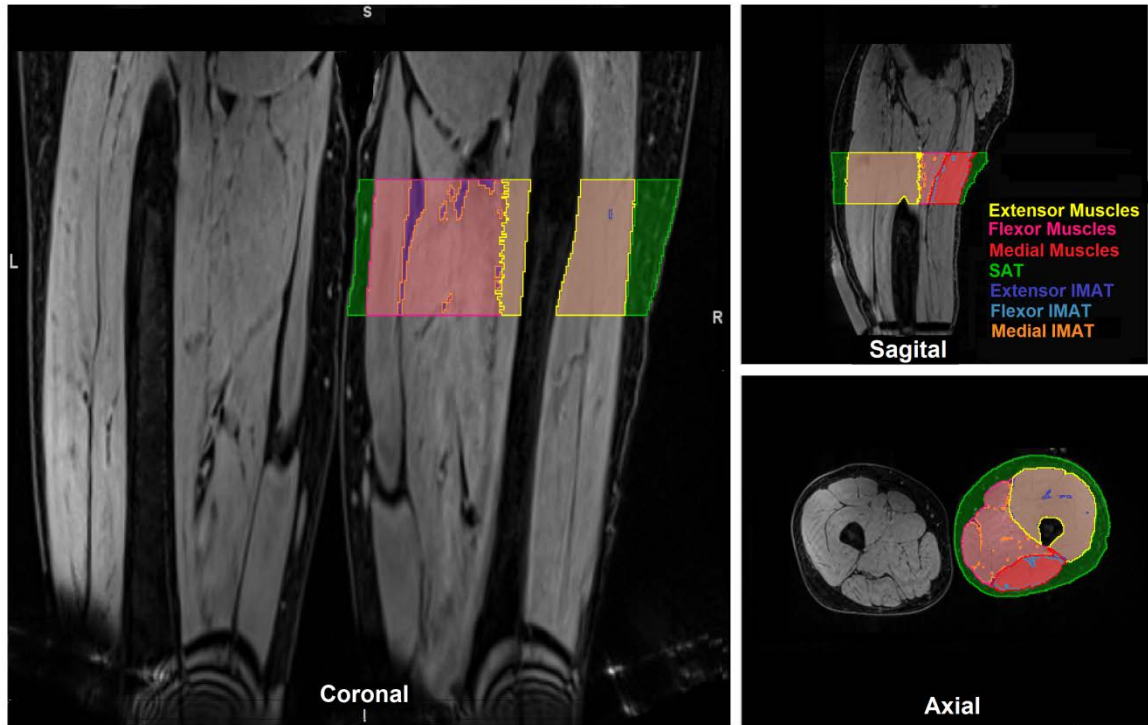


Fig 1.3 Exemplary MRI volumes of thigh muscle in coronal, sagittal and axial views. The regions of interest are depicted with colors: Yellow: Extensor Muscles, Pink: Flexor Muscles, Red: Medial Muscles, Green: Subcutaneous adipose tissue (SAT), Dark blue: Extensors intermuscular adipose tissue (IMAT), Light blue: Flexors IMAT, and Orange: Medial IMAT.

c. Limitations of Current Methods

Although the manual segmentation of the thigh muscles and adipose tissue is known to be the gold standard, it presents limitations such as being laborious, time consuming, prone to inter-examiner variability and finally lacking scalability to high numbers of MRI slices and longitudinal studies. Despite the relevant developments reported in the literature for automatic and semi-automatic segmentation methods, there has been no explicit segmentation framework proposed for the SCI population that can accurately segment

muscle groups like knee extensors and flexors, which play a key functional role, and quantify the distribution of adipose tissues around and within the thigh muscle volumes.

d. Proposed Approach for MRI Segmentation

For automatic segmentation of thigh muscles and adipose tissue in SCI population, we have proposed a novel step-wise stochastic framework for volumetric thigh segmentation of subcutaneous adipose tissue, inter-muscular adipose tissue and muscle compartment tissues utilizing an intensity-based algorithm and our proposed Joint Markov Gibbs Random Field model that integrates first order appearance model, spatial information, and shape model to localize the muscle groups. This methodology addresses the challenges in automatic segmentation of structures in the absence of intensity differences and the high level of variability in the prior shape information. The details of the methodology and applications of the proposed framework has been discussed in Chapter 2.

D. EMG Signal Processing

The EMG signal is a recording of a series of electrical activities that originate from skeletal muscles. These electrical activities are the sum of electrophysiological variations in the state of muscle fiber membranes as a result of the excitability through neural control that lead to depolarization and repolarization which results in generation of an action potential [36]. EMG signals are often recorded during isotonic and isometric muscle contractions. In isotonic contraction, the length of the muscle changes during resistance and can be further sub categorized into concentric (shortening) and eccentric (lengthening) contractions. On the contrary, isometric contraction creates no change in muscle length but causes muscles to produce force while the posture is in static position.

Analysis of EMG during isometric contractions is more commonly used for physical rehabilitation, whilst isotonic contractions are more common for strength and athletic studies. EMG signals are used extensively in SCI research in order to characterize muscle activation during the performance of various tasks as well as evaluating the effects of epidural stimulation on the muscles. Although recorded EMG signals carry useful information about the state of the muscles and their neural drives, these signals require advanced processing in time and frequency domains to locate and extract proper features.

a. Time-domain Analysis

Time-domain features for EMG signal analysis include the analysis of the signal amplitude (mean, standard deviation and coefficient of variation of the envelope), the total power of the signal (or root mean square value), entropy, number of zero-crossings, integrated EMG, and the onset and offset of increase in the muscle activity (bursts) during performing various motor tasks [37]. In the context of epidural stimulation, a challenging task in EMG analysis in the time domain is the precise detection of each epidurally evoked potential. This task is crucial in order to determine the effective threshold for epidural stimulation intensity that triggered the occurrence of the first visible evoked potential for each muscle. The motor evoked potential detection is usually performed manually by a trained observer visually inspecting the raw EMG signals, which is considered to be the gold standard for activation detection.

Change Detection Methods

There have been several computer-based methods proposed in the literature for change detection in EMG signals, such as the single or double threshold detector [38], Teager–Kaiser Energy Operation [39-41], wavelet template matching [42], supervised and

unsupervised learning algorithms [43] or statistical criterion determination methods like hidden Markov models [44] and Gaussian mixture models [45, 46]. The main goal of all these methods is to convert the original raw signals into a set of estimated sequences that make the highest distinction between before and after change as well as detect the occurrence of the change and the corresponding time instant, t_0 , as early as possible [45]. These methods can be divided into four main stages: pre-processing, conditioning, decision thresholding, and post processing. The type of test function; the decision rule, which involves the selection of constant or dynamic thresholds; and the heuristic constraints for the final detected onset, which varies based on the application and the characteristics of the EMG signals, vary between different methods.

b. Frequency-domain Analysis

Transforming the EMG signal to frequency domain provides information about the frequency content of the signal. Fast Fourier transform (FFT) has been traditionally used to analyze EMG signals in frequency domain. Mean, median and peak frequencies are some of the well-known features that can be extracted from FFT output, known as power spectral density (PSD). However, FFT has issues such as assuming stationarity for the EMG signal, not being localized in time and having poor time resolution, so that it is not suited for representing efficiently abrupt changes in the signal. The short-time Fourier transform (STFT) was designed to increase the time resolution of FFT by selecting a fixed-size moving window and take the FFT for each segment; however, STFT may have poor resolution in time and/or frequency domains, depending on the window size. On the other hand, wavelet transform (WT) guarantees high time and frequency resolutions by decomposing the signal using numerous multi-resolution wavelets [47, 48]. WT can

accurately characterize the short time component within non-stationary signals, providing information regarding the power distribution of the signal in time and frequency domains [49]. These advantages have made WT an attractive choice for analyzing the frequency content of the muscle response during performance of a task. The wavelet transform has been used in numerous studies to detect localized muscle fatigues during muscle contractions [49-51]. Particularly Karlsson et al. [52] had compared CWT with other time-frequency transformation, including STFT, and found that CWT is the most reliable method for analysis of non-stationary biological signals. Other studies had discussed the effectiveness of using the Wavelet transform to identify muscle fatigue as an automated process [50-53]. The instantaneous mean and median frequencies, peak power and peak frequency are examples of useful features that can be extracted from continuous WT outputs.

EMG Classification and Prediction Methods

The EMG signal-based control systems are an ongoing research especially in the area of rehabilitation [37]. While analysis of EMG signals has been used widely for classification of neuromuscular diseases [54] and muscles fatigue [55], a growing body of work is dedicated to analyzing EMG for controlling assistive robotic devices such as exoskeletons and lower-limb orthoses [56, 57]. The task of classification of the recorded EMG signals with high accuracy has been the main goal of these studies. Attaining better classification performance often comes hand in hand with selecting best features from the EMG signals. The feature extraction process involves the transformation of raw EMG signals into a feature vector that best describes the information that can be used for discriminating between different conditions or finding new patterns. Studies have

reported that an ensemble of time- and frequency domain features result in better classification performance [58]. Using high number of features or time varying features often result in high dimensionality of feature vectors and redundancy problem. Therefore, dimension reduction methods are required to reduce the dimensionality of the data while maintaining discrimination capability of the feature vectors. Dimension reduction methods can be divided into two main categories: feature projection and feature selection. Feature projection attempts to determine the best combination of the original features to form a new feature set that do not present redundant information; and feature selection selects best subset of the original feature vector based on a certain criteria [56, 59]. The feature vectors extracted from the EMG signals will be then fed into classifier to discover the underlying patterns. The classifier then assigns a certain class or category to the test data and measure the score (likelihood) of the new data points belonging to a given class, which is known as the prediction step. Several techniques are used to classify EMG data such as artificial neural networks (ANN), Bayesian classifier, fuzzy logic, multilayer perceptron (MLP), support vector machines (SVM), linear discriminant analysis (LDA), hidden Markov models, K-nearest neighbor (KNN) method, decision tree, random forests and ensemble methods [37]. In a study done in 2013 by Phinyomark et al. the performance of LDA, random forests, decision tree, KNN, SVM and MLP neural networks was compared for the classification task of ten upper limb motions in which LDA method had presented the best performance with 98.87% accuracy. Another study has shown near 99% classification accuracy by using MLP to classify human forearm motions based on time-frequency domain features [60]. It has been argued by Xie et al.

that the training time of ANN classifiers is quite long and determining the proper size and structure of the network is arduous and time-consuming [36].

c. Limitations of Current Methods

In the change detection task, manual detection of muscle activation is a laborious task when facing a large stack of data recorded from several muscles during various experiments. It can also be prone to human errors and inter/intra-observer variation and would also limit the ability to allow scalability to a high number of patients. Therefore, accurate computer-based method for activation detection process is crucial. Moreover, in every activation detection method, sensitivity to the noise level in the signal is a great challenge. Selection of proper pre- and post-processing methods usually helps to minimize the effect of noise on the accuracy of the method. It is also notable that some of the proposed methods in the literature are highly dependent on prior information of the signal, i.e. supervised methods, which makes those methods semi-automatic and their accuracy application-dependent.

In the frequency domain, finding a transform that can best represent the frequency content of the muscle response to epidural stimulation is challenging. Furthermore, finding relevant neurophysiological features that can provide insights regarding the epidural stimulation mechanism of activating the motor units is a significant task that has not been addressed before in SCI research.

Moreover, the analysis of EMG signals in the epidural stimulation context involves combining the neurological (muscle response to stimulation) and kinesiological (muscle response to performance of a motor task) characteristics of EMG. Developing the best classification and prediction approach that would assess the motor performance and

suggest stimulation parameter adjustments that can improve the performance, is of great interest and importance in this field and has not been addressed in prior studies.

d. Proposed Approach for Time-domain EMG Processing and Visualization

In this dissertation, we proposed a novel automatic framework for building individualized maps of scES induced muscle activation patterns while addressing the two main challenges that a fully automated activation detection method faces, by proposing an unsupervised and on-line approach that deals with the stochastic characteristics of the EMG signals in the scES application. Our generalized framework: 1) effectively denoises, detects, and extracts key features from EMG signal; 2) visualizes the occurrence of the muscle evoked potentials induced by scES; and, 3) increases the accuracy and efficiency of the physiological mapping process in order to determine the underlying relationships between the scES parameters and muscle activations. Consequently, this framework will offer a unique visualization tool that suggests stimulating which part of the stimulation array will lead to selective activation of lower limb muscles. This technique assists experimentalists to prompt decisions on further adjustments or improvements in designing future experiments.

e. Proposed Framework for Spectral Analysis, Classification and Prediction

To discover neurophysiological patterns in the motor responses to the epidural stimulation that lead to independent motor performance in individuals with complete SCI, we have compared three frequency transforms (FFT, STFT and CWT) of EMG signals recorded from lower limb muscles to extract time- and frequency domain features that best characterize muscle response to the stimulation. Furthermore, we have developed a

machine learning framework that can classify the performance of the standing task (assisted versus independent) using the extracted features. The algorithm is further advanced to predict the performance of each individual muscle during stimulation parameter testing and therefore predict which stimulation parameters has the potential to result in independent standing for each individual.

Finally, we suggest that integrating the information provided by our individualized maps of motor activation patterns promoted by scES and the prediction outputs of the second framework provides a powerful tool for finding optimum stimulation parameters selection.

E. Dissertation Organization

The structure of this dissertation is depicted as a flowchart in Fig 1.4. In this dissertation, we are targeting three problems in the SCI research domain: 1) Evaluation of muscle size and the adipose tissue distribution prior to epidural stimulation intervention; 2) Quantification and visualization of muscle recruitment patterns of epidural stimulation; and 3) Determining the characteristics of EMG signals that lead to independent standing with scES and predicting the standing performance given a set of stimulation parameters.

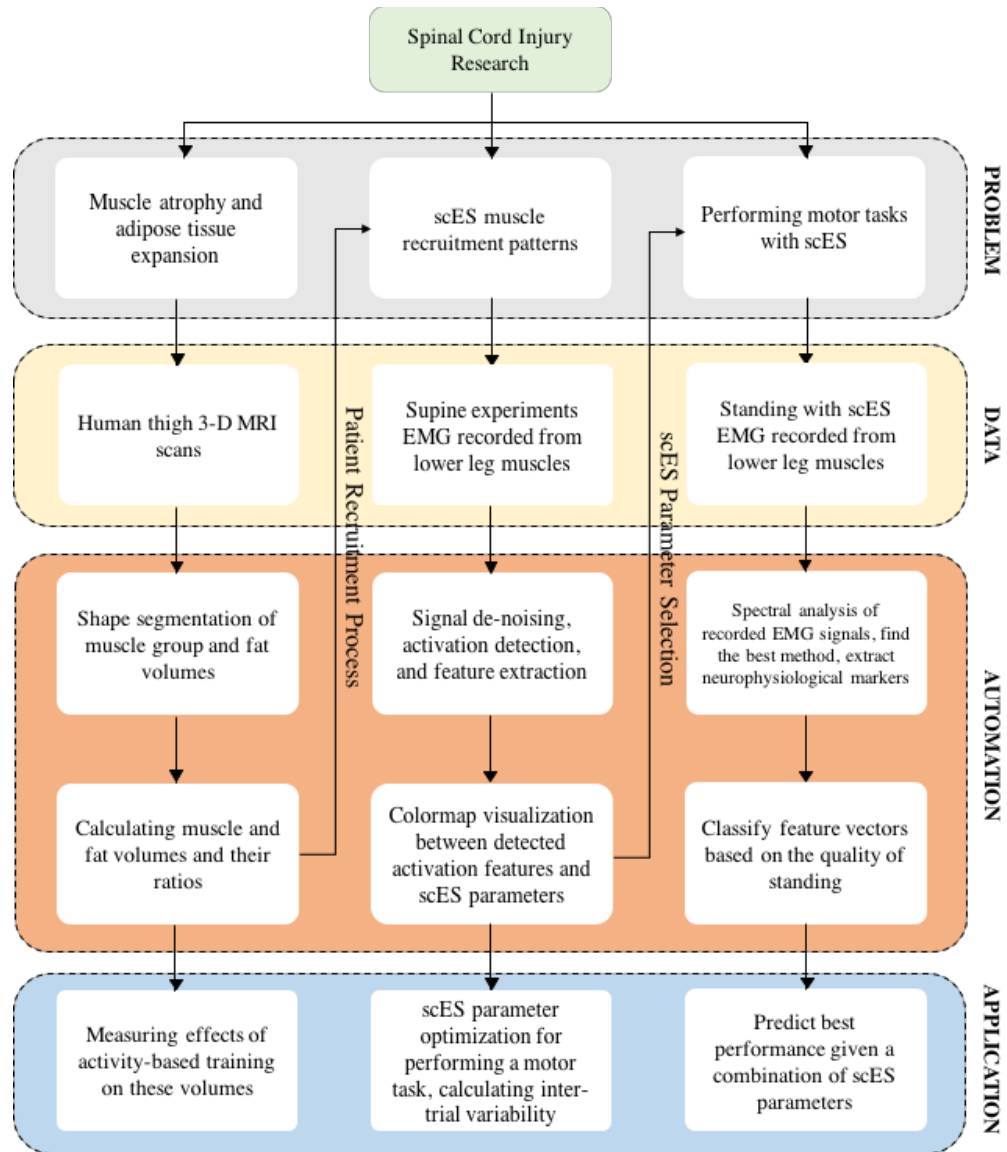


Fig 1.4 Flowchart depicting the structure of this dissertation.

In this flowchart, the three areas that are the focus of our research are divided into four main stages: defining the problem, the data that has been collected to address the problem, the automation process that is the main focus of this dissertation and finally the applications of the developed methodology for each problem. The flowchart also shows that the three problems addressed in the area of SCI research are interconnected. Particularly, the evaluation of muscle size and adipose tissue distribution is one of the

factors that need to be assessed during the patient recruitment process for epidural stimulation implant. Furthermore, the mapping of scES muscle recruitment patterns is needed for finding the proper stimulation parameters adjustments during the performance of various motor tasks.

In Chapter 2 of this dissertation, the details of the proposed framework for automatic segmentation of muscle groups and adipose tissue in MRI thigh volumes are presented. The application of using this framework to track the effects of activity-based training on the muscle volumes of a case study is also discussed in this chapter. Chapter 3 is dedicated to present the details of our work in time-domain EMG signal analysis including the novel framework for de-noising, activation detection and visualization of motor evoked potentials in order to determine muscle recruitment patterns of scES; the clinical application of using the outputs of our framework to find the optimum electrode configuration for performing voluntary knee flexion in a SCI subject, and finally measuring the amount of the inter-trial variability of recorded motor evoked potentials induced by epidural stimulation. The details of the time-frequency analysis of the recorded EMG signals using Wavelet transform and its applications in classification and prediction of standing performance with scES are presented in Chapter 4. Finally, the last chapter of this proposal is dedicated to conclusion and future directions both in the signal processing and the image processing parts of the SCI project.

CHAPTER II

NOVEL STOCHASTIC FRAMEWORK FOR AUTOMATIC SEGMENTATION OF HUMAN THIGH MRI VOLUMES AND ITS APPLICATIONS IN SPINAL CORD INJURED INDIVIDUALS

A. Introduction

Spinal cord injury (SCI) is one of the primary causes of motor disabilities in humans, with an annual incidence of approximately 17700 new cases only in the United States [2]. Skeletal muscles experience deleterious physiological changes after SCI. Animal studies showed that spinal cord transection reduced muscle mass of hind-limb extensors between 20% and 40% in one month [61-63]. Individuals with chronic SCI also showed cross-sectional area of the whole thigh, knee extensors and plantar flexors that were about 30% smaller compared to non-disabled individuals [64, 65]. In addition, SCI leads to fat infiltration within the muscle (intramuscular adipose tissue) and between muscles (intermuscular adipose tissue, IMAT) [65, 66]. The consequences of severe SCI-induced adaptations on skeletal muscle are two-fold: on one side, the muscle mechanical output is compromised, both in terms of force exertion and fatigue resistance [67, 68], which could limit motor function even if the recovery of neural control was sufficient. Additionally, the concurrent loss of muscle tissue and gain of ectopic (i.e. non-subcutaneous) adipose tissue can favor health-related complications such as pressure ulcer, glucose intolerance, insulin resistance and therefore type II diabetes, metabolic syndrome and cardiovascular

disease [65, 66]. However, these negative muscle adaptations can be mitigated by proper interventions that include neuromuscular electrical stimulation, dietary programs and assisted movement trainings [69, 70].

a. Muscle Atrophy Assessment

Magnetic resonance imaging (MRI) is a suitable method for examining the effects of SCI and determining the effectiveness of subsequent rehabilitative interventions on skeletal muscle and adipose tissue distribution, because of its multiple forms of contrast weighting and its sensitivity to diffusion, perfusion, and chemical composition of tissues [71]. In particular, determining the SCI- and intervention-induced adaptations in functional key muscle groups, such as knee extensors and flexors, is important for understanding if appropriate muscle volume and ratio between key muscle groups are present at different stages post SCI, as this can affect motor function. Also, MRI can provide useful information for understanding ectopic adipose tissue-related adaptations after SCI and different interventions in order to optimize prevention of SCI-induced health complications. For example, individual characteristics of SCI such as the level of spasticity may influence ectopic adipose tissue distribution as well as skeletal muscle size [72]. Similarly, it is important to evaluate the effects of different interventions (i.e. dietary planning; activity-based training) in order to understand their efficacy and select the most appropriate ones for reducing ectopic adipose tissue and thus contributing to prevent SCI-induced health complications.

b. Current Methods

It is important to recognize that manually assessing these parameters from MR images presents some relevant limitations, as manual segmentation is laborious, time-consuming, impractical for large studies, and can make the estimated indices subjective to the inter-rater variability to some extent. To overcome these issues, different automatic segmentation methods of MRI images were proposed in the literature. Automatic segmentation of the MR thigh images started with the work of Barra et al. [73, 74] by using intensity differences between tissues to segment the total muscle and fat areas in elderly population and it was further advanced by others to segment subcutaneous adipose tissue (SAT), IMAT and bone areas in obese populations [16, 75]. More recently, various algorithms were proposed to use prior shape information to segment individual thigh muscles in healthy population and individuals with chronic obstructive pulmonary disease [76-78]. Automatic and semi-automatic atlas-based methods using image registration algorithms for muscle segmentation have gained more attention recently to segment quadriceps individual muscles and muscle group in healthy individuals [79, 80]. There have also been longitudinal studies on the human thigh muscles using the semi-automatic segmentation methods in individuals with osteoarthritis and those with muscular dystrophy [81, 82].

The field of segmentation and quantitative assessments of medical images has been considerably impacted in recent years by the emergence of deep learning neural networks. In particular, two and three-dimensional Convolutional Neural Networks (CNNs) have shown promising results in various medical imaging fields including several recent studies on segmentation of bone and cartilage in MRI thigh and knee scans [32, 83-86]. However, there are several limitations and additional requirements needed

for the application of CNNs on 3-D medical images segmentation, such as an increased number of adjustable network parameters, substantial memory and computational costs, and the need of high-level engineering expertise to properly perform training and testing steps for pre-designed networks [32-35].

Despite the relevant developments regarding the automatic segmentation and quantitative assessments of medical images that have been reported in the literature, there has been no explicit automatic segmentation framework proposed for the SCI population that can accurately and efficiently segment muscle groups like knee extensors and flexors, which play a key functional role, and quantify different types of adipose tissue such as SAT and IMAT. In the present study, we propose a novel stochastic method that integrates intensity, spatial information and shape model to separate fat volumes from the muscle tissue and segment the muscle tissue into three compartments (knee extensors, knee flexors and a medial compartment including the adductor muscles), utilizing the Joint Markov Gibbs Random Field (MGRF) model. In order to test the accuracy of this method, we have applied the proposed framework on both a group of individuals with chronic SCI and a group of non-disabled (ND) individuals, comparing the automatic segmentation outcomes to those obtained from manual segmentation. Moreover, we have also compared the outcomes generated from our novel three-fold stochastic method with those obtained from two other well-known atlas-based techniques in order to highlight the potential improvements brought about by our approach. Finally, the thigh muscle and fat segmentation task was also performed using a well-known CNN architecture to evaluate the advantages and limitations of deep learning approach for this application.

B. Materials and Methods

a. MRI Scan Specifications and Characteristics of the Research Participants

In this work, the 3-D MRI scans were acquired using Siemens 3T Magnetom Skyra with pulse sequence – t1 vibe (for 3-D VIBE images) for in phase, opposite phase, water, and fat imaging. The volume dimensions (X, Y, Z) are 320 by 208 by 320 and the series length is 1. Voxel dimensions (X, Y, Z) are 1.5 x 1.5 x 1.5 mm, size of series point is 0.006 seconds and the slice gap is equal to zero. The thigh MRI scans analyzed in this study were collected from a total of 30 participants including 16 individuals with chronic SCI and 14 ND subjects. The characteristics of the 16 individuals with severe chronic SCI were the following: age (year): 32.4 ± 9.1 ; time since injury (year): 6.7 ± 7.7 ; 13 males and 3 females; 10 individuals classified as American Spinal Injury Association (ASIA) impairment scale (AIS) A, 5 individuals as AIS B, and 1 individual as C as for the International Standards for Neurological Classification of Spinal Cord Injury [87]; height (m): 1.78 ± 0.09 ; weight (kg): 77.19 ± 12.48 ; body mass index (BMI) (kg/m^2): 24.36 ± 3.99 . The 14 ND subjects included in this study presented were 11 males and 3 females with age (year): 28.47 ± 3.8 ; height (m): 1.80 ± 0.10 ; weight (kg): 92.56 ± 15.30 ; BMI (kg/m^2): 28.54 ± 4.27 . All participants were fully informed about the aims of the study and written consent was provided from all individuals, which was approved by the University of Louisville Institutional Review Board. All research activities were performed in accordance with the guidelines and regulations of this Institutional Review Board.

b. Automatic Segmentation Framework

A 3-D stochastic framework for fat suppressed (FS) and water suppressed (WS) MRI muscles and fat segmentation is proposed in Fig 1. The proposed system consists of a

preprocessing step to prepare the data for automatic segmentation, which includes bias-field correction, extraction of the central 50 slices between greater trochanter and lateral epicondyle of the femur, and cropping and resizing the MRI images to include only one thigh for further processing steps. The automatic segmentation part is divided to 4 steps. In the first step, which is devoted to fat and muscle area segmentation, the sum of WS and FS volumetric MRI is utilized to get the mask of the whole thigh volume and the bone marrow area utilizing Linear Combination of Discrete Gaussians (LCDG) algorithm [88]. The same method was used on each FS-MRI volume to initially extract muscle volume and WS-MRI volume to segment the total adipose tissue. Moreover, SAT was separated from IMAT by overlaying the muscle tissue mask, obtained from the FS volume, on the total fat segments from the WS volume. In the second step, each greyscale muscle volume and its manually segmented muscle groups (training dataset) are co-aligned to a reference dataset using a 3-D cubic B-splines-based approach (described in [89]) to account for the anatomical differences of each patient's extracted muscle volumes. The third step consisted in implementing a joint Markov model that simultaneously maximizes the likelihood estimation of three components: Appearance-based shape (muscles anatomy), spatial (second order appearance) and intensity (first order appearance) models by using iterated conditional modes to localize and segment three muscle groups (knee extensors, knee flexors and the medial compartment, which includes Sartorius, adductor longus, gracilis, adductor brevis, and adductor magnus muscles) for the test subjects. The fourth and last step consisted in quantifying the effects of SCI on human thigh muscles by calculating the volume of the segmented tissues. More details about the joint Markov model will be discussed in the following sections.

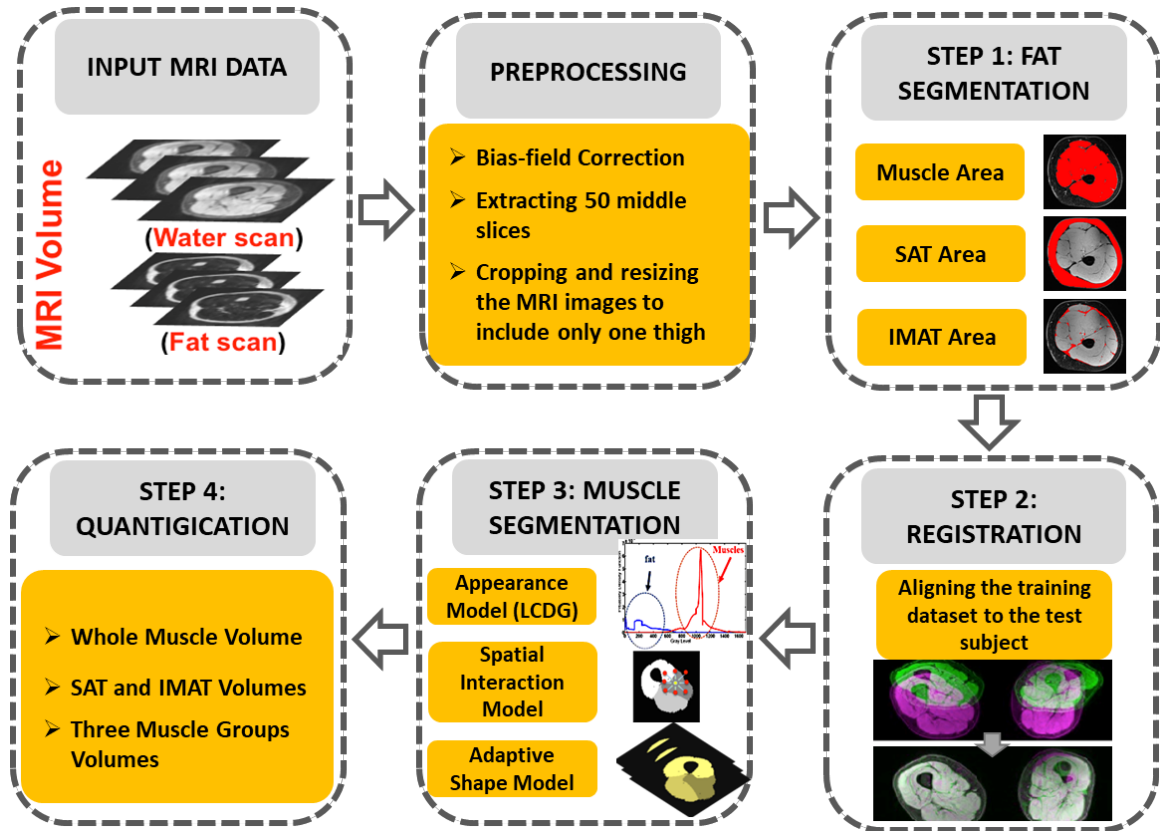


Fig 2.1 The proposed framework. The Block diagram of the proposed framework for muscles/fat segmentation and quantification based on MRI 3-D volumes.

I. Linear Combination of Discrete Gaussians (LCDG)

The main objective of LCDG is to find the threshold for each gray volume that extracts the 2 classes (corresponding to the dark tissues, and light tissues) from their background. In case of FS-MRI scans (Fig 2a), the dark tissues represent the fat and the light tissues represent the muscles area (vice versa for WS-MRI scans). At the end of the LCDG step, we get two probabilities for each voxel of the input volumes: P1 which is the probability of belonging to class 1 (dark tissue) and P2 which is the probability of belonging to class 2 (light tissue). The voxel-wise LCDG probability, will be combined

to obtain the muscle, SAT and IMAT areas from FS, WS and FS+WS MRI scans. For example, Fig 2 illustrates the steps of the muscle area segmentation using LCDG algorithm for FS-MRI volumes. Figure 2b shows the initial approximation of the bimodal empirical distribution of $Q = 256$ grey levels over a typical FS-MRI volume of human thigh. The dominant modes represent the brighter muscles area and its darker background (fat area). After the additive and subtractive parts of the absolute deviation are approximated with the DG mixtures, the initial mixed LCDG-model consists of the 2 dominant, 4 additive and 4 subtractive DGs (brown curves), as shown in Fig 2c and d). Finally, the estimated LCDG as well as conditional LCDG models of the two classes (i.e. muscles and fat tissues) are illustrated in Fig 2e and f. This algorithm is also used for WS-MRI scans to segment the fat tissue and FS+WS to segment the whole thigh mask and the bone.

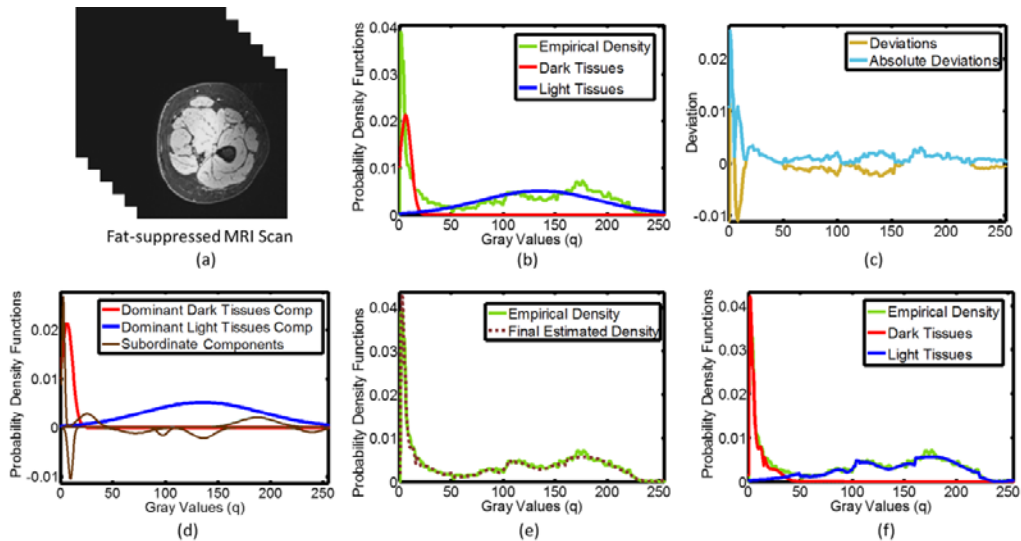


Fig 2.2 An Example for applying LCDG algorithm MRI 3-D volumes. LCDG algorithm output on (a) depicts exemplary 3D FS-MRI image data; (b) probability density functions

of the image voxels in Fig 2a, as determined empirically, and as approximated via LCDG using two dominant DGs; (c) the deviation (standard and absolute) between the empirical and estimated marginal probability density functions in Fig 2b; (d) LCDG algorithm output on the dominant and subordinate DGs in the image data in Fig 2a; (e) the final estimated LCDG model of the empirical density function; and (f) the final LCDG output of the conditional probability density functions of light tissue (muscle) and dark tissue (fat) intensities and the empirical density function.

II. Joint Markov Gibbs Random Field Model

In order to divide the extracted muscles area into various groups, a registered-to-reference database of grayscale volume, \mathbf{g} , of the muscle groups area and its map, \mathbf{m} , are described with a joint probability model: $P(\mathbf{g}, \mathbf{m}) = P(\mathbf{g}|\mathbf{m})P(\mathbf{m})$, which combines a conditional probability distribution of the input volume given the map $P(\mathbf{g}|\mathbf{m})$, and an unconditional probability distribution of maps $P(\mathbf{m}) = P_{sp}(\mathbf{m})P_V(\mathbf{m})$, where, $P_{sp}(\mathbf{m})$ represents an adaptive shape prior and $P_V(\mathbf{m})$ is a Gibbs probability distribution with potentials \mathbf{V} , which denotes a sample of a 3D MGRF model of \mathbf{m} [90].

Appearance-based Shape Model

In order to reduce the variability across subjects and enhance the segmentation accuracy, an adaptive shape model of each muscle group is employed. To create the shape database, a selected training set of volumes, collected from manually segmented subjects, are registered to a reference dataset using a 3-D B-splines-based transformation that is previously developed [89]. The selection for training dataset has been done based on the 2-D correlation coefficient (number between 0 and 1) between the grayscale images of the manually segmented volumes and the test slices. If the average correlation

coefficient for the whole volume is more than or equal to 0.5, that dataset will be selected for training otherwise it will be rejected. After selection, the training volumes are registered to the reference volume. Therefore, for each new test subject, an individual training set is built to help with variability reduction for muscle group segmentation.

In summary, each source volume f (i.e., each of the training subjects) is aligned to the reference template g on a domain $\Omega \subset R^3$ by using a non-rigid registration. Given a certain source f , the registration estimates the deformation field T for all $x \in \Omega$, by displacing a sparse grid, $\Omega' \subset \Omega$ of control points, ζ :

$$\mathbf{T}(x) = x + \sum_{\zeta \in \Omega'} \zeta(\|x - \zeta\|)\Delta\zeta \quad (2.1)$$

where $\Delta\zeta$ is the displacement vector of the control point ζ and the weighting function $\zeta(\cdot)$ measures the contribution of any control point in Ω' to the displacement of a point in Ω . The goal is that the deformation field minimizes the point-wise dissimilarity between the target g and the deformed source f :

$$E(\mathbf{T}) = \frac{1}{|\Omega'|} + \sum_{\zeta \in \Omega'} \frac{\phi(g(x), f(\mathbf{T}(x)))}{\zeta(\|x - \zeta\|)} dx \quad (2.2)$$

where ϕ is the dissimilarity function (we used the sum of absolute differences). The objective function in Eq. (2.2) is minimized using a Markov random field model of displacements of the control points ζ [90]. The dense displacement field is then determined from the control point displacements through representing free form deformations via cubic B-splines. We have selected this method because it is fully automated (no manual initialization or hand-picked landmarks) and has low computational time. More details can be found in [89, 90].

The probabilistic shape priors are spatially variant independent random fields of region labels, as follows:

$$P_{sp}(\mathbf{m}) = \prod p_{sp:x,y,z}(m_{x,y,z}) \quad (2.3)$$

where $p_{sp:x,y,z}(l)$ is the voxel-wise empirical probabilities for each label $l \in \mathbf{L}$. To segment each input MRI data, an adaptive process guided by the visual appearance features of the input MRI data is used to construct the shape prior. This shape prior consists of four labels: the 3 muscle groups and the background. In the training phase, we use N-1 (N number of subjects) manually segmented data sets by an MRI expert to create the probabilistic maps for the four labels. For the testing phase, each test MRI volume is registered using the same approach in [89], to the training sets used to create the discussed shape prior.

Spatial Interaction (Second-Order Appearance Model)

In order to overcome noise effects and to ensure segmentation homogeneity, spatially homogeneous 3D pair-wise interactions between the region labels are additionally incorporated in the proposed segmentation model. These interactions are estimated using the Potts model, i.e., an MGRF with the nearest 26-neighbors of the voxels (also known as cliques), and analytic bi-valued Gibbs potentials, that depend only on whether the nearest pairs of labels are equal or not. The utilized second-order 3D MGRF model of the region map \mathbf{m} is defined as:

$$P_V(\mathbf{m}) = \frac{1}{Z_{v_s}} \exp \sum_{(x,y,z) \in R} \sum_{(x',y',z') \in v_s} V(\mathbf{m}_{x,y,z}, \mathbf{m}_{x+x',y+y',z+z'}) , \quad (2.4)$$

where Z_{v_s} is the normalization factor. Let $f_{\text{eq}}(\mathbf{m})$ denote the relative frequency of equal labels in the neighboring voxel pairs. The initial region map results in an approximation with the following analytical maximum likelihood estimates of the potentials [91]:

$$v_{\text{eq}} = -v_{\text{ne}} \approx 2f_{\text{eq}}(\mathbf{m}) - 1, \quad (2.5)$$

which allows for computing the voxel-wise probabilities $p_{\mathbf{v}:x,y,z}(l)$ of each label; $l \in \mathbf{L}$. More details are in [88].

Intensity (First-Order Appearance) Model

Our approach also accounts for the visual appearance of the muscles besides the learned shape model and the spatial interactions. Therefore, an intensity-based model using LCDG with positive and negative DG sub-components is applied to improve the initially obtained segmentation accuracy. The role of LCDG is to accurately approximate the empirical gray level distribution of FS-MRI voxel intensities with combination of dominant and subordinate DGs for each label (muscle group). This approximation adapts the segmentation to the changes in appearance, such as non-linear intensity variations caused by different IMAT distributions between muscle groups. At the end of this stage, each grayscale voxel existing in the target volume was mapped to a class with the highest occurrence probability.

Algorithm I: The proposed muscles group segmentation approach

For each input FS and WS MRI volumes with grayscale volume g :

- a) Use LCDG to initially extract muscle volume from adipose tissue and
-

bone.

- b) Select atlas volumes using 2-D correlation coefficient measure between the training database and the target volume.
 - c) Use non-linear registration to transpose selected atlas volumes' voxels to the reference volume space.
 - d) Form an initial region map m using the marginal estimated density and prior shape of each muscle group label.
 - e) Find the Gibbs potentials for the MGRF model from the initial map.
 - f) Approximate the marginal intensity distribution $P(g|m)$ of each muscle group using LCDG.
 - g) Improve the region map m by assigning each voxels to a class with the highest probability density based on its gray value.
-

c. Segmentation Accuracy Metrics

To evaluate the results, we calculated the segmentation accuracy compared to the ground truth (obtained from manual segmentation) using Dice similarity coefficient (DC)

[92], Recall ($R = \frac{TP}{TP+FN}$), Precision ($P = \frac{TP}{TP+FP}$) and the Hausdorff distance (HD) [93].

The DC measures the concordance between two enclosed volumes as follows

$$DC = \frac{2TP}{FP+2TP+FN}, \quad (2.6)$$

where FP represents the number of false positive (i.e. the total number of the misclassified voxels of the background), FN is the number of false negative (i.e. the total number of the misclassified voxels of the object), and TP is the true positive (i.e. total number of the correctly classified pixels), as shown in Fig 2.3 a and b. On the other hand,

The HD is defined as:

$$HD(X, Y) = \max\{\sup_{x \in X} \inf_{y \in Y} d(x, y), \sup_{y \in Y} \inf_{x \in X} d(x, y)\} \quad (2.7)$$

where X and Y are the boundaries of two different volumes. It measures how far two subsets of a metric space are from each other, as shown in Fig 3b. High DC, R, P and a low HD are desirable for good segmentation.

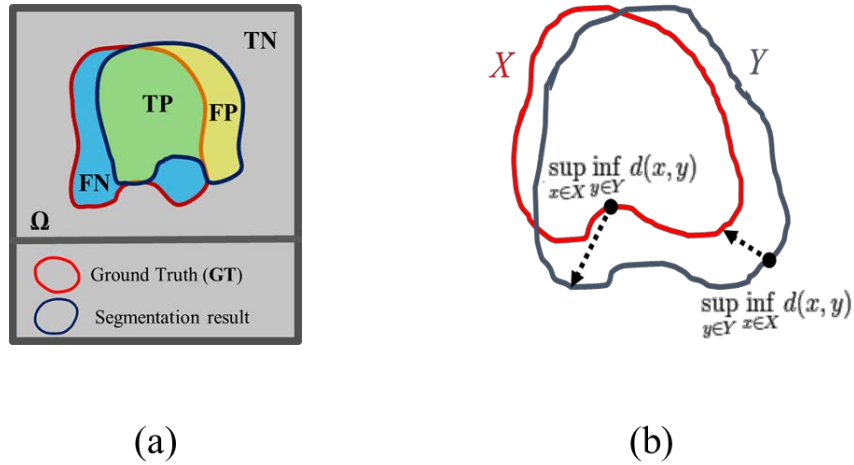


Fig 2.3 Segmentation accuracy measures. (a) In the segmentation quality measurements, there are 4 regions to be considered as: True positive (TP), false positive (FP), true negative (TN), and false negative (FN). (b) The calculation of the HD between the red line X and the blue line Y .

d. Manual Segmentation, ANTs, STAPLE and DeepMedic algorithms

Manual segmentation of MR images were performed by one expert operator using MANGO software (Research Imaging Institute, UTHSCSA) for determining SAT, IMAT, whole muscle, and the 3 muscle compartments considered in this study.

To compare the proposed method (A1) with other automatic segmentation alternatives, MRI volumes are subsequently segmented using: (A2) an atlas based segmentation

approach using ANTs registration algorithm [94]. In this technique, to estimate accurate mapping between the same structures/tissues of each atlas subject and the test one, the nonlinear Symmetric Normalization (diffeomorphic metric mapping algorithm) has been used to obtain such a 3D deformation fields that will be applied for the corresponding labeled subject. Finally, a majority voting classifier is used to fuse the aligned atlas subjects into the final automatic segmentation. The second method (**A3**) is known as simultaneous truth and performance level estimation (STAPLE) described in [95, 96]. This algorithm considers a collection of segmentations (atlas subjects) and computes a probabilistic estimate of the final segmentation. All atlas MRI scans are aligned to the target scan and the obtained deformation fields are applied to the counterpart segmentation. The fused final segmentation is formed by estimating an optimal combination of the aligned atlas subjects incorporating a prior model for the spatial distribution of structures being segmented as well as spatial homogeneity constrains.

The total thigh MRI segmentation framework was also performed with a pre-designed CNN architecture known as DeepMedic network [32], which was initially designed for segmentation of brain lesions in 3-D multi-modal MRI images. This network structure won the SISS-ISLES 2015 segmentation challenge [97]. We followed the implementation steps as recommended by the developers in order to achieve the network's best segmentation performance for segmenting SAT, IMAT, bone and three muscle compartments. To calculate the total accuracy of the DeepMedic network, we used three-fold validation method by training the network with 20 3-D MRI scans, including both SCI and ND thigh scans, and testing on the remaining 10 scans and then swapping

between training and testing groups to assess the automatic segmentation results for all scans.

The manual segmentation and the proposed framework were run on a PC with 3.60 GHz, Core i7 CPU and 16.0 GB RAM. The ANTs and STAPLE algorithms were run with 3.0 GHz Core i7 Quad CPU processor and 64GB RAM. Both computers had Windows 10 OS, MATLAB R2015b and C++ programs. The CNN code was run on both 3.50 GHz, 12 Core CPU with 256.0 GB RAM and NVIDIA 1070 Ti GPU with Linux OS and Python and TensorFlow programs.

C. Results

a. Segmentation of SAT, IMAT and bone

Figure 4 shows examples of the LCDG results on the sum of WS- and FS-MRI volumes, WS-MRI volumes and FS-MRI volumes (Fig 4a) for extraction of the whole thigh, whole fat, whole muscle mask (Fig 4b) as well as bone area (Fig 4c). Also, an example of 3D visualization of the final thigh segmentation results for SCI and ND is reported in Fig 4d. As explained in the methodology section, the SAT and IMAT areas were separated by using the whole muscle area as a mask on the whole fat area.

The average accuracy of the initial segmentation of fat tissue was tested by comparison of the automatic results with the manual segmentation of SAT, IMAT and thigh muscle. The comparison was made based on calculating the DC, R and P as accuracy measures. The average values of these three accuracy measures are presented in Table 1.

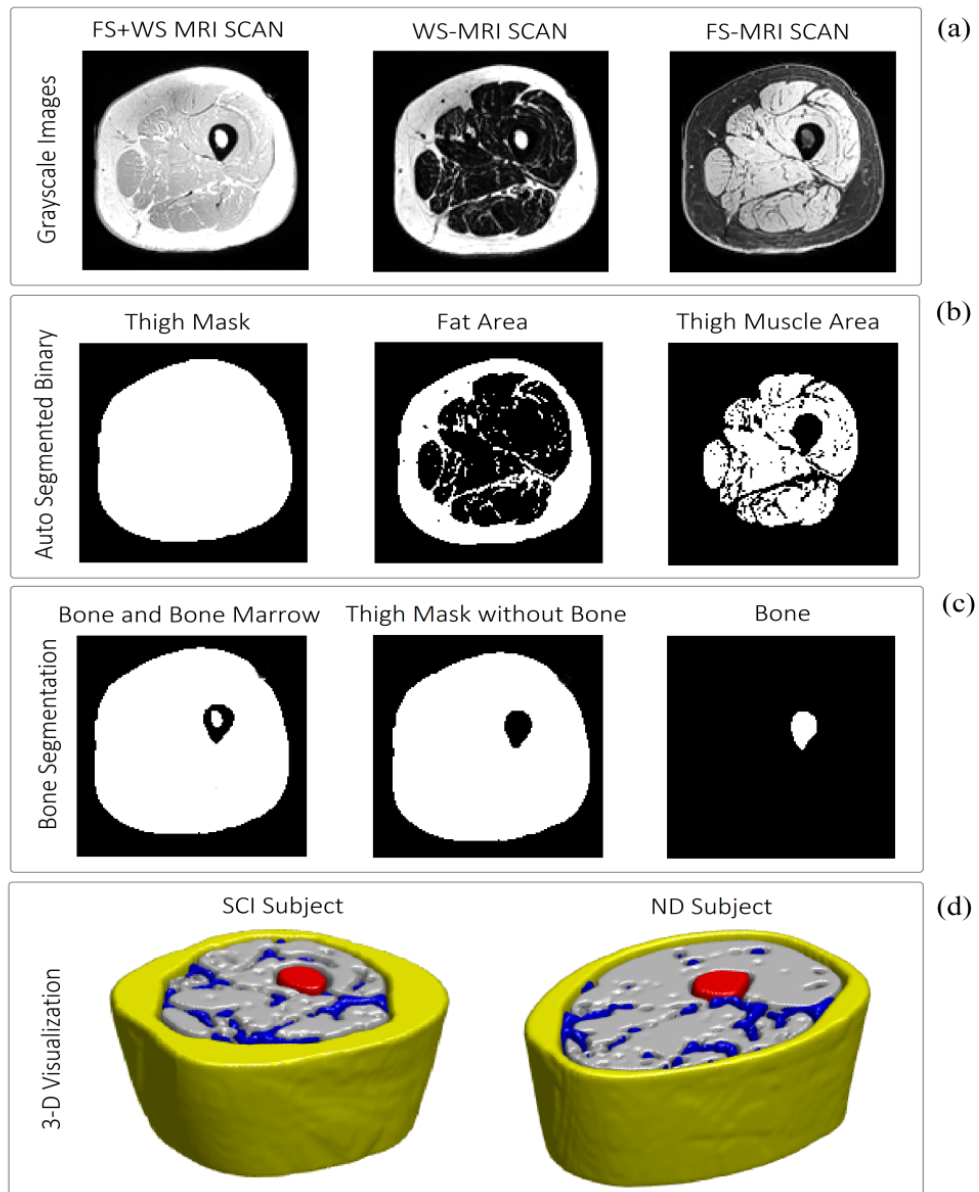


Fig 2.4 Examples for the utilization of LCDG to segment the soft tissue volumes. (a) From left to right: gray scale MR images for FS+WS, WS and FS; (b) From left to right: binary mask of total thigh area, total fat and total muscle area; (c) From left to right: steps for segmenting the bone and bone marrow; (d) 3-D representations of the segmentation results for SCI (left) and ND (right) thigh; Grey: Muscle area, Yellow: SAT, Blue: IMAT, Red: bone.

Table 2.1 The average (\pm SD) accuracy measures (Dice’s coefficient (DC), Recall (R), and Precision (P) of the proposed fat segmentation approach for SCI (N=16) and ND (N=14) individuals.

SCI				ND			
Avg. Metrics	SAT	IMAT	Thigh Muscle	Avg. Metrics	SAT	IMAT	Thigh Muscle
DC	0.91 \pm 0.06	0.85 \pm 0.06	0.97 \pm 0.02	DC	0.97 \pm 0.01	0.86 \pm 0.07	0.98 \pm 0.01
P	0.94 \pm 0.03	0.86 \pm 0.09	0.98 \pm 0.02	P	0.96 \pm 0.02	0.82 \pm 0.11	1.00 \pm 0.00
R	0.89 \pm 0.09	0.86 \pm 0.10	0.96 \pm 0.03	R	0.98 \pm 0.01	0.91 \pm 0.06	0.97 \pm 0.03

b. Muscles Group Segmentation

To obtain the accuracy of the three automatic muscle group segmentations, we used the common technique of leave-one-subject-out, where N-1 subjects are used to build the atlas and one subject was left out for testing, and we repeated this for all subjects in the SCI and ND groups separately. Fig 2.5 reports examples of the cross-sectional area of the original grayscale MRIs (Fig 2.5a), the results of the automatic segmentation of the muscle groups (Fig 2.5b), manually segmented muscle groups overlaid on automatic segmentation (Fig 2.5c), and 3-D representation of automatic segmentation of muscle groups (Fig 2.5d).

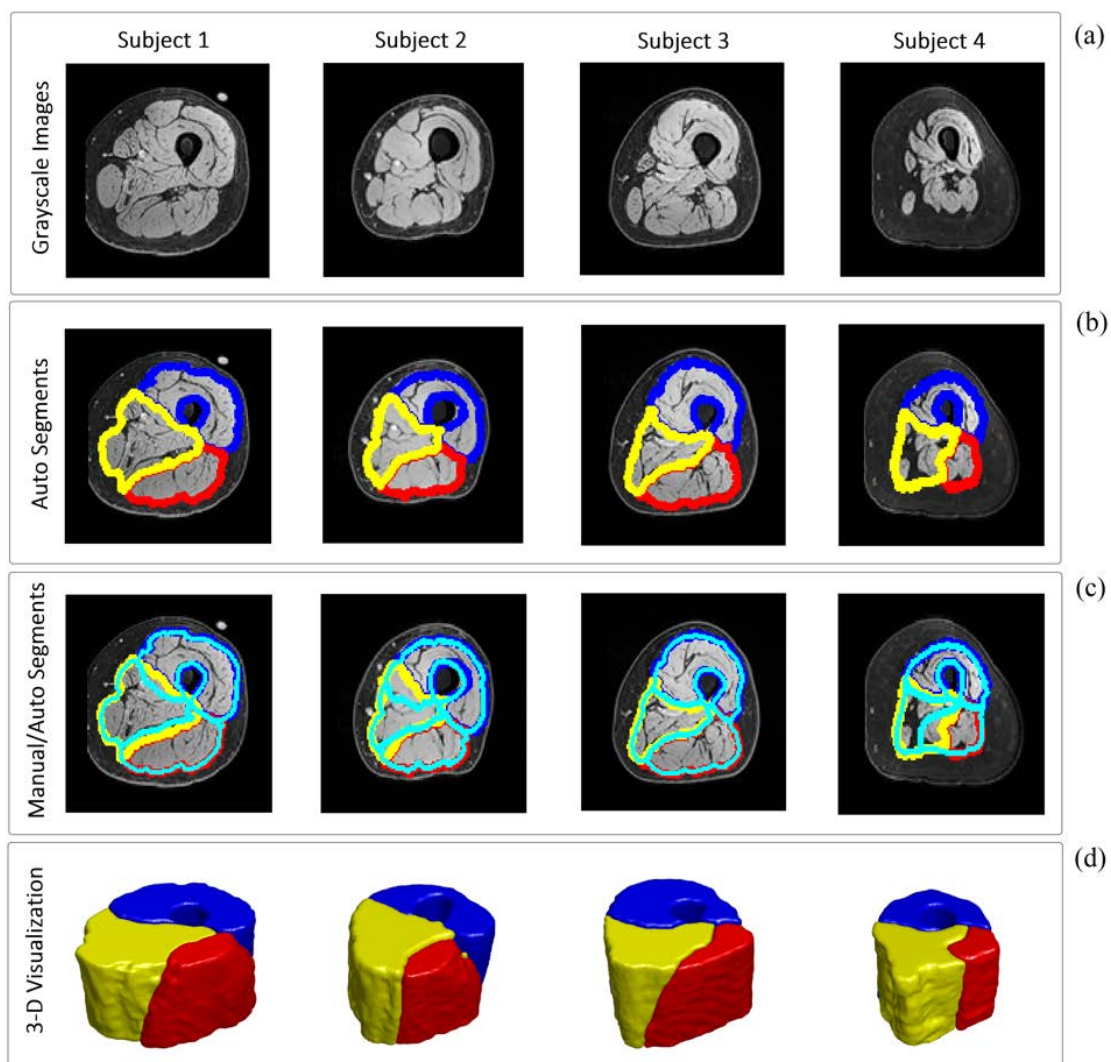


Fig 2.5 Examples of muscle group segmentation algorithm for four SCI subjects. (a) original cross sectional MR image; (b) automatic segmentation of muscle groups: blue area is extensor, red is flexor and yellow presents the medial compartment; (c) manually segmented muscle groups (cyan lines) overlaid on automatic segmentation for comparison; and (d) 3-D representation of automatic segmentation of muscle groups: blue volume is extensor, red is flexor and yellow presents the medial muscle group.

c. Comparison with ANTs and STAPLE

The average accuracy results for different methods (A1: proposed joint MGRF algorithm, A2: ANTs, and A3: STAPLE) are presented in Table 2. The proposed method (A1) reaches 90.79% overall DC, 91.08% of precision, 91.19% of recall, and 16.83 mm of HD compared to DC = 84.39%, P = 90.72%, R = 81.96%, and HD = 19.64 mm for A2, and DC = 86.03%, P = 91.12%, R = 86.16%, and HD = 18.29 mm for A3. In summary, these data show that our approach leads to more accurate results compared to the other two methods that were tested in this study.

Table 2.2 The average (\pm SD) accuracy measures (Dice’s coefficient (DC), Recall (R), Precision (P), and the Hausdorff distance (HD) for three methods (A1: proposed algorithm, A2: ANTs, and A3: STAPLE) for SCI and ND groups.

Method	SCI Group			ND Group				
	Metric	Group 1 extensor	Group 2 flexor	Group 3 medial	Metric	Group 1 extensor	Group 2 flexor	Group 3 medial
A1	DC	0.94 \pm 0.03*	0.88 \pm 0.06*	0.89 \pm 0.05*	DC	0.95 \pm 0.03	0.90 \pm 0.03 [‡]	0.89 \pm 0.06*
	P	0.95 \pm 0.03	0.91 \pm 0.08*	0.87 \pm 0.10	P	0.92 \pm 0.06	0.91 \pm 0.04 [‡]	0.89 \pm 0.07
	R	0.94 \pm 0.05*	0.86 \pm 0.08*	0.91 \pm 0.04*	R	0.97 \pm 0.03	0.90 \pm 0.07 [‡]	0.90 \pm 0.11*
	HD(mm)	12.98 \pm 6.44*	12.84 \pm 6.96*	20.47 \pm 10.24	HD(mm)	10.51 \pm 6.1	12.67 \pm 3.13	31.53 \pm 14.24
A2	DC	0.84 \pm 0.12	0.79 \pm 0.10	0.84 \pm 0.10	DC	0.89 \pm 0.08	0.85 \pm 0.09	0.85 \pm 0.09
	P	0.95 \pm 0.03	0.89 \pm 0.09	0.89 \pm 0.07	P	0.92 \pm 0.05	0.89 \pm 0.08	0.90 \pm 0.09
	R	0.80 \pm 0.20	0.77 \pm 0.16	0.79 \pm 0.17	R	0.88 \pm 0.14	0.84 \pm 0.13	0.83 \pm 0.15
	HD(mm)	20.22 \pm 6.07	14.75 \pm 5.90	19.80 \pm 9.29	HD(mm)	16.70 \pm 6.4	14.94 \pm 5.91	31.45 \pm 9.93
A3	DC	0.86 \pm 0.10	0.83 \pm 0.10	0.85 \pm 0.07	DC	0.89 \pm 0.08	0.87 \pm 0.07	0.86 \pm 0.07
	P	0.96 \pm 0.03	0.90 \pm 0.09	0.89 \pm 0.08	P	0.92 \pm 0.05	0.90 \pm 0.07	0.91 \pm 0.07
	R	0.82 \pm 0.18	0.82 \pm 0.14	0.86 \pm 0.12	R	0.91 \pm 0.12	0.90 \pm 0.06	0.87 \pm 0.14
	HD(mm)	15.60 \pm 6.71	13.42 \pm 7.27	22.41 \pm 9.48	HD(mm)	12.85 \pm 6.7	14.12 \pm 4.58	32.35 \pm 12.31

* Our proposed algorithm showed equal or higher accuracy than the other two methods.

d. Comparison with CNN

In order to examine advantages and limitations of the deep learning approach for thigh MRI segmentation task, we have implemented the DeepMedic CNN network structure to perform the segmentation task on our entire dataset. Based on the DC similarity measure for segmentation of the three muscle groups without the IMAT, and segmentation of bone and SAT volumes, the performance of the trained CNN network was 0.93 ± 0.03 when all 30 subjects included in the present study were considered; this value was slightly higher than that obtained using the framework proposed in this study (0.92 ± 0.05). On the other hand, the precision measure of our framework (0.94 ± 0.06) was slightly higher than the CNN (0.93 ± 0.05) and the total HD calculated for our framework is only 11.82 ± 6.72 mm which is considerably higher than the HD value calculated for the CNN network, 20.48 ± 16.43 mm, suggesting that CNN network tended to be less accurate than the framework proposed in the present based on this accuracy measure.

e. Comparison Between SCI and ND volumes

The volumes of SAT, IMAT, thigh muscle, extensor muscles, flexor muscles, and medial compartment muscles were calculated based on both manual and automatic segmentation for all subjects, and presented for the SCI and ND groups separately (Fig 6). In order to determine any statistically significant difference between SCI and ND groups for each of these parameters, we used the non-parametric two-tailed Wilcoxon rank sum test with alpha level set at 0.05. This test can be used for two populations with unequal sample sizes and independent samples. The SAT and IMAT volumes were significantly greater in ND compared to SCI when the results from automatic segmentation were considered

(Fig 6a and b), and the same trend ($p = 0.058$) was observed also for manual segmentation. Similarly, all muscle-related volumes were significantly greater in the ND group ($p < 0.0001$) when both manual and automatic segmentation were considered (Fig 6 c to f).

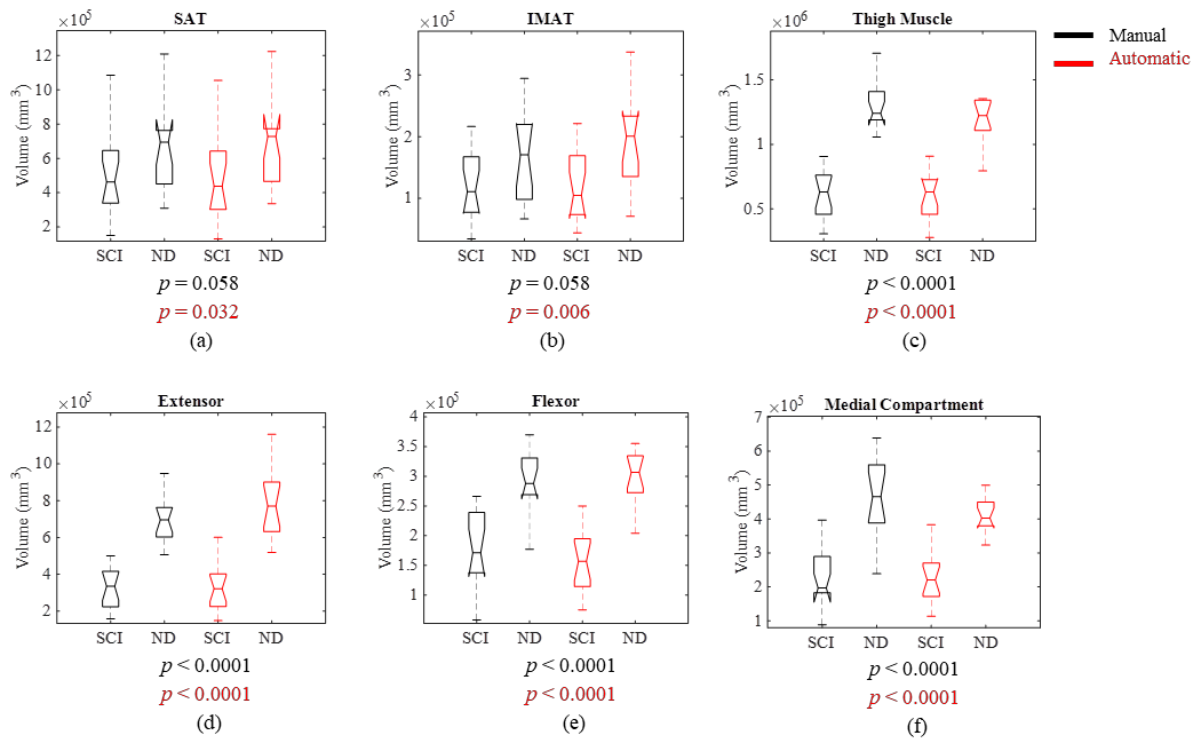


Fig 2.6 The boxplot representation of the calculated volumes and ratios for manual (black) and automatic (red) segmentation results. (a) Extensor volume; (b) Flexor volume; (c) Medial volume; (d) IMAT volume; (e) SAT volume; (f) Total muscle volume; and (g) IMAT /muscle.

D. Discussion

The primary focus of this study was to design, implement and examine a fully automatic framework for MRI thigh muscle and adipose tissue segmentation and volume quantification in individuals with severe SCI. The proposed segmentation framework (Fig 1) consists of three main steps: total muscle and adipose tissue segmentation based on the intensity contrast between different tissues; three muscle compartments segmentation based on three-fold stochastic integrated model (shape prior, spatial interactions and intensity); and volume quantification of the segmented parts.

In the early attempts for automatic segmentation of fat and muscle areas in MRI scans, most methods were initially designed to separate muscle and adipose tissues based on their pixel signal intensity differences. Particularly in the segmentation of MRI scans of human thighs, Barra et al. [73, 74] proposed fuzzy clustering algorithm using gray-level as voxel feature with post-processing adjustments to segment muscle and fat volumes. Histogram thresholding methods were also utilized broadly in the literature for this task [98]. Imamoglu et al. [99] also used MRI thigh scans with saliency features to extract thigh muscle volumes using morphological operations and binary fuzzy decision-based fusion. In spite of their popularity, intensity-based methods have a major setback as, for example, they cannot distinguish between different types of fat (SAT/IMAT). Therefore, the automatic segmentation methods have evolved to more advanced techniques to make these separations possible. For instance, Positano et al. [75] in 2009 added the active contour algorithm to the fuzzy clustering method to segment SAT and bone area and expectation maximization (EM) algorithm to separate IMAT from muscle area when investigating obese individuals. Similarly, Kovacs et al. [100] used the contouring

method to segment fascia lata to separate SAT and IMAT in severe muscular dystrophy cases. In a recent study, Irmakci et al. [101] proposed an extended version of fuzzy connectivity method to segment the fat and whole muscle areas of thighs as well as brain and whole body tissue using multi-modal MRI images. However, segmenting the challenging task of segmenting different muscles or muscle groups in the absence of substantial intensity differences between muscles is not addressed in this study. In the present study, we also used LCDG intensity-based method for assessing thigh muscle and adipose tissue using FS and WS MRI scans of thigh. The multi-modal MRI scans of thigh muscles have been rarely used in previous automatic thigh segmentation studies. This alternative modality of MRI is particularly advantageous for thigh segmentation since it uses opposite contrasts for fat and muscle tissues in FS and WS images, and therefore by utilizing intensity-based method (LCDG) only, we could segment the whole adipose tissue in WS slices and the whole muscle area in FS images and use it as a mask to separate SAT and IMAT. Utilizing the sum of WS and FS was also used to segment the bone and bone marrow areas (Fig 4). This approach allowed us to avoid the use of a priori shape information or iterative contouring algorithm for this part of the segmentation.

The segmentation of different muscles and/or muscle groups is also a task that intensity-based segmentation methods cannot accomplish. This type of segmentation started with Andrews et al. [76], who proposed a framework for using principal component analysis (PCA)-based shape prior from the training dataset to segment the knee flexor and extensor individual muscles in MR 3-D volumes. Similarly, Baudin et al. [77, 78] introduced the iterative random walk (RW) segmentation framework for segmenting

individual muscles by starting from a priori shape information and utilizing the support vector machine (SVM) method to estimate the RW parameters. A hybrid method was proposed by Andrews and Hamarneh [76] by combining the generalized log-ratio probabilistic shape model and random forest binary detector to segment each individual muscle of the human thigh. Utilizing the atlas-based methods has been gained more attention in recent years with Ahmad et al. [79] framework of atlas construction and image registration to segment the quadriceps muscle group. Another atlas-based segmentation method was proposed by Troter et al. [80] to segment four individual muscle volumes inside the quadriceps group by using semi-automated single-atlas and fully automated multiple-atlas approaches and suggesting that the single-atlas method was more robust for individual muscle segmentation and has a better accuracy. In 2017, Orgier et al. [102] have proposed a new semi-automatic technique for segmenting the same four quadriceps muscles by manually segmenting the top and bottom slices and using the propagating non-linear registration approach to segment the middle slices. In the thigh volumes segmentation application, we were particularly interested in segmenting knee extensors and knee flexors muscle groups because of their important functional role in human movement generation. Unlike previous studies that only used prior shape information for muscle segmentation, our proposed method uses all three components of shape, spatial (MGRF) and intensity (LCDG) to determine if a given voxel belongs to any of the three muscle groups considered (knee extensors, knee flexors, or medial compartment) (Fig 5). The segmentation method proposed in this study was applied on a group of individuals with severe SCI and on a group of ND individuals. In order to build a generic thigh segmentation atlas for ND group, we recruited individuals

considered as normal ($N = 3$), overweight ($N = 5$) and obese ($N = 6$) as for their BMI [103]. The DC accuracy values (Table 1) suggest that the fat and thigh muscle area, which were segmented using the LCDG intensity-based approach showed overall high accuracy values, which were equal to $90.97 \pm 6.74\%$ for the SCI group and $93.91 \pm 7.02\%$ for the ND group. For the muscle compartment segmentation, the proposed method showed on average $90.41 \pm 5.59\%$ accuracy for SCI group and $91.18 \pm 5.02\%$ for ND (breakdown numbers are presented in Table 2). The very similar accuracy for the muscle compartment segmentation between SCI and ND is noteworthy, seen as the SCI group showed substantial inter-individual differences, as exemplified in Fig 5 (see subject 4 compared to the other three subjects).

In order to further evaluate our segmentation method, we also compared the accuracy results related to muscle compartment segmentation with those obtained from two other well-known segmentation methods (ANTs and STAPLE). The three-fold integrated model proposed in this study showed an overall greater accuracy compared to ANTs and STAPLE, as for the accuracy measures that were calculated (DC, R, P and HD; Table 2). This may be due to the positive effect of integrating both the appearance and spatial models with the prior shape information from the atlas into a three joint MGRF model. In particular, the prior atlas enables the proposed approach to use known muscle anatomy to distinguish and correctly classify different muscle compartments that have the same appearance, while the spatial models handle any inhomogeneity that may exist within a muscle compartment.

We also performed the entire thigh muscle and fat segmentation task with the well-known DeepMedic 3-D CNN structure to compare its performance with the stochastic-

based algorithm proposed in this study. The different trends observed for DC and HD indexes may be due to the fact that the falsely segmented voxels of the CNN method were mostly happened far from the boundary of the targeted areas which have longer distances from the actual borders (greater HD) whereas for the joint MGRF method, the falsely segmented voxels mostly happened near the borders of the muscle groups which lead to smaller HD values. While the CNN performance was comparable to the proposed method for muscle MRI segmentation task, implementing the CNN code required extensive memory and computations as well as expertise in programming in Linux OS, Python and TensorFlow. The total executive run-time for segmenting the entire database using 3-D CNN was 52.0 hours on GPU while the total run-time for the proposed method was only 5.3 hours on CPU (S7 Table). We also attempted to run the DeepMedic software multiple times over 4 weeks for the training step using a regular CPU, but we were unable to properly train the network. The CNN training duration is still dramatically longer than the processing time of the proposed framework. However, once the CNN algorithm is trained, the processing time for segmenting the testing subjects was relatively low. We have shown that the 3-D CNN-based method can be quickly adjusted to thigh MRI segmentation task without any changes to the network structure. Also the CNN can be trained on part of the dataset and segment the other part (test scans) with acceptable accuracy and relatively fast using GPU; however, as the number of test subjects grows over time in a clinical setting, it would be desirable to re-train the network or use transfer learning [104] to improve the segmentation accuracy. Conversely, in the proposed framework, all the previously segmented and reviewed scans can be utilized in

the future atlases to guide the segmentation of a new thigh MRI scan without substantial additional computational cost.

Finally, we compared the volumes of SAT, IMAT, thigh muscle, knee extensors, knee flexors, and medial compartment between SCI and ND groups using the results obtained from both automatic and manual segmentation (Fig 6). The main goal of this comparison was to examine whether the same conclusion in terms of physiological differences between the two groups could be achieved using both segmentation methods. SAT and IMAT volumes were significantly greater ($p = 0.023$ and $p = 0.009$, respectively) in ND using automatic segmentation outcomes; a similar trend ($p = 0.058$) was also observed using the volumes calculated from manual segmentation (Fig 6 a and b). The greater adipose tissue volumes found in ND is an unexpected finding, as most of the data reported in the literature show that after SCI there is an increase in body fat mass as well as IMAT in the thigh [65, 105]. The ratio between IMAT and thigh muscle volume calculated in the SCI group of the present study (19.8%) is within the range observed in other SCI individuals [65, 105]. On the other hand, most of the ND individuals enrolled in the present study were either overweight or obese, and these conditions can result in increased SAT and IMAT volumes [106].

Thigh muscle volume and the volumes of the three investigated muscle compartments were significantly greater in ND individuals compared to the SCI group when outcomes from both automatic and manual segmentation were considered (Fig 6c to f). These findings are in agreement with previous studies that showed marked SCI-induced muscle atrophy [64, 65].

In conclusion, we developed a novel and accurate MRI-based segmentation framework that can automatically segment thigh subcutaneous and intermuscular adipose tissue as well as muscle tissue related to knee extensors and knee flexors in individuals with SCI. These parameters have important health and functional implications in the SCI population and the proposed segmentation method can facilitate the use of MRI to assess individual characteristics and possibly the effects of different interventions. This framework could be further improved by increasing the MRI resolution, which would allow an accurate segmentation of intra-muscular adipose tissue and individual muscles, and by increasing the number of thigh MRI slices from the 50 central to the whole thigh in order to make a more comprehensive assessment of the different volumes.

E. Application: SCI Case study

In this study, we have utilized the proposed segmentation framework to quantify the effects of an activity-based training on the volumes of fat and muscle compartments in an individual with a motor incomplete SCI. We want to evaluate the accuracy of the automatic framework and its ability to find meaningful trends in different training time intervals.

Characteristics of research participant and training protocol

Subject: Gender: female; Time since injury: 4 yrs; Age: 22 yrs; Weight: 102 lb; AIS D; neurological level of injury: T12, that affected the motor function of the right lower limb only.

Interventions: Activity-based rehabilitation was performed for about 9 months and predominantly consisted of neuromuscular electrical stimulation of the affected leg

during standing and slow walking as well as walking over-ground without stimulation. During the 3.5-month follow up she performed stand training with stimulation.

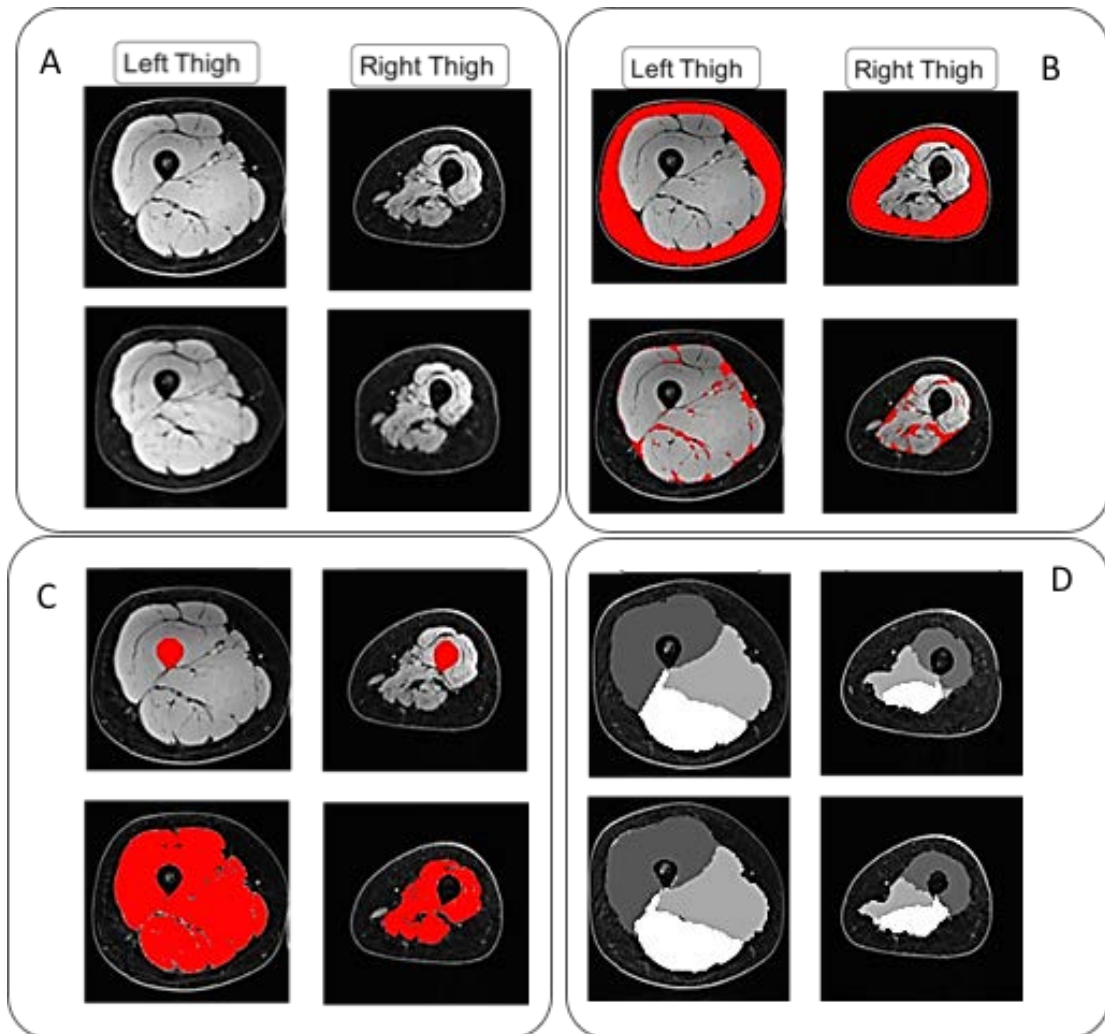


Fig 2.7 Steps for muscle and adipose tissue segmentation of MR thigh images: (a) Top: original left and right MR thigh images, bottom: corresponding registered images; (b) Top: segmented subcutaneous fat, bottom: segmented intermuscular fat; (c) Top: bone segmentation, bottom: segmented muscle area; (d) Top: manual muscle group segmentation, bottom: automatic muscle group segmentation of left and right thigh images.

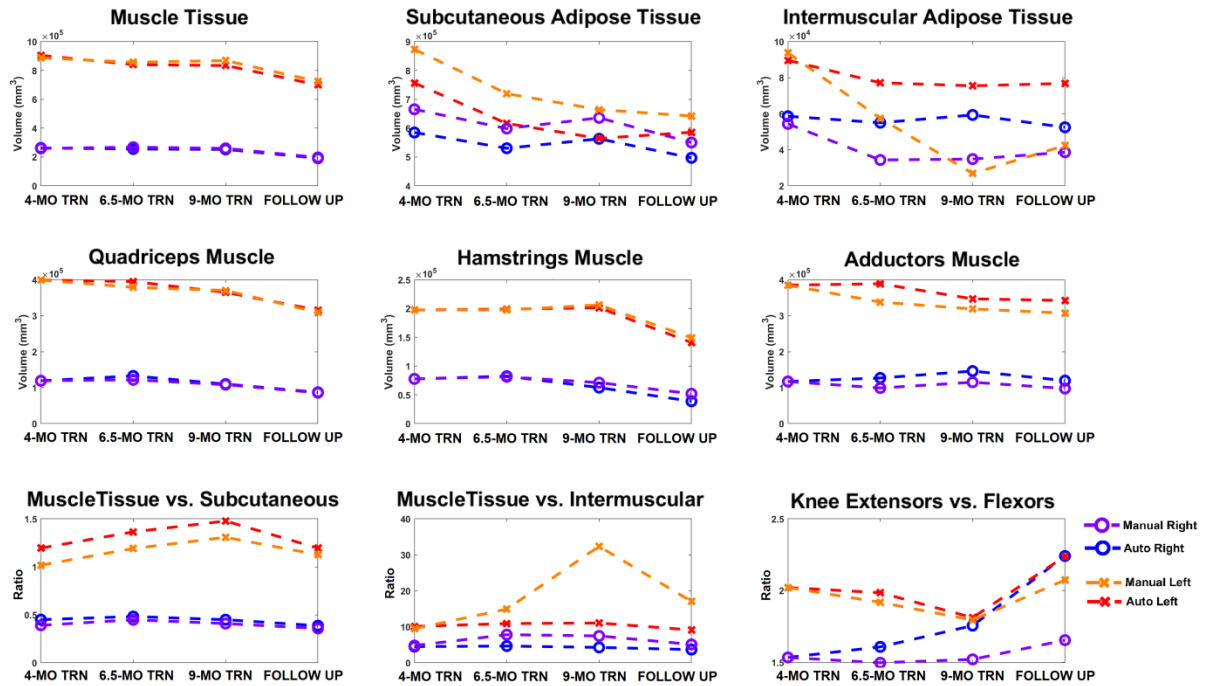


Fig 2.8 Comparison of the segmented volumes and volume ratios of manual (purple and orange lines) and automatic (blue and red lines) outputs for right and left thighs, respectively, at four different time points during the activity-based interventions.

We compared the output of both automatic and manual segmentation of thigh MRI volumes for both left and right thighs at four different time points during the activity-based interventions. As it is shown in Fig 2.7, the right leg, which was affected by SCI, showed severe muscle atrophy and fat infiltration compared to the unaffected leg (left). Moreover, Fig 2.8 shows the automatic segmentation of muscle groups follows closely the manual results. In this figure, we calculated the volumes of Muscle Tissue, Subcutaneous Fat, Intermuscular Fat, Quadriceps, Hamstrings and Adductors muscles based on the manual and automatic segmentations respectively. The ratios of Muscle Tissue to Subcutaneous Fat, Muscle Tissue to Intermuscular Fat and Knee Extensors to Flexors were also calculated for these two methods. Using statistical analysis, we

calculated the significance of differences between manual and automatic values. The results suggest that there are no significant differences for muscle tissue volume, three muscle compartments and muscle tissue to subcutaneous fat and knee extensors to flexors ratios. However, there are significant differences between manual and automatic methods for intermuscular fat volumes ($p = 0.01$) and muscle tissue to intermuscular fat ratio ($p = 0.007$). Furthermore, it can be interestingly observed from these graphs (Fig 4) that training promoted an important decrement of inter-muscular and subcutaneous fat in both left and right thighs and these trends are visible from both automatic and manual segmentation results.

F. Study Outcomes

The preliminary outcomes of this study have been published as two full-papers in prestigious conferences MICCAI and ICIP (2017). The final results for applying the proposed framework on 30 MRI thigh volumes with comparison to other well-known segmentation methods is currently under review for publication at PLOS ONE journal. The results of the proposed segmentation framework and its application in the longitudinal case study have been presented as posters in KSCHIRT Symposium 2017, BMES Conference 2017 and University of Louisville Speed School Exposition 2018. The developed automatic MRI segmentation method has also been filed as a patent disclosure by the University of Louisville Technology Transfer office.

CHAPTER III

ACTIVATION DETECTION AND COLORMAP REPRESENTATION OF EPIDURAL STIMULATION MAPPING OF SPINAL CORD

A. Introduction

Previously, it has been shown that epidural electrical stimulation in combination with locomotor training and/or pharmacological interventions in animal models were able to highly promote spinal circuits functionality after complete spinal cord transections in rats [107, 108]. Subsequently, in the past several years, clinical studies have also reported that lumbosacral spinal cord epidural stimulation (scES) combined with activity-based training progressively re-enabled full weight bearing standing [6] [7] and volitional control of lower limbs in individuals with chronic complete paralysis [13, 14]. Remarkably, the appropriate selection of stimulation parameters (amplitude, pulse width, frequency and anode/cathode assignment) was shown to be critical to promote the generation of effective motor patterns [6]. Mapping experiments were initially performed with participants in supine position, recording motor evoked potentials from different lower limb muscles using surface electromyography (EMG) during scES with different sets of electrode configurations. The purpose of these experiments was to study the topographical features of recruiting leg muscles by scES [109] and also to provide useful information for the selection of electrode configurations applied for promoting lower

limb motor function. The task of determining the links between scES parameters and the characteristics of the evoked potentials is referred to as the “mapping” task in this study. To study the characteristics of the scES induced evoked potentials, the first step is to localize them inside raw EMG signals that are recorded from several leg muscles by segmenting each EMG signal based on the stimulation onset. One of the most challenging tasks in EMG analysis in the scES content is the precise detection of each epidurally evoked potential. This task is crucial in order to determine the effective threshold for scES intensity that triggered the occurrence of the first visible evoked potential for each muscle. The evoked potential (activation) detection is usually performed manually by a trained observer visually inspecting the raw EMG signals, which is considered to be the most accurate method for activation detection. However, it is a laborious task when facing a large stack of data recorded from several muscles during various experiments. Moreover, manual method can be prone to human errors and inter/intra-observer variation and would also limit the ability to allow scalability to a high number of patients. Therefore, to facilitate the activation detection process, an accurate computer-based method is proposed in this work.

Signal Change Detection Methods

There have been several methods proposed for computer-based change detection for EMG signals in the literature, such as the single or double threshold detector[38], Teager–Kaiser Energy Operation[39-41], wavelet template matching[42], supervised and unsupervised learning algorithms [43] or statistical criterion determination methods like hidden Markov models [44] and Gaussian mixture models[45, 46]. The main goal of all these methods is to convert the original raw signals into a set of estimated sequences that

make the highest distinction between before and after change as well as detect the occurrence of the change and the corresponding time instant, t_0 , as early as possible[45].

Most of the automatic onset detection methods can be divided into four main stages: pre-processing, conditioning, decision thresholding, and post processing. Most methods have a pre-processing stage for filtering the raw signal with a band-pass filter in order to remove artifacts and reduce the noise level in the signal. In the conditioning stage, the EMG signal passes through a test function, i.e. a type of event indicator. In the third stage, the algorithm will set a threshold that indicates the first point of the signal change. Finally, the last stage deals with the false alarms by setting certain constraints on the detected onset values [45, 110]. Most of the methods differ based on the type of test function; the decision rule, which involves the selection of constant or dynamic thresholds; and the heuristic constraints for the final detected onset, which varies based on the application and the characteristics of the EMG signals. There are several categories of event indicator functions, such as on-line vs. off-line, or supervised versus unsupervised learning algorithms. If an algorithm has been executing the task in a sequential fashion for each incoming data point, the method is called on-line; otherwise it is considered off-line[45]. Also, if the training input data for a learning method is already labeled using a priori information, the method is supervised, and if the algorithm estimates a model for the input data using specific parameter estimation techniques, it is an unsupervised technique.

In every activation detection method, sensitivity to the noise level in the signal is a great challenge. Selection of proper pre- and post-processing methods usually helps to minimize the effect of noise on the accuracy of the method. It is also notable that some of

the proposed methods are highly dependent on prior information of the signal, i.e. supervised methods, which makes those methods semi-automatic and their accuracy application-dependent. In this study, we suggest a novel method to address these two main challenges that a fully automatic activation detection method faces, by proposing an unsupervised and on-line approach that deals with the stochastic characteristics of the EMG signals in the scES application.

The main purpose of this work is to develop a novel method for automatic detection of the epidurally evoked potentials using a generalized framework to perform the scES-EMG mapping task. The generalized framework will: 1) effectively de-noise, detect, and extract the key features of the signal; 2) visualize the occurrence of the muscle evoked potentials induced by scES; and, 3) increase the accuracy and efficiency of the physiological mapping process in order to determine the underlying relationships between the scES parameters and muscle activations. Consequently, this framework will assist the data analysts to promptly decide on further adjustments or improvements in designing future experiments.

B. Materials and Methods

a. Participants, Stimulation and Data Acquisition

Participants

In this study, five male individuals with motor complete spinal cord injury (SCI) have participated. Two of these participants have American Spinal Injury Association Impairment Scale (AIS) grade B and three of them have AIS grade A. The average age of these five individuals at the time of the experiments was 29.8 ± 4.5 years old and the average time since injury was 4.2 ± 1.6 years. All five participants have provided

written, informed consent for the experimental procedures, which have been approved by the University of Louisville Institutional Review Board.

Spinal Cord Epidural Stimulation: A stimulation unit (RestoreAdvanced Neurostimulator, Medtronic, Inc., Minneapolis, MN) in combination with a chronic, 16-electrode array (39565 paddle electrode array, Medtronic, Inc., Minneapolis, MN) is surgically implanted at the T11–L1 vertebral levels over the spinal-cord segments L1–S2. It is used to deliver electrical stimulation to the lumbosacral spinal cord of each SCI individual. The electrode array was connected to the IPG unit that was implanted in a subcutaneous abdominal pouch[13].

EMG recording system: National Instrument Data Acquisition system (National Instruments, Austin, TX) was built to collect both EMG signal and the signal from the communication signal detector. EMG signals were recorded and filtered (band-pass filter of 10 Hz–2 kHz (–3 dB)) with differential surface electrodes (Motion Lab Systems, Baton Rouge, LA) from Motion Lab MA300 EMG system. Two surface electrodes were placed symmetrically lateral to the electrode array incision site over the paraspinal (PS) muscles in order to record the stimulation artifacts. Other electrodes are placed to record 14 thigh and leg muscles signal. A communication signal detector was developed to capture the communications signal (stimulation parameters) between the Clinician Programmer and IPG. The communication signal detector sends detected stimulation parameter change to the data acquisition system. Using the PS EMG artifact signal and the captured communication signal to mark the onset of each stimulation pulse[109]. Fig 3.1 illustrates the connections between the epidural stimulation unit and the EMG recording system.

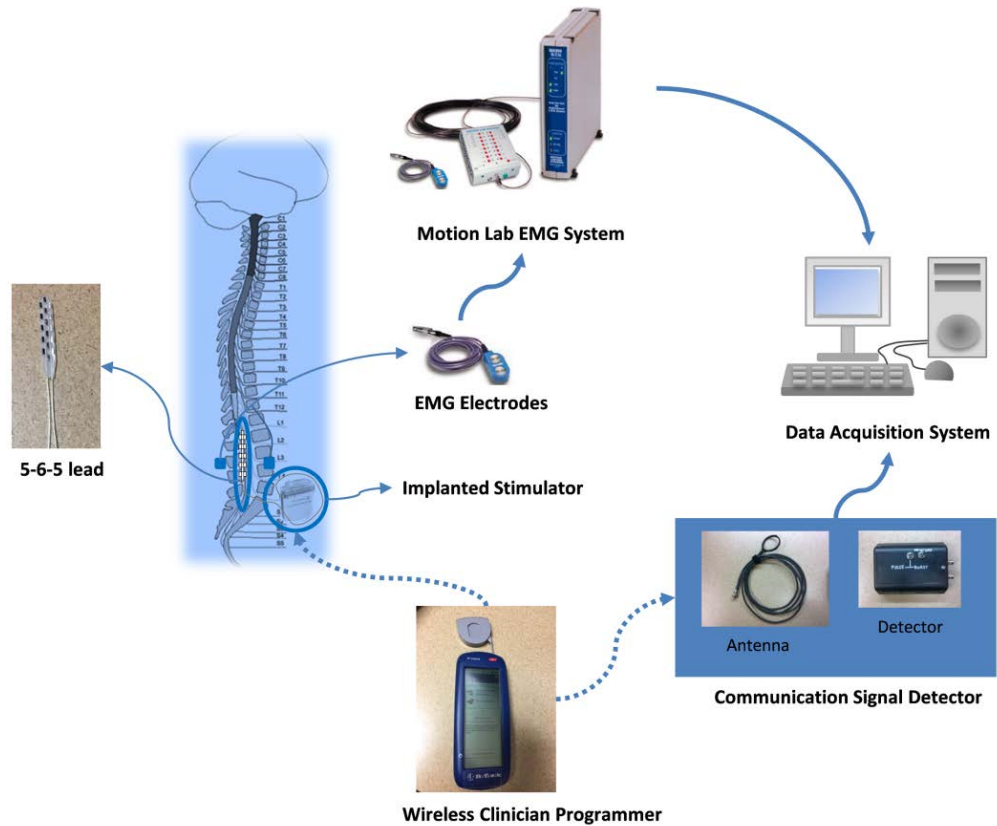


Fig 3.1 scES and EMG connections. Schematic representation of the epidural stimulation unit (16-electrode array, IPG unit and wireless programmer) and its connections to the EMG recording system¹.

EMG data acquisition

The scES lower limbs mapping experiments start 2–3 weeks after the surgical implantation [13, 109]. The supine experiments are performed in accordance with the procedures previously described by [13] with the participants relaxed in a supine position. The electrical stimulation waveforms are comprised of a rectangular, biphasic shape with pulse duration of 450 μ s. In the supine experiments, specific combinations of

¹ Permission to use the illustrations of the Motion Lab EMG System and EMG electrodes was granted from Motion Lab System Inc.

electrodes are selected for activation, which is referred to as stimulation configuration. A total of 12 different stimulation configurations are examined for each individual. For each configuration, stimulation intensity or frequency will be increased whilst the other parameters are fixed. The stimulation voltage (intensity) ramp-up experiments are performed with the scES intensity (in volts) gradually increased and the frequency is set at 2 Hz. During each intensity ramp-up, the scES intensity starts at a pre-activation value (V) and increases at either 0.1 or 0.5 V increments up to 10 V with time interval between each ramp-up at least 2-3 seconds, which in this time interval scES delivers a minimum of five stimulus pulses for each intensity level (at 2 Hz). In the frequency ramp-up experiments on the other hands, after the intensity is set at the value where all the muscles are activated ($f = 2\text{Hz}$), the frequency is increased from 2 to 5 Hz and from 5 to 60 Hz with the step 5 Hz.

During the performance of each experiment, the surface EMG signals are recorded from 14 leg muscles, using bipolar surface electrodes that are placed on the left (L) and right (R) soleus (SOL), medial gastrocnemius (MG), tibialis anterior (TA), vastus lateralis (VL), rectus femoris (RF), medial hamstrings (MH), and gluteus maximus (GL). The recorded EMG signals are digitized at a sampling rate of 2000 samples per second. The heart rate and blood pressure data of each participant are also recorded during the experiments.

b. Methodology

In this study, a set of five algorithms is proposed to perform the mapping task in an automated fashion to convert the raw recorded EMG signal into its significant building blocks, i.e. the evoked potentials induced by scES. Additionally, the algorithms extract

several key features of these evoked potentials, such as peak-to-peak amplitude, latency, integrated EMG and Min-max time intervals, and enable visualization of these features to effectively represent the desired hidden information in the EMG recordings to the data analysts. Fig 3.2 illustrates the block diagram of the general framework.

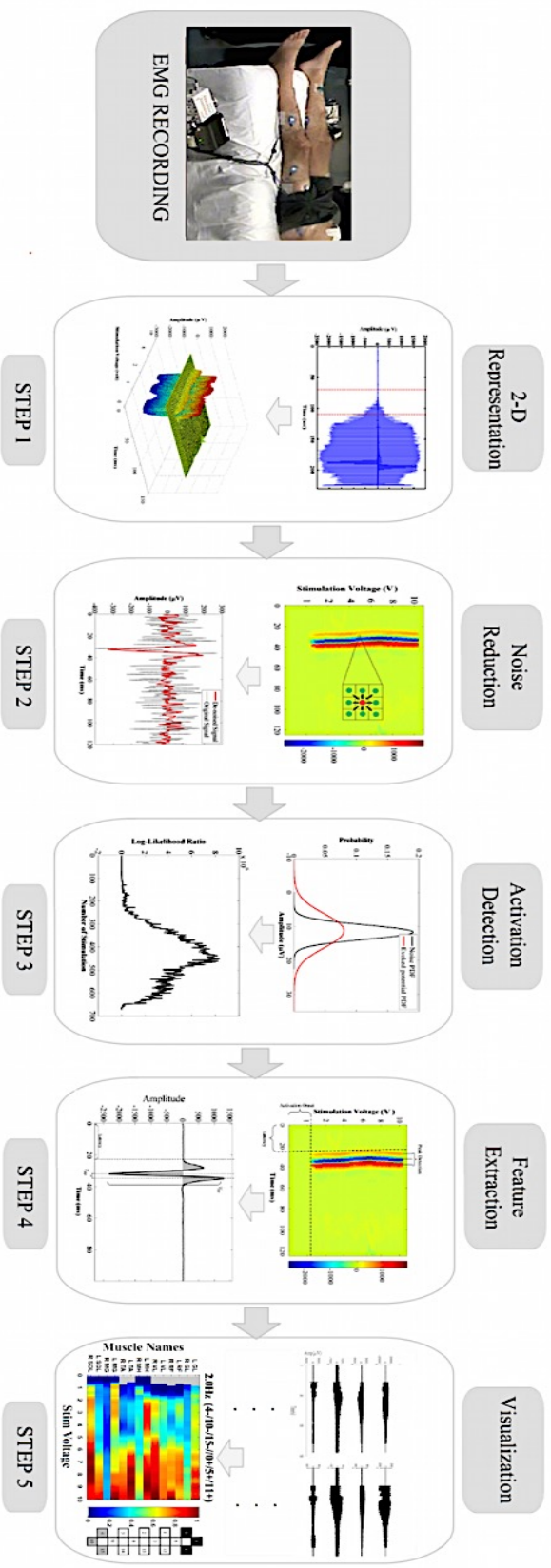


Fig. 3.2 Block diagram of the proposed framework for visualization and activation detection of evoked potentials induced by scES.

2-D representation of EMG Signal

From a computational point of view, each single record of the EMG ($x_k, k \geq 1$) is a set of sample observations from a discrete random process ($X_k, k \geq 1$). The EMG signals, which are recorded from all 14 leg muscles, consist of evoked potentials ($w_1, w_2, \dots, w_N \in W$) that are induced by ES. Utilizing the onsets of the stimulation pulses, the whole EMG signal is segmented into its building blocks (W set) where each segment consists of the time interval between two consecutive stimulation pulsations (Fig 3.3A, 3B). Subsequently, the first algorithm converts the EMG signal, X_k , to a 3-D image, $\delta_k(x, y, z)$, by overlaying all the EMG signal segments and then displaying their value in 3-D graphs (Fig 3.3C). These 3-D graphs are converted to 2-D images using Colormap algorithm where the amplitude values are represented as colors (Fig 3.3D). Each row in the Colormap image illustrates one segment of the whole EMG signal. Fig 3.2 demonstrates all the steps for this conversion process for a sample EMG signal.

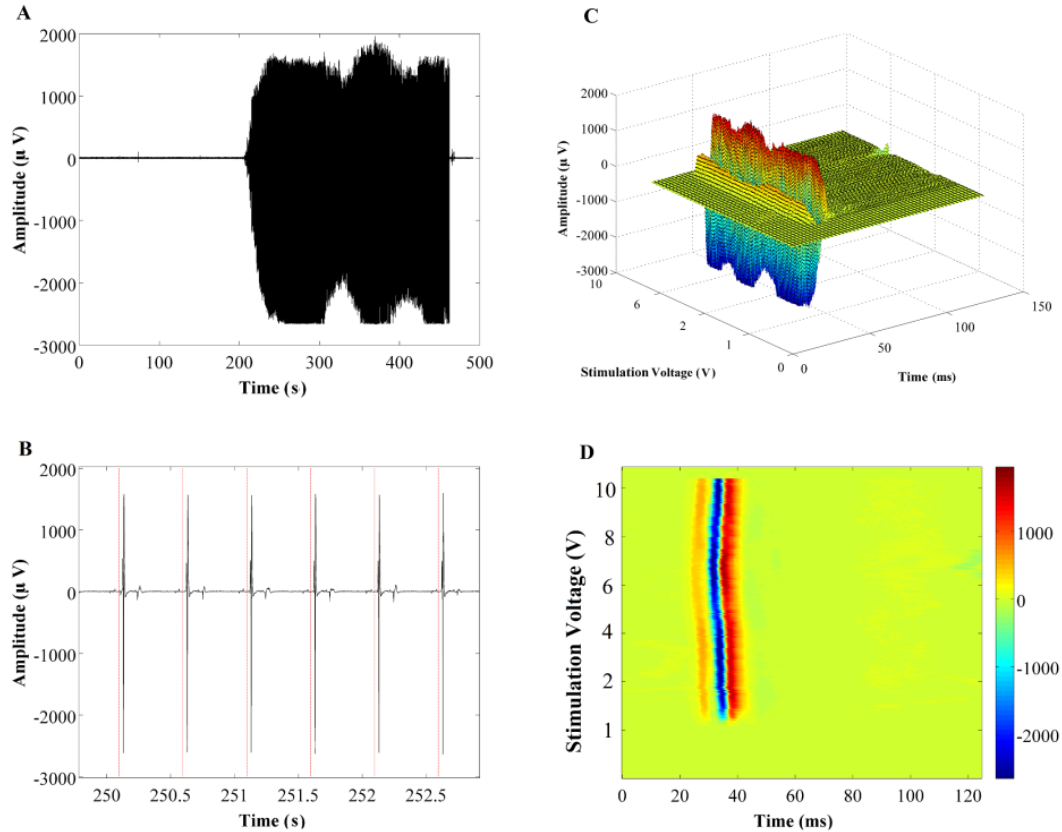


Fig 3.3 The steps for converting raw EMG signals into 2-D and 3-D images. (A) Raw EMG signal, (B) Signal segmentation using stimulation time intervals, (C) Overlaying all the segments and building the 3-D graph where X-axis is the evoked potentials duration (ms), the Y-axis is the stimulation voltage (V), and the Z-axis is the amplitude of the signals (μV) and (D) Converting the 3-D graphs into 2-D images using Colormap.

Noise Reduction

After signal to image conversion, it is possible to use image-processing techniques for smoothing the images and consequently de-noising the signals. In this study, a 2-D generalized Gaussian Markov Random Field (GGMRF) model is applied to the constructed 2-D images so as to reduce the noise level from the EMG signal[111]. This particular smoothing method preserves continuity and removes inhomogeneity in the image, which in this context is caused by background noise in the original EMG signals.

This is achieved by comparing each pixel's value, which is the evoked potential amplitude in μV , to the n-neighborhood pixel set and recalculating the respective pixel value based on Eq. 3.1.

$$\hat{\delta}_s = \underset{\delta_s}{\text{argmin}} \left\{ |\delta_s - \tilde{\delta}_s|^q + \sigma^q \lambda^p \sum_{r \in \mathbf{v}_s} \mathbf{b}_{s,r} |\tilde{\delta}_s - \delta_r|^p \right\} \quad \text{Eq. 3.1}$$

Where δ_s , $\hat{\delta}_s$ and $\tilde{\delta}_s$ are the original pixel value, its recalculated value, and expected estimate, respectively. \mathbf{v}_s is the 8-neighborhood pixel set; $\mathbf{b}_{s,r}$ is the GGMRF potential; and σ and λ are scaling factors. The parameter $\mathbf{p} \in [1.01, 2.0]$ controls the smoothing level (e.g., $\mathbf{p} = 2$ for smooth versus $\mathbf{p} = 1.01$ for relatively abrupt edges). The parameter $\mathbf{q} \in [1, 2]$ determines the Gaussian ($\mathbf{q} = 2$) or Laplacian ($\mathbf{q} = 1$) prior distribution of the estimator[113]. Our simulations are conducted with $\sigma = 1$, $\lambda = 5$, $\mathbf{p} = 1.01$, $\mathbf{q} = 2$, and $\mathbf{b}_{s,r} = \sqrt{2}$ (see [111] for more details on GGMRF). The size of the neighborhood, n, has a great impact on the level of smoothing and needs to be adjusted for each application. An example of the input and output of the GGMRF method and their corresponding muscle activation segments is demonstrated in Fig 3.4.

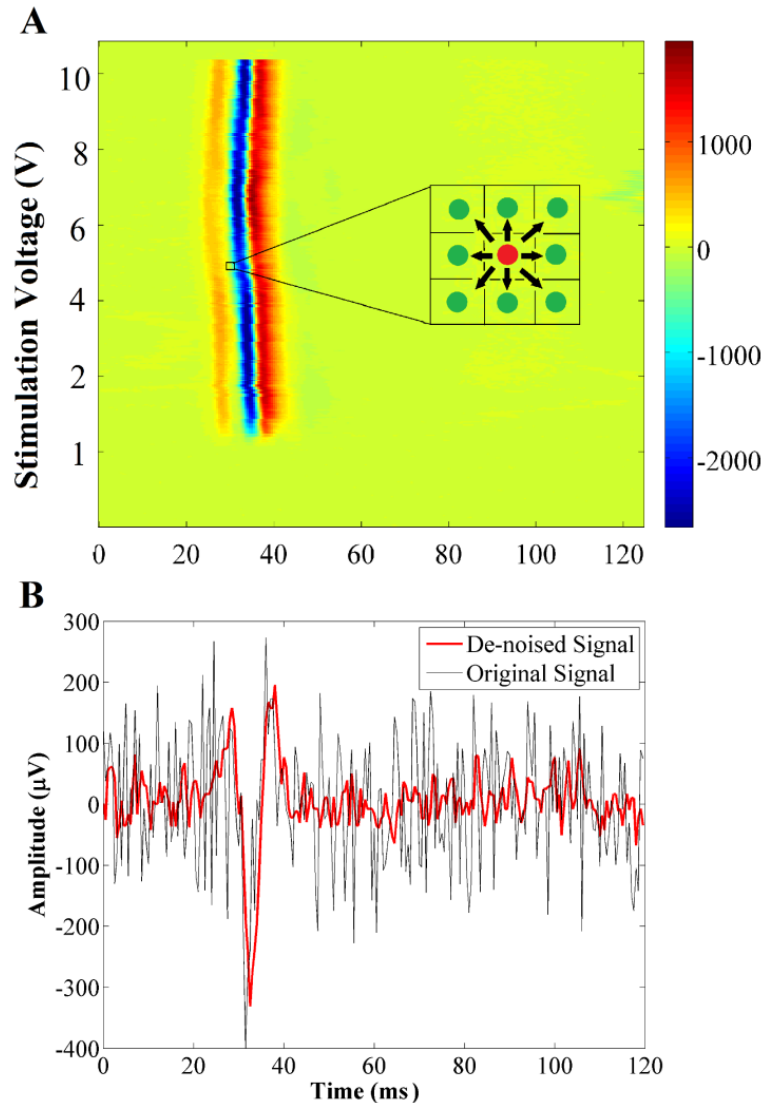


Fig 3.4 EMG Denoising Using GGMRF. (A) Applying GGMRF method to 2D image (B) and an example of evoked potential before (black) and after (red) applying GGMRF method.

Advantages of spatial smoothing of the EMG signals compared to the traditional band-pass filtering techniques, is that this method reduces EMG signal variability by offering the option of comparing each evoked potential with the previous and next one. Unlike the filtering methods, this image smoothing method offers a de-noised signal without any significant changes in the position or original shape of muscle activations.

Activation Detection

The activation detection algorithm is designed to determine the presence or absence of scES induced evoked potentials in each segment of the EMG signals and, consequently, the corresponding stimulation intensity threshold. The pre-assumptions for this task are: 1) the intensity threshold V_{s0} , which causes the emergence of the earliest evoked potentials, is an unknown random value with unknown distribution; and, 2) the amplitude of the first visible evoked potential is also an unknown value. These are valid assumptions because of the non-stationary nature of EMG signals and the fact that no *a priori* information regarding the distribution of the varying parameters is present. It is notable that these onset values alter based on the choice of the stimulation configuration, frequency and muscle type, and also subject to the day-to-day and pre-post training variability. As mentioned in section 2.1, scES delivers the minimum of five stimulation pulses per stimulus voltage referred to as an *event*, $(w_j, L_{n-1} \leq j \leq L_n)$ where $\min(L_n - L_{n-1}) = 5$. It is defined by clinical analysts that if 50 percent or more of the stimulation pulses corresponding to the same intensity (event) trigger evoked potentials, that intensity will be considered as the activation threshold voltage (V_{s0}).

The general technique implemented in this step is known as the statistically optimal decision (SOD) method. One of the well-known derivations of SOD is named approximated generalized likelihood-ratio (AGLR) detector that is developed by Staude and Wolf (1999). In this study, this method is modified and adapted to our activation detection application. There are three main phases to this activation detection method: in the first phase, each segment of the de-noised signal ($w_i \in W$) is modeled by a Gaussian probability density function (pdf) and the model parameters μ_i and σ_i are estimated using

the maximum likelihood estimation (MLE) method ($p_{\theta}(w_i)$). Fig 3.5B shows the histograms for one segment of an EMG and its estimated Gaussian distribution. From a statistical point of view, the activation detection method represents a binary selection between the null hypothesis H_0 that states “there is no significant change in the pdf $p_{\theta_0}(w_i)$ of the i^{th} segment of the signal” and the alternate hypothesis that states “there is a significant change in the parameters of pdf $p_{\theta_1}(w_i)$ ”[45]. Therefore, in the second phase, the Gaussian model of all the EMG segments will be compared to the Gaussian model of the background noise by the log-likelihood ratio (LLR) measure. Eq. 3.2 shows the general formulation of the LLR.

$$s_k = \ln \left(\frac{p_{\theta_1}(y_{i_k})}{p_{\theta_0}(y_{i_k})} \right) \quad \text{Eq. 3.2}$$

Where y_{i_k} is the k^{th} sampled-value of w_i segment after smoothing step. In order to reduce the high computational cost of this equation, it is assumed that the occurrence of the scES induced muscle activation does not change the mean μ of the Gaussian pdf and the most significant changes happen in the standard deviation σ_i of the pdf as shown in Fig 3.5C. Therefore, the Eq. 3.2 can be simplified to Eq. 3.3.

$$s_k = \ln \left(\frac{\sigma_0}{\sigma_i} \right) + \frac{1}{2} (y_{i_k} - \mu)^2 \left(\frac{1}{\sigma_0^2} - \frac{1}{\sigma_i^2} \right) \quad \text{Eq. 3.3}$$

The sum of all the s_k values over one segment is referred to as CUSUM value S_i and is calculated based on Eq. 3.4.

$$\begin{aligned} S_i &= \sum_{k=N_{i-1}}^{N_i} s_k \\ &= (N_i - N_{i-1} + 1) \ln \left(\frac{\sigma_0}{\sigma_i} \right) + \frac{(N_i - N_{i-1})}{2} \left(\frac{\sigma_i^2}{\sigma_0^2} - 1 \right) \quad \text{Eq. 3.4} \end{aligned}$$

Using Eq. 2.4, for each segment of the signal one value is calculated, which represents the highest statistical difference between that specific segment and the background noise (Fig 5D).

Finally, in the third phase of the algorithm, a dynamic threshold h is calculated for each EMG signal in order to find the first segment of the signal that includes the evoked potential and its corresponding stimulation intensity V_{s0} . Based on experimental observations, the first event corresponding to the lowest stimulation voltage does not usually trigger muscle activation; thus, this event can be considered as the baseline. Consequently, the threshold value h can be computed as the summation of the maximum and standard deviation of the set of S_i that belongs to the baseline (Eq. 3.5).

$$\mathbf{h} = \mathbf{S}_{max} + \sigma_{S_i} \quad \text{Eq. 3.5}$$

All the steps of the activation detection method are demonstrated in Fig 5. This step of the framework has been applied only to the voltage ramp-up experiments (at 2 Hz) where there is a single evoked potential in response to each stimulation pulse (after the muscle is activated) and the accurate detection of the muscle activation and its onset is desired.

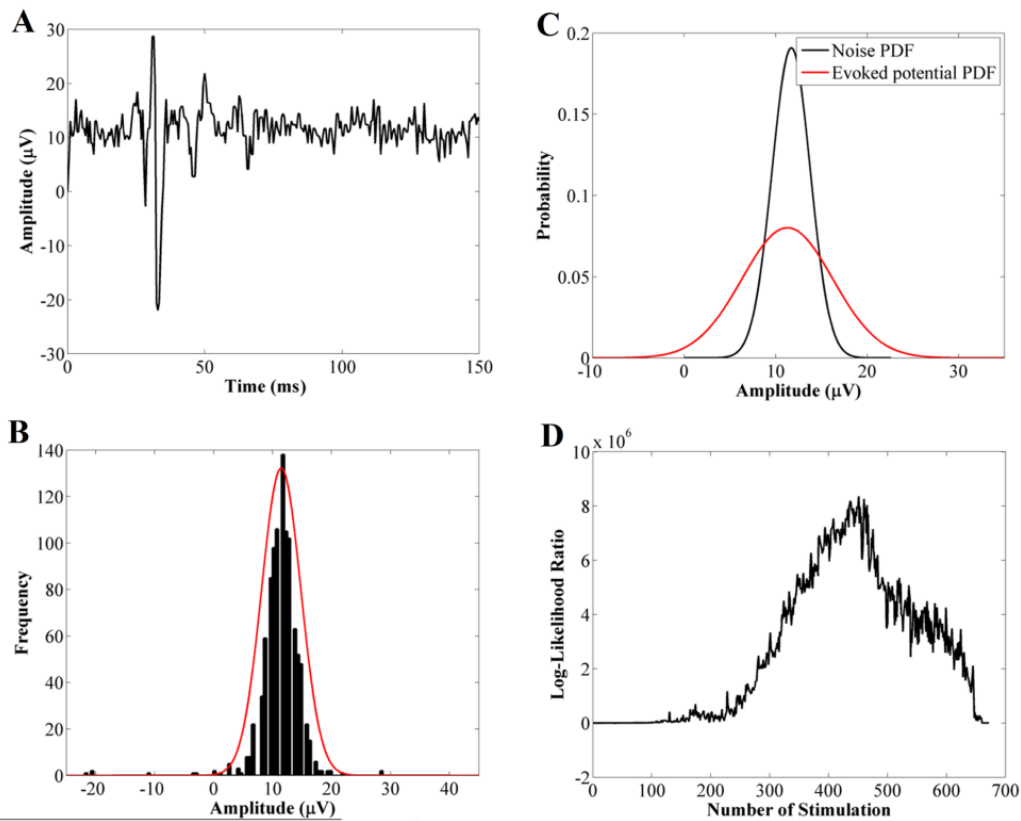


Fig 3.5 Activation Detection. Calculation steps for activation detection algorithm. (A) A sample evoked potential (one segment of the EMG signal), (B) Histogram of the sample evoked potential (black) and its estimated Gaussian distribution (red), (C) Comparing the Gaussian pdf of evoked potential signal (red) to pdf of background noise (black), (D) Plotting the calculated LLR for all segments of the EMG signal and detect the activation threshold (arrow).

Feature Extraction

The objective of the feature extraction algorithm is to represent each epidurally evoked potential with a set of key features. With this algorithm, the user has the flexibility to calculate these parameters automatically or observe visually using the 2-D representation of the EMG signal (Fig 3.6A). The automatically calculated parameters in this framework

are: peak-to-peak amplitude (V_{pp}), which is the absolute value of the difference between the highest and the lowest peaks (T_{pp}) in the evoked potentials and its normalized value based on the highest peak between left and right muscle; activation latency, the time interval between the stimulus onset and the onset of muscle activation, the time interval between the highest and lowest peak; integrated EMG value, the area under the motor unit curve after rectifying the EMG signal; and, finally, binary 0/1 values: an indication of the absence or presence of evoked potentials in each segment of the signal. The aforementioned features are illustrated in Fig 3.6B.

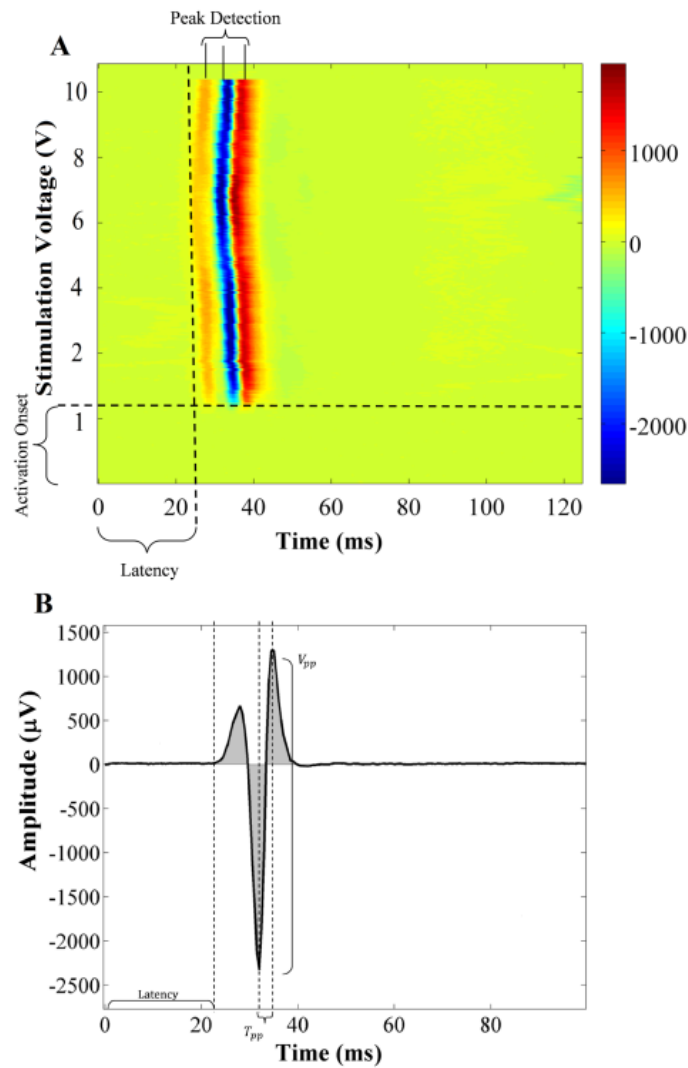


Fig 3.6 Feature Extraction. Selected feature parameters for EMG activation signal. (A) Visual inspection: Number of peaks of the evoked potential, Activation onset and Latency, (B) Computer-based feature extraction of peak-to-peak amplitude (V_{pp}), Activation latency, Time interval between minimum and maximum values (T_{pp}) and Integrated EMG (summation of absolute values of all gray areas).

Visualization

The last step of the framework is to represent the data processing results in an optimum and informative way to illustrate the connection between stimulation parameters and

results generated from the computer-based method for each muscle. This will create a valuable, efficient and convenient presentation of the data for the examiner to enhance interpretation and modify the experiments accordingly. Fig 3.7 shows examples of the transformation of 14 raw EMG signals into a single Colormap image for intensity ramp-up (Fig 3.7A and 3.7C) and frequency ramp-up experiments with the same stimulation configuration (Fig 3.7B and 3.7D). The Colormap values represent the peak-to-peak amplitudes for intensity ramp-up, after the automatic detection of scES-induced activation, and integrated EMG values for frequency ramp-up experiments.

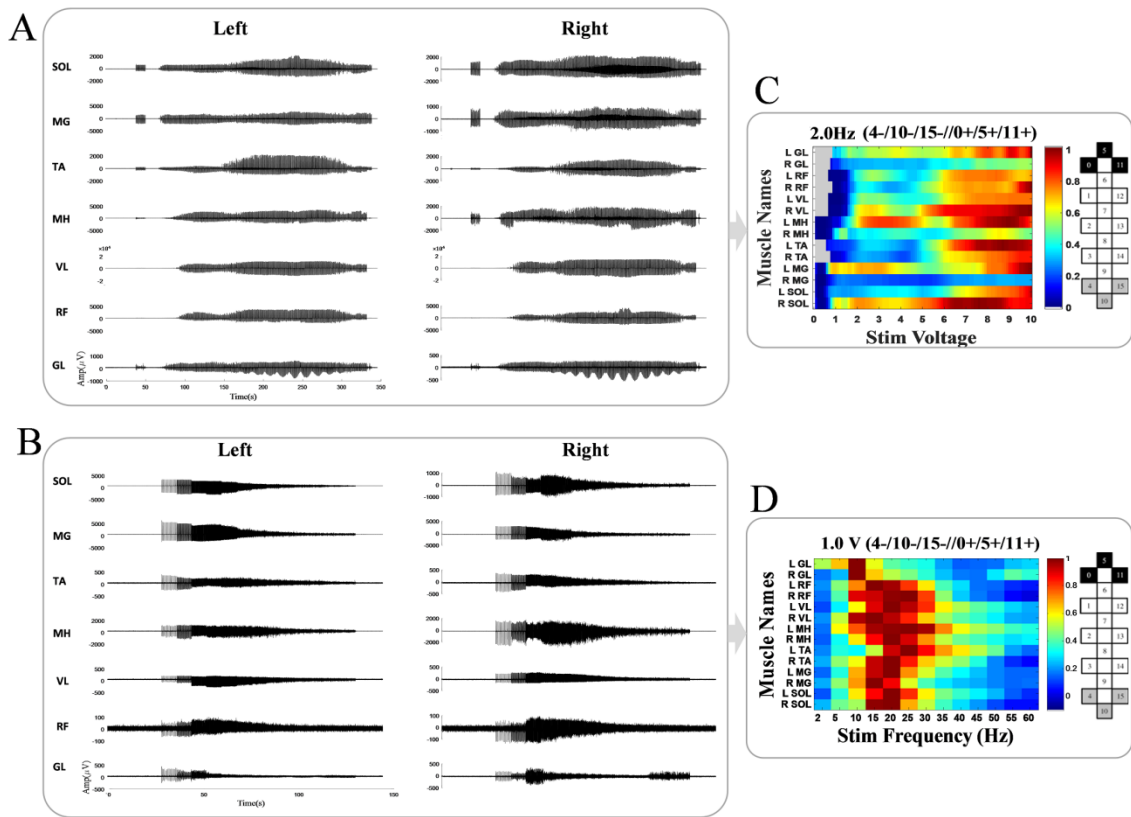


Fig 3.7 Colormap Visualization. Examples of converting 14 EMG signals into Colormap images for a voltage ramp-up and a frequency ramp-up experiment. (A) Raw EMG signals of 14 proximal and distal left and right leg muscles during voltage ramp-up from 0.1 to 10 V. (B) Raw EMG signals of same muscles during frequency ramp-up from 2 to 60 Hz. (C) Colormap image shows the corresponding peak-to-peak amplitudes (μV) with

respect to each muscle and stimulation voltage after stimulation threshold detection. The gray area is presenting the pre-threshold part of the experiment where no activation was induced. (D) Colormap image shows the corresponding integrated EMG values with respect to 14 muscles and stimulation frequencies.

The colormap visualization technique can be expanded for several ramp-up experiments where different configurations are tested for each subject. This is particularly helpful for the experimental analysts since it gives them the option for instantly comparing the results of several experiments together and decide on the optimum stimulation parameters selection. Examples of this form of colormap representation are demonstrated in the results section.

C. Results

In this section, the accuracy and speed of automating the mapping task is presented followed by a few examples of the clinical applications of the proposed framework. The performance of the computer-based activation detection algorithm has been evaluated by comparing the output of the algorithm with the output of the manually detected evoked potentials in intensity ramp-up experiments performed by trained data analysts, which is considered as the gold standard. The activation detection method presented is also compared with two other existing methods, Teager-Kaiser Energy Operation (TKEO) [39] and the AGLR method without the GGMRF smoothing step. The comparison is based on both recorded EMG signals and simulated signals. Finally, the runtimes of all the algorithms are presented.

a. Performance Evaluation Using Manual Activation Detection

This evaluation is based on calculating sensitivity, specificity, Dice similarity and accuracy as the performance metrics. These parameters are calculated based on true positive (TP), true negative (TN), false positive (FP), and false negative (FN) values. The boxplots of the four performance measurements on 700 EMG signals separated for each individual are shown in Fig 3.8.

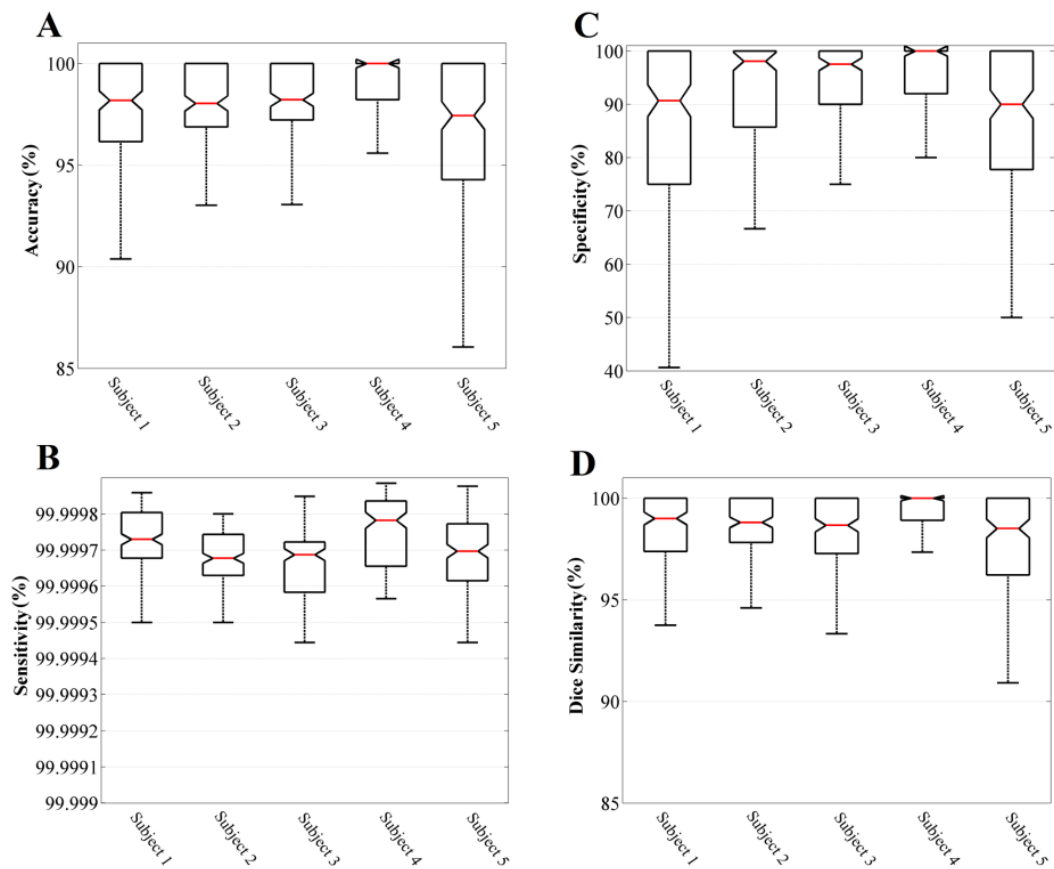


Fig 3.8 Performance Measures. Boxplot representation of performance measurements for comparing automated activation detection method with the manual ground truth. (A) Accuracy, (B) Sensitivity, (C) Specificity, (D) Dice Similarity

Looking at these values in Fig 3.8, it is immediately noticeable that the selected comparison measures (i.e. sensitivity, specificity, Dice similarity and accuracy) have

distributed in different ranges. For instance, the percentage of sensitivity values are densely distributed in [99.9994, 99.9999] interval whereas the specificity data points are distributed in [79.59, 99.99] or accuracy values are spread out between [94.33, 100.00]. These differences can be addressed based on the experimental design and the original definitions of these measures. For example, the sensitivity is the ratio of true positives over all the positive (activated) segments of the signal, and since during the intensity ramp-up usually most segments of the EMG signals contain evoked potentials, the true positive ratio is almost always close to 100%. On the other hand, the specificity values show the ratio of true negatives and since a few segments usually fall into the not-activated category, the accuracy of the program for detecting these segments can drop in some cases and cause in lower true negative ratio. The Dice similarity measure is usually used to quantify the amount of agreements between two sets of binary results and in this application these values are distributed in [96.29, 99.99].

b. Comparison with Other Activation Detection Methods

The performance of the automated method is compared to two other methods: TKEO and AGLR without smoothing. In this study, we slightly modified these algorithms to be adapted to the activation detection problem in order to make a fair comparison between their outputs and our proposed method. The TKEO method utilizes a conditioning function as shown in Eq. 3.6.

$$\Psi(x_{i_k}) = x_{i_k}^2 - x_{i_{k-1}}x_{i_{k+1}} \quad \text{Eq. 3.6}$$

Where x_{i_k} is the observation k in segment i . After applying the conditioning function, the maximum value of each segment is compared to the dynamic threshold (Eq. 2.5) and activation will be detected if the maximum value is greater than the threshold.

The comparison results are based on recorded EMG signals as well as simulated EMG signals.

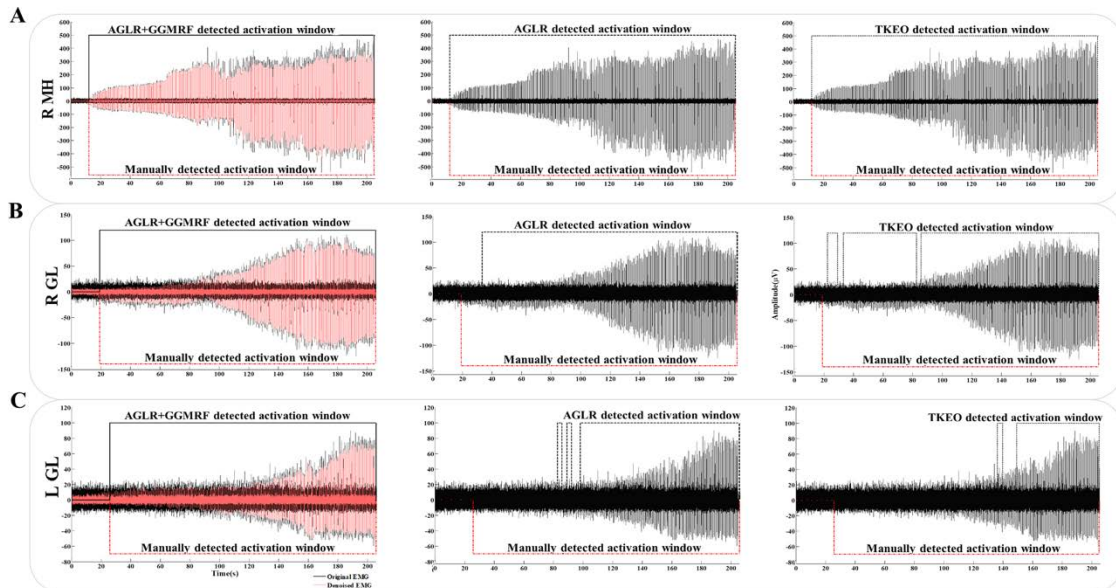
The results of comparing the proposed method with AGLR and TKEO based on the total accuracy in the recorded EMG signals from five patients are presented in Table 3.1 in the five-number-summary format. It is noticeable that AGLR and TKEO showed a lower accuracy compared to the new automated framework. Particularly there is approximately 1.05% increase in the median value of accuracy that shows the effect of adding the GGMRF smoothing technique to the pre-processing step, which makes the automated method more robust where there is higher noise level in the signal. It is notable here that although other signal filtering techniques might show the same robustness to noise, these methods cause distortion to the shape of the evoked potential or activation latency in the signal which are unfavorable in this application.

Table 3.1 Comparison with other activation detection methods. Comparison of the total accuracy for the new automated activation detection method with the TKEO and SODM methods based on five-number-summary

	SODM+GGMRF	SODM	TKEO
Maximum	100.00	100.00	100.00
Upper quartile	100.00	100.00	100.00
Median	100.00	98.95	98.42

Lower quartile	97.72	97.43	97.22
Minimum	94.33	93.65	93.18

Fig 3.9 demonstrates examples of recorded EMG signals with different SNR levels and performance comparison of the three methods for each signal. The three signals were recorded from right MH (Fig 3.9A), right GL (Fig 3.9B) and left GL (Fig 3.9C) during an intensity ramp-up experiment and they have high, medium and low SNR (10.63 dB, 4.37 dB and -0.14 dB), respectively². The performances of the three methods are shown as activation windows in black lines (from left to right: AGLR with GGMRF, AGLR and TKEO). The activation window is a time interval in which the algorithm was able to detect every single evoked potential induced by scES pulsations. The manually detected activation windows are shown in red dashed lines as the ground truth.



² SNR values are approximated by using the smoothed signals as the original signal without noise and the subtraction of recorded and smoothed signal as the noise signal (assuming that the noise is additive).

Fig 3.9 Examples of recorded EMG signals with high, medium and low SNRs and the performance comparison between three activation detection methods. (A) high SNR signal from right MH; (B) medium SNR signal from right GL and (C) low SNR signal from L GL. Detected activation windows for AGLR + MMGRF, AGLR and TKEO from left to right are shown as continues and dashed black lines. De-noised signal is shown in light red and manually detected activation window as dashed red line.

As this figure shows, for the high SNR signal all three methods can detect 100% of the evoked potentials in the signal. In the medium SNR, only AGLR with GGMRF can detect the activations as early as the ground truth. The AGLR without de-noising had near 15 seconds delay in detecting the first activation (accuracy of 94.11%). TKEO didn't show a long delay but it was unable to consistently detect all the activations throughout the signal (accuracy of 95.58%). In the last row, the left GL signal has low SNR and it causes a long delays and inconsistencies in detecting the activations for AGLR (69.11%) and TKEO (38.23%), however our algorithm is robust in detecting the earliest activations that are overwhelmed with the high noise level.

In order to measure the extent to which the proposed method keeps its robustness in the noisy environment, and compare it with other methods, the performances of the three methods were tested using the simulated signals with different SNR values. The simulated EMG signal is designed using an activation shape signal as the evoked potential, $X(k)$, that is convolved with a train of Dirac delta impulses $\sum_{n=1}^k 0.01n \delta(t - n)$, where the amplitudes linearly increase. The additive white Gaussian noise, $n(t)$, is then added to the signal based on the desired SNR to generate the final simulated signal. This signal consists of 50 segments, where the first 20 segments do not include any

evoked potential; thus, 10 segments of the first portion of the signal are utilized as the baseline. The SNR of the simulated signal is increased from -10 to 10 dB. Fig 3.10 demonstrates the plot of the accuracy measurement values versus SNR for three methods. As it is shown in this figure, all three methods are performing well at higher SNR values. However, as the noise level in the signal started to increase, TKEO and AGLR accuracy rates suddenly dropped to below 50% but the proposed method kept its accuracy near 80% at lower SNRs. Therefore, it is clear from this plot that the AGLR with GGMRF significantly outperforms the other methods for EMG signals containing lower SNR values.

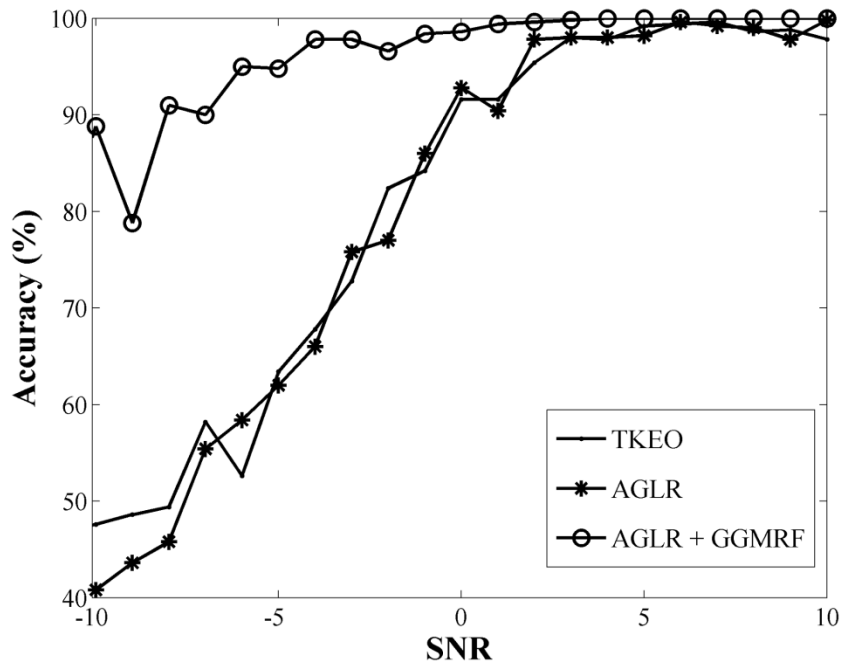


Fig 3.10 Comparison of the proposed activation detection algorithm with two other methods. Comparison of three activation detection methods, TKEO, SODM, and SODM with GGMRF on simulated signals as a function of SNR (dB).

c. Calculating Total Runtime of The Algorithms

The hardware and software that were employed to process the EMG signals and calculate the runtime of the algorithms are Dell computer with Optiplex 9020, Intel® Core™i7-4790 CPU @ 3.60 GHz, 16.0 GB RAM, 64-bit Operating System, and MATLAB R2011a, respectively. The runtime of this framework is directly dependent on the length of the experiments. Table 3,2 presents the average runtime of each of the five algorithms. The average and standard deviation of total execution time for processing each set of data recorded during one ramp-up experiment through all five algorithms is approximately 12.7 ± 2.3 seconds. Comparing to the previous manual method that could take up to several days, the automated method clearly demonstrates superior efficiency with respect to time and human resources.

Table 3.2 Runtime measurements. The runtime mean and RMSE of each steps of the proposed framework

		Converting					
		signal to	Noise	Activation	Feature		
		image	reduction	detection	extraction	Visualization	Total
Runtime	Mean						
(s)		3.93	6.61	1.54	0.05	0.40	12.71
	RMSE	1.33	1.18	0.24	0.01	0.01	2.33

D. Discussions

There are several points that need to be addressed in the process of developing the proposed automated framework for EMG signal processing. First, it is important to note that the presented method does not need any *a priori* information for the statistical model,

which makes it a fully automatic method that uses only the current and previous EMG signal values to build the statistical model. Also, there is no need to label the input data manually before running the program.

Comparing the results from recorded EMG signals and simulated signals with controllable SNR shows that in most cases surface EMG signals have fairly high SNR, which makes the performance of all the methods fairly accurate. However, there are some instances where the EMG signals can be disturbed with unpredictable sources of noise and artifacts like displacement of the recording electrodes or random occurrence of internal muscle activations that can interfere with the epidurally induced activations. As it was shown in the results section, adding the image-smoothing step to the framework helps to reduce the chance of false alarms (outliers) in the presence of these sources of noise. Since both TKEO and AGLR show rather accurate results without GGMRF, we predict that adding this pre-processing step to TKEO and probably other methods will also increase their accuracy significantly. It should also be mentioned that the GGMRF method itself is sensitive to the size of the neighborhood pixels and this parameter should be adjusted based on the application; therefore, adding this step can be a tradeoff between accuracy and the need for parameter adjustment.

In addition to internal activations there are some instances where there is a secondary (late) response to the scES stimulation that can overgrow the primary evoked potential and cause false alarms. In order to minimize the effects of these secondary responses on the program's accuracy, only the first one eighth of each signal segments are used to build the statistical model because this is the time interval where primary activations, that

are directly linked to the order of muscle recruitment of the scES, are most likely to happen.

As it was explained in the methodology section the program is designed to detect both the occurrence of evoked potentials and the latency (onset) of each detected evoked potential as one of the key features that has been extracted. Same statistical methodology with minor modifications has been applied for the onset detection algorithm. In order to increase the resolution of the detected onsets, the program increases the sampling rate to 10,000 samples per second in the recorded EMG signals using linear interpolation technique.

It should also be noted that while the manual activation detection has been considered as the gold standard in this study, the manual method itself has weaknesses such as disagreements between different observers in low SNRs or intra-observer variability in detecting the true onset that can be caused by exhaustion specially when facing large stack of data.

By reducing the noise level in the signal, while minimally affecting the evoked potential signal using the GGMRF technique and considerably increasing the signal-to-noise ratio (Fig 3.9), this framework increases the detection accuracy of the earliest muscle response in the EMG signal and the corresponding stimulation voltage (intensity) as the muscle activation threshold. In other words, this algorithm detects the exact intensity threshold that is needed for the muscle to get activated (for a given electrode configuration). Determining this threshold value has two main advantages for the experimentalist: 1) To find the configuration (or combination of several configurations) that offers the lowest intensity threshold for activating all the muscles; and 2) To set the intensity at the pre-

threshold value during the performance of specific voluntary tasks for the selected optimum configuration. Therefore, the automatic process of linking scES parameters to the muscle recruitment order that is presented in this study improves the speed and precision of the operator's decision for selecting both the optimum configuration and the corresponding pre-threshold intensity.

Finally, our framework has the flexibility to be applied to any other experimental protocols or signals, by simply updating certain parameters (e.g. intensity or frequency) and attributes (e.g. peak-to-peak amplitude or integrated EMG) of the signals. Spinal cord epidural stimulation research has current applications in small and large animal models as well as human models. In all models, understanding the effect of scES on the spinal cord networks following injury is a critical component that will lead to more successful selection of stimulation parameters targeted for functional improvements. As we have shown in our previous works (3-6) stimulation configurations are different across individuals, species and tasks, emphasizing the need to map motor evoked responses relative to stimulation site for each research participant. Transcutaneous stimulation has also been used as a technique to access the capabilities of the spinal cord networks following injury. Thus, the methodology presented in this paper can also be used to visualize the motor evoked responses relative to stimulation site and stimulation voltage across multiple muscles. Applications in which understanding detailed responses of multiple muscles to a stimulus with varying intensity and location could benefit from the analysis technique explained in this paper.

E. Application I: Finding optimized electrode configuration

Functional application of scES mapping and colormap visualization technique is presented here to show the practical convenience and effectiveness of the proposed framework. Here we present the results of performing 12 voltage ramp-up experiments with different stimulation configurations for one of the participants. Fig 3.11A illustrates the peak-to-peak amplitudes of left and right RF and VL muscles with respect to 12 middle column configurations and the stimulation voltage. These graphs help the examiner to determine which configuration showed the best performance for a given muscle. At the same time the data from the systolic blood pressure (SBP) was also recorded during all 12 experiments and using similar methodology to EMG we were able to generate similar colormap with respect to configuration and intensity (Fig 3.11B). The SBP colormap was further divided into two colormaps: one before a certain muscle (R VL in this example) gets activated (Fig 3.11B left) and one after the muscle starts to show activations (Fig 3.11B right). This way the examiners can observe the effects of muscle activation on SBP data. Before the mapping experiments had been done, during the voluntary movement experiments[14], the individual was asked to try to extend their knee (Fig 3.11C) by setting the stimulation parameters to 1-/6-/12-//7+/8+, 3.3 V and 25 Hz for configuration, intensity and frequency, respectively (Fig 3.11D). However, the selected configuration was not optimum and did not result in a proper movement. The experimental analysts then used the mapping colormap images for this subject to determine that the electrode selection for this subject should be moved upward on the stimulation array according to the EMG colormaps for RF and VL which show that middle column configurations near the top of the array (7-//6+;7-//8+) caused the earliest activations with low SBP. Therefore, the stimulation parameters were adjusted to (0-/1-

/5-/8-/11-/12-/13-//6+/7+, 3.1 V and 25 Hz (Fig 3.11E) for voluntary movement experiment and resulted in proper knee extension.

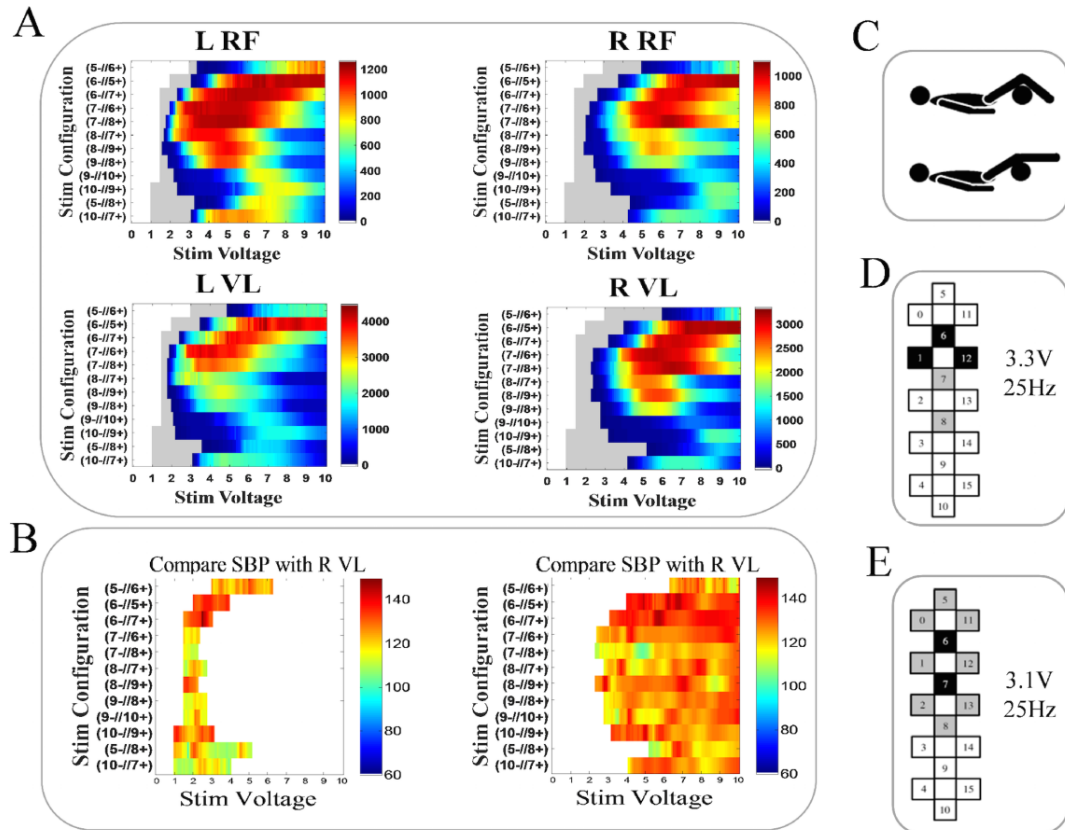


Fig 3.11 Functional application of scES mapping and visualization technique. (A) Colormap figures for middle column configurations for 2 selected muscles (left and right RF and VL) used to identify optimal configurations for voluntary activity (knee extension) in a research participant. The white area in the images shows that at which stimulation voltage the experiment started and the gray area shows the pre-threshold part of the experiments. (B) SBP data with respect to stimulation configurations when the R VL muscle is off (left) and when it is on (right) (C) stick figure representing movement. (D) Successful but not optimal configuration designed for knee extension (E) Optimized configuration for knee extension. In the graphical representation cathodes are black, anodes are graph and assigned electrodes are white.

F. Application II: Repeatability Measures of Epidurally Induced Motor Evoked Potentials in Individuals with Spinal Cord Injury

This application of the developed framework aims at quantifying the variability of the recorded Spinal cord evoked potentials (scEPs) caused by controlled and uncontrolled experimental factors during Spinal cord epidural stimulation (scES). It has been shown previously that scES along with activity-based training can promote the recovery of motor functions after chronic motor complete spinal cord injuries (SCI). The appropriate selection of scES parameters, which are most often task- and individual-specific, is crucial for promoting motor recovery. In order to facilitate the selection of proper stimulation parameters, an individualized map of motor pools activation is defined by combining the scEPs induced by various stimulation parameters recorded over multiple experimental trials with the research participants in supine position. However, to date, the reliability of these scEP recordings used in building the map has not been investigated and the effects of changing the stimulation parameters on the variability of scEPs have not been quantified. In this study, the experimental procedures were performed on 10 individuals with motor complete SCI in supine position using various scES parameters, i.e. intensity, electrode combinations and their polarity. The EMG signals were recorded from 16 leg muscles in repeated experiments performed one to seven days apart. The scEPs were detected from the recorded EMG signals and the peak-to-peak amplitude and activation threshold of each scEP were extracted. Linear mixed-effects models were used to quantify the amount of variability in amplitude and threshold measurements that is caused by each controlled and uncontrolled experimental factor. Figure 3.12 demonstrates the recruitment curves of 4 selected muscles (left VL, MH, TA and SOL)

corresponding to 4 electrode configurations for subject A59. The selected configurations stimulate different parts of the electrode array. For instance, the 5-//6+ configuration in Fig 3.12 A is stimulating the top part of the array, 8-//7+ (Fig 3.12 B) stimulates the middle part, 10-//9+ (Fig 3.12 C) stimulates the bottom part of the array and in Fig 3.12 D the 4-/10-/15-//0+/5+/11+ configuration targets a wide field and non-location specific stimulation. This figure shows that the threshold values (red circle and X markers) occur very closely on the two subsequent trials for most of the muscles and configurations; whereas the amplitude criterion tends to grow further apart between the two trials as the stimulation intensity increases but this trend is subjective to the muscle and configuration. On the other hand, the curvature of the activation patterns remains rather unchanged between the two trials in all the muscles and electrode configurations depicted in these plots. It is also notable from Fig 3.12 D that the wide-field configuration activates the muscles almost simultaneously at very low intensities (0.5~0.6V) but the narrow-field configurations, located at the top and middle part of the electrode array (Fig 3.12 A and B), need higher stimulation intensities to activate the muscles.

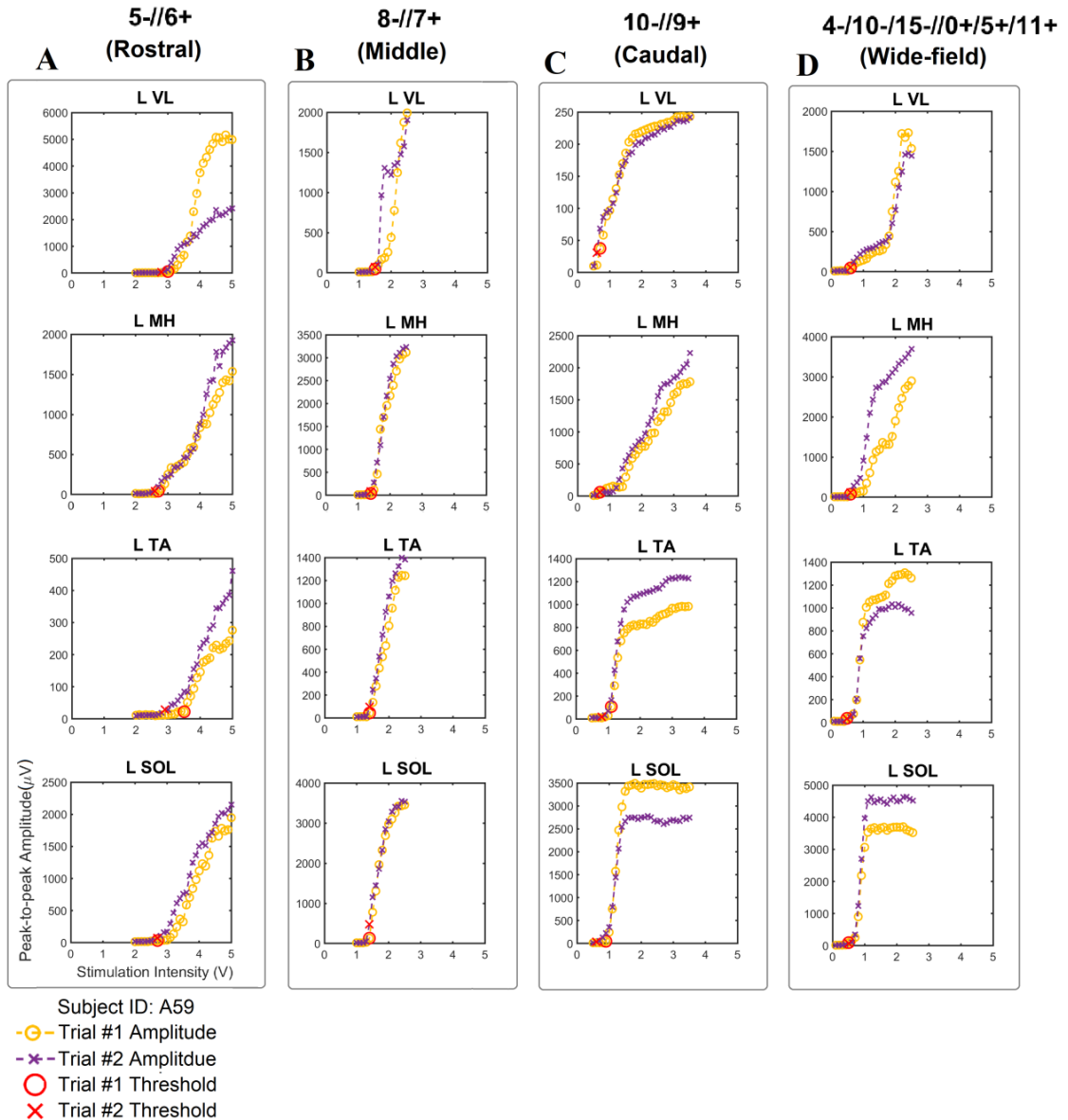


Fig 3.12 The recruitment curves of left VL, MH, TA and SOL muscles of Trial #1 and Trial #2 amplitude and threshold values with stimulation configuration (A) 5-//6+ rostral part of the electrode array; (B) 8-//7+ middle part of the electrode array; (C) 10-//9+ caudal part of the electrode array; (D) 4-//10-//15-//0+/5+/11+ wide-field configuration.

a. Linear Mixed-effects Models

The reliability analysis of the sCEP amplitude and threshold measurements using linear mixed effects multi regression models are summarized in Tables 3.3 and 3.4,

respectively. The standard deviation values estimated for each experimental factor and factor interactions are presented separately for surface and indwelling electrode measurements.

Table 3.3. Estimated components of the total variation in $\log A$, σ , (approximate components of relative variation in A) and their 95% confidence intervals (CI) for surface and indwelling electrodes measurements.

Surface Electrodes Measurements				Indwelling Electrodes Measurements (IL Muscles)		
Factor	σ	CI		σ	CI	
		Lower	Upper		Lower	Upper
Research Participant	0.590	0.331	1.046	0.927	0.508	1.603
Experimental Pair	0.761	0.656	0.889	0.944	0.597	1.244
Muscle	0.673	0.470	1.026	0.016	0.000	0.761
Intensity	1.556	1.350	1.810	1.074	0.896	1.289
Muscle Exp. Pair	1.012	0.976	1.050	0.923	0.740	1.165
Intensity Exp. Pair	0.393	0.381	0.405	— ^a	—	—
Muscle Intensity	0.234	0.220	0.249	— ^a	—	—
Muscle Intensity Experimental Pair	0.084	0.061	0.102	— ^a	—	—
Residual	0.537	0.534	0.541	0.864	0.845	0.883

^a There were insufficient data to estimate these interaction effects.

Table 3.4. Estimated components of the total variation in I_t , σ , and their 95% confidence intervals (CI) for surface and indwelling electrodes measurements.

Surface Electrodes Measurements				Indwelling Electrodes Measurements (IL Muscles)		
Factor	σ	CI		σ	CI	
		Lower	Upper		Lower	Upper
Research Participant	0.602	0.322	1.025	0.660	0.330	1.152
Experimental Pair	0.854	0.750	0.983	0.795	0.606	0.995
Muscle	0.118	0.075	0.193	— ^a	—	—
Muscle Exp. Pair	0.519	0.496	0.544	0.491	0.300	0.686
Residual	0.385	0.372	0.399	0.664	0.441	0.664

^a There were insufficient data to estimate the effect of this factor.

The residual values (Residual) presented in Tables 3.3 and 3.4 reflect the amount of variability caused by uncontrolled technical and physiological factors in subsequent trials, i.e. the inter-trial variability. It is noticeable that the residual values are lower than most of the independent factors for both amplitude and threshold criteria. The stimulation intensity shows the highest variation in the amplitude measurements, while the experimental pair factor, which includes research participant and electrode configuration, presents the highest variability in threshold measurements for both surface and indwelling recordings.

Table 3.3 and 3.4 also report the factor interactions that were included in the linear mixed effects models. Amongst the factor interactions that were considered in the models, only “muscle | experimental pair” showed higher variability than residuals for both scEP amplitude and threshold. This means that a given muscle responded differently across different subjects and electrode configurations.

b. Comparison between Inter-Trial Variability of the Amplitude and Threshold Criteria

In order to compare the residual values for the amplitude and threshold measurements, we fitted the same MLE model to the $\log(I_t)$ measurements. The residual standard deviation and its 95% confidence interval of this model are 0.186, [0.180, 0.193] for the surface measurements and 0.274, [0.245, 0.309] for indwelling measurements. In this form, the residuals of the two models for the logarithmically transformed measurements are approximately equal to the coefficient of variation of the original (non-transformed) measurements [114]. Therefore, the coefficient of variation value of the threshold measurements is 33% of the coefficient of variation for the amplitude (Table 3.4) recorded by surface electrodes, and 31% for the amplitude measurements recorded by indwelling electrodes. Seen as the 95% confidence intervals of the residuals for the two models do not overlap, they are considered significantly different. In other words, the inter-trial variability of the amplitude criterion is significantly higher than the inter-trial variability of the threshold criterion.

c. Bootstrapping and Intra-class Correlation Coefficient

Using the bootstrapping method, the null hypothesis of equal measurements in subsequent trials was tested. Based on this analysis, with $p=0.100$ the equal assumption

for peak-to-peak amplitude values obtained from surface electrodes cannot not be rejected. Moreover, for threshold measurements obtained from surface electrodes, the hypothesis of equal values between trial #1 and #2 is not rejected with p-value = 0.854. Also for the indwelling electrode measurements, with p-values equal to 0.327 and 0.430 for amplitude and threshold criteria, respectively, the hypothesis of equal values between trial #1 and #2 cannot be rejected. The intra-class correlation coefficient, and corresponding level of agreements according to Indrayan and Chawla [115]) were calculated for the same muscle in the same participant under the same experimental conditions, i.e. stimulation intensity and electrode configuration, to show how closely the measurements recorded on the repeated trials are compared to the first trial. The intra-class correlation coefficient numbers for the surface and indwelling measurements of the amplitude values are equal to 0.946 and 0.921, respectively, which both correspond to excellent agreements between the recorded measurements on subsequent trials. For the threshold measurements, the intra-class correlation coefficient values are equal to 0.903 (Excellent) and 0.748 (Moderate) for surface and indwelling electrodes, respectively.

The results of this study show that the recorded measurements (amplitude and threshold) on subsequent trials were not significantly different when all the controlled experimental factors remained fixed. These results also verify that changing the controlled factors including stimulation parameters causes higher variation in the scEP measurements than any uncontrolled sources of variability. The findings also show that the coefficient of variation of amplitude measurements recorded on repeated trials is significantly higher than that observed for threshold measurements. These findings suggest that scEPs

recorded in experiments performed within one week are reliable measurements to map the effects of scES parameters on muscle activation patterns.

G. Study Outcomes

Our EMG signal processing efforts in the time domain resulted in two journal papers: one is published in PLOS ONE journal and the other one is under review in the journal of Electromyography and Kinesiology. The results of this study have also been presented as oral and poster presentations in 2018 Biomedical Engineering Society (BMES) conference and 2016 Research Louisville. Additionally, the EMG processing framework has been filed as a patent disclosure by the University of Louisville Technology Transfer office.

CHAPTER IV

NEUROPHYSIOLOGICAL MARKERS PREDICTING INDEPENDENT STANDING ENABLED BY SPINAL CORD EPIDURAL STIMULATION

A. Introduction

Spinal cord epidural stimulation (scES) along with activity-based training has been proven to be effective in re-enabling independent standing, walking over ground and voluntary movements in individuals with severe spinal cord injury (SCI) [8-14, 116, 117]. In order to successfully facilitate motor recovery, the stimulation parameters (intensity, frequency, electrode configuration) need to be adjusted for each individual and each task [116]. The ability to stand with independent lower limb extension is a key achievement toward the recovery of functional mobility, and it was consistently observed in all three motor complete SCI individuals previously reported and subsequently they recovered over ground stepping and walking [8, 12]. The guidelines proposed for selecting a sub-set of electrode configurations to be tested for standing include adjusting cathodes (active electrodes) position in order to target primarily extensors muscle groups according to the individualized map of motor pools activation [116, 118]. Also, the use of multiple interleaving programs represents an important advantage compared to the use of a single program, as it allows to access different locations of the spinal circuitry with different intensities. However, to date there are no available algorithms or procedures that suggest the exact set of parameters to be applied for facilitating standing using tonic scES. In

addition, the characteristics of muscle activation patterns leading to independent standing remain poorly understood.

Characteristics of Muscle Activation Patterns

Electromyogram (EMG) activities recorded from lower limb skeletal muscles have been used to characterize muscle activation patterns during the performance of various tasks enabled by scES [11]. These signals carry important information regarding the electrophysiological properties of the muscle response to epidural stimulation and sensory information. Spectral analysis of EMG signals and extracting key features from the time and frequency domains can also provide information related to characteristics of the neural drive, number of recruited motor units and their firing rates, and the type of engaged muscle fibers during various performance conditions of specific task [119]. Understanding the characteristics of muscle activation patterns leading to independent standing can be essential for developing a machine learning approach that can contribute to the selection of appropriate scES parameters. This is of particular interest at the early stages of spinal stimulation application, when it is likely that none of the tested stimulation configurations promote independent extension of any lower limb segment.

Here, we introduce a novel framework for EMG data processing that implements spectral analysis and machine learning methods for characterizing EMG activity resulting in independent or assisted standing, and for identifying the stimulation parameters that promote muscle activation more effective for standing. We initially determined which spectral analysis method is more effective for identifying frequency-domain EMG features that characterize independent standing promoted by scES in humans with clinically motor complete SCI. We then integrated EMG frequency- and time-domain

features in the computational model and tested its ability to accurately classify independent and assisted standing. Also, the physiological characteristics of EMG activity resulting in assisted and independent standing were defined. Finally, we applied the proposed framework on EMG datasets collected while research participants were testing different scES stimulation parameters for standing, with the goal of ranking the effectiveness of the muscle activation patterns generated. In this study, the EMG signals recorded during standing with scES are analyzed using FFT, STFT and CWT in order to draw comparisons between the amount of useful information they provide regarding the spectral content of the recorded EMG. A classification method will be applied to the features extracted from these three methods to assess the effectiveness of these features in quantifying standing ability in SCI individuals using scES.

B. Materials and Methods

a. Research Participants

Eleven participants (10 male and 1 female) with chronic motor complete SCI who have been implanted with scES (Fig 1A) were included in this study. All participants presented stable medical conditions with no progressive spinal cord injury and no drug abuse at the time of implantation followed by the experiments. The age of participants ranged from 23.38 to 36.19 years with mean and standard deviation of 28.78 ± 4.5 ; time since injury in these individuals ranged from 3.12 to 8.46 (5.02 ± 1.83) years at the time of standing experiments. The written informed consent for the entire experimental procedure and publications of research outcomes, which were approved by the University of Louisville Institutional Review Board, were provided by all participants. The research participants were recruited over 6 years (2009 to 2015), and were enrolled into an

interventional study focused on either the facilitation of standing and stepping or the recovery of cardiovascular function.

Table 4.1 Clinical characteristics of the research participants.

ID	Age (yrs)	Sex	Duration of Injury (Yrs)	Neurological Level	AIS Grade	AIS Score					
						Sensory (T10 - S5, core out of 24)				Motor (lower extremity)	
						L LT	L PP	R LT	R PP	L	R
B13	33	M	4.2	C7	B	10	10	10	8	0	0
B07	24	M	3.4	T2	B	15	11	18	10	0	0
A45	24	M	2.2	T4	A	0	0	0	0	0	0
A53	27	M	2.3	T4	A	0	0	0	0	0	0
B23	32	M	3.3	C5	B	8	0	10	0	0	0
A59	26	M	2.5	T4	A	0	0	0	0	0	0
B30	22	F	3.3	T1	B	17	5	17	9	0	0
A60	23	M	3.1	T4	A	0	0	0	0	0	0
A68	35	M	3.8	C4	A	0	0	0	0	0	0
A41	24	M	7.2	C4	A	0	0	0	0	0	0
B21	31	M	7.0	C4	B	1	1	0	0	0	0

b. Surgical implantation of electrode array and stimulator

The epidural spinal cord stimulation unit (Medtronic, RestoreAdvanced) and the 16-electrode array (Medtronic, 5-6-5 Specify) were surgically implanted in the eleven research participants (Fig 4.1 A). The electrode array was positioned over the midline of the exposed dura, in correspondence of spinal segments L1-S1/S2. EMG recordings from leg muscles were obtained intraoperatively during spinal stimulation at 2 Hz using midline, left and right electrode pairs in order to localize the optimal placement of the array. The wire leads were then internalized and tunneled subcutaneously to the abdomen and connected to the neurostimulator.

c. Experimental Procedure

Standing experiments were performed with participants standing over ground in a standing frame while the spinal cord was epidurally stimulated. If needed, participants received external assistance for hips and knees extension (Fig 4.1 B). Various stimulation parameters including the stimulation intensity, frequency and electrode array selection were tested for each individual to promote independent standing before and after activity-based training.

Selection of scES parameters for standing

A subset of scES parameters aimed at facilitating standing were initially identified based on the individual-mapping of scES pattern activation from previous assessments performed on the same research participants in supine position as well as from the literature. scES was initially delivered at a near-motor threshold stimulation amplitude that did not elicit directly lower limb movements in sitting. scES parameters were then adjusted during standing, for example unbalancing anodes and cathodes between the lateral columns of the electrode array to compensate activation differences between left and right lower limb, or adding interleaving stimulation programs to facilitate the activation of specific muscle groups. Also, stimulation frequency and amplitude were modulated synergistically in order to identify the higher stimulation frequency that elicited a continuous (non-rhythmic) EMG pattern effective to bear body weight.

Each research participant underwent one or two experimental sessions aimed at selecting appropriate scES parameters for standing prior to the beginning of stand training. Stimulation parameters were also adjusted throughout stand training. In particular, dedicated sessions were performed approximately every 2-4 weeks to monitor motor

behavior and lower limb EMG activity while testing different stimulation parameters to contribute to their selection.

EMG Signal Acquisition

EMG, ground reaction forces and kinematics data were recorded at 2000 Hz using a custom-written acquisition software (National Instruments, Austin, TX). The EMG signals were recorded during standing from 16 leg muscles using surface electrodes for left and right soleus (SOL), medial gastrocnemius (MG), tibialis anterior (TA), vastus lateralis (VL), rectus femoris (RF), medial hamstrings (MH), and gluteus maximus (GL) and two indwelling electrodes for left and right iliopsoas (IL) muscles. Figure 4.1 C and D show examples of the recorded EMG signals from left SOL muscle during hip and knees assisted and independent standing conditions, respectively.

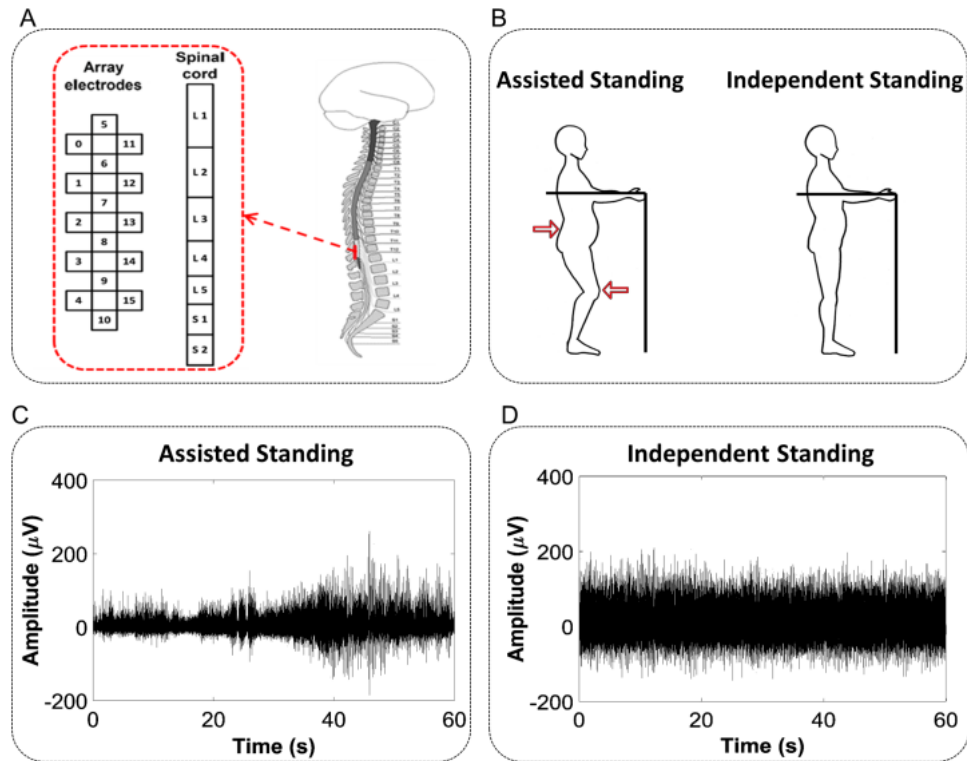


Fig 4.1 (A) The spinal cord epidural stimulation and its location on the human spinal cord; (B) Schematic view of the standing task; (C) Example of the recorded EMG signal from left SOL during one minute of assisted standing and (D) Independent standing.

d. EMG time and frequency domain analysis

Each standing event considered for analysis was characterized by consistent external assistance and stimulation parameters and a duration ranging between 40 and 70 seconds; the initial and final 5 seconds of each event were not considered for analysis. Each event was labeled as follow, based on whether hips and knees needed external assistance for standing or achieved independent extension: hips and knees assisted; hips assisted and knees independent; hips and knees independent; one knee assisted and one knee independent.

The EMG processing framework consisted of several steps including spectral analysis, time- and frequency-domain features extraction, dimension reduction, classification and prediction, which are described here below.

EMG time domain features

The EMG pattern variability was assessed by calculating the coefficient of variation (standard deviation / mean) of the linear envelope EMG obtained by filtering the rectified EMG signal through a low-pass digital filter (cutoff frequency: 4 Hz) [11].

The EMG total power was calculated using the following equation:

$$P = \frac{1}{T} \int_0^T |x(t)|^2 dt \quad (4.1)$$

Where $x(t)$ is the recorded EMG signal and T is the length of the signal.

For each examined muscle, the total power was then normalized by the maximum value detected within each participant.

Spectral analysis

In this study, we initially applied three spectral analysis methods to the scES-promoted EMG activity, with the goal of identifying the method that better differentiate conditions of assisted standing and independent standing based on the spectral information provided. Fast Fourier Transform (FFT) is the most commonly used method for spectral analysis of EMG signals [120]. It is characterized by high frequency resolution and poor time resolution, and cannot localize the frequency content of the

signal in the time domain. Short-Time Fourier Transform (STFT) was designed to increase the time resolution of FFT by selecting a fixed-size window moving across the EMG signal [121]. Finally, Continuous Wavelet Transform (CWT) has been designed to effectively localize the frequency content of non-stationary signals in both time and frequency domains by using size adjustable wavelets and therefor without compromising time or frequency resolutions [52, 53, 119].

EMG Frequency domain features

Power spectral density (PSD) of FFT, STFT spectrogram ($s(t, f)$) and CWT scalogram ($p(f, t)$) (using Morlet wavelet, $\psi_{f,t}(\tau)$) were calculated as reported in equations 4.2 to 4.4, respectively.

$$FFT(f) = \int x(\tau) \exp(-j2\pi f\tau) d\tau,$$

$$PSD(f) = |FFT(f)|^2 \quad (4.2)$$

$$STFT(t, f) = \int w^*(\tau - t)x(\tau) \exp(-j2\pi f\tau) d\tau,$$

$$\text{STFT Spectrogram: } s(t, f) = |STFT(t, f)|^2 \quad (4.3)$$

$$CWT(f, t) = \int x(\tau) \psi_{f,t}^*(\tau) d\tau,$$

$$\text{Morlet wavelet: } \psi_{f,t}(\tau) = \frac{1}{\sqrt{f_0/f}} \psi(\tau - t/(f_0/f)),$$

$$\text{Wavelet scalogram: } p(f, t) = |CWT(f, t)|^2 \quad (4.4)$$

Where f_0 is the sampling frequency (2 kHz).

The STFT window size was selected at 0.3 seconds to increase the time resolution of FFT and minimally compromising the frequency resolution.

Mean frequency, median frequency, dominant frequency, and maximum power are the physiologically relevant features that were extracted from FFT outputs.

For STFT and CWT, instantaneous values of mean frequency (IMNF), median frequency (IMDF), dominant frequency ($F_{\max}(t)$) and maximum power ($P_{\max}(t)$) were calculated (Eq. 4.5-4.8), and their average and standard deviation (SD) were considered as features for further analysis. In particular, EMG maximum power variability was assessed by calculating its coefficient of variation (SD / mean).

$$IMNF(t) = \frac{\sum_{j=1}^M f_j p(f_j, t)}{\sum_{j=1}^M p(f_j, t)} \quad (4.5)$$

$$\sum_{j=1}^{IMDF(t)} p(f_j, t) = \sum_{j=IMDF(t)}^M p(f_j, t) \quad (4.6)$$

$$F_{\max}(t) = \operatorname{argmax}_f(p(f, t)) \quad (4.7)$$

$$P_{\max}(t) = \max_f(p(f, t)) \quad (4.8)$$

where M is the number of frequency bins.

e. Classification

All the calculated EMG feature values (predictors) were normalized to their maximum to remove the effects of their units in the classification step. The non-negative

matrix factorization (NNMF) algorithm was applied to the normalized measurements for dimensionality reduction [122] and the output values were logarithmically transformed in order to stabilize the variance [123]. We then performed preliminary analysis to determine which classification method resulted in the highest accuracy for classifying conditions of assisted standing versus independent standing based on the EMG features herein considered. In particular, K-nearest neighbor (KNN) [124] performed better than Naïve Bayes [125], binary Support Vector Machine [126], and ensemble decision trees [127]; therefore, KNN was the classification method applied in the present study.

- The KNN classifier includes several parameters that need to be adjusted in order to achieve its best classification performance. These parameters include number of neighbors, distance measures, distance weights and standardization (centering and scaling the predictors). In order to find the optimized parameters for the classifier, the Bayesian optimization algorithm was used [128]. The objective function for the optimization is $\log(1 + \text{Cross Validation Loss})$. The Cross-Validation Loss is the ratio of misclassified observations during the cross-validation step. The classification accuracy is calculated using 10-fold cross validation method and calculated as a percentage value of $1 - \text{Cross Validation Loss}$ [125]. The KNN classifier with the parameter optimization algorithm and the cross-validation step were iterated 10 times and the average accuracy values and the 95% confidence intervals are reported.

f. Prediction

All calculated EMG feature vectors (time- and CWT-derived features) that we included in the classification step were then used as a training dataset for the prediction part of the framework. A trained model is defined as a model that has captured the

patterns in the training dataset. Based on these learnt patterns, the trained model can predict the class label (i.e. assisted or independent standing) for new observations that were not included in the training dataset.

For this part of the study, we developed KNN models that are trained for each investigated muscle pair (i.e. left and right soleus). These models were then used to predict the class labels for the prediction dataset, which includes assisted standing events collected from 6 research participants during experimental sessions aimed at testing the effectiveness of different scES parameters for standing. The output of the prediction step is a score value ranging from 0 and 1, which is the posterior probability $P(C|X_{new})$ of “independent standing” class C given a new observation X_{new} (Eq. 4.9).

$$P(C|X_{new}) = \frac{\sum_{i=1}^K W(X_i)1_{X_i=C}}{\sum_{i=1}^K W(X_i)} \quad (4.9)$$

Where K is the number of nearest neighbors to X_{new} , X_i is the i^{th} nearest neighbor, $W(X_i)$ is the weight of X_i which is the distance value from X_{new} and normalized based on the class prior probability, i.e. the frequency of the number of observations in one class in the training dataset. The $1_{X_i=C}$ function returns 1 if observation X_i belongs to class C and 0 otherwise [129].

For each muscle, score values equal or less than 0.5 assign the given observation to the “assisted standing” class label, while values greater than 0.5 assign the observation to the “independent standing” class label. The number of neighbors for the prediction task is set to $K = 5$; this keeps the classification accuracy high for all muscle pairs and allows

comparison of the prediction scores between KNN models. All EMG analysis steps are performed using MATLAB R2017b software and its Statistics and Machine Learning Toolbox.

g. Statistical analysis

Statistical analysis was performed using GraphPad Prism (version 5.00 for Windows, GraphPad Software, San Diego, California, USA). A P value < 0.05 was considered statistically significant. The distribution of quantitative EMG variables was tested for normality using the Kolmogorov–Smirnov test, and the parametric or non-parametric tests reported below were applied accordingly. The effect of assisted or independent standing on the EMG features considered (total power, pattern variability, maximum power variability, median frequency, median frequency SD) was tested on all muscles investigated with surface EMG pooled together (left and right SOL, MG, TA, MH, VL, RF, GL), on primary extensor muscles (left and right SOL, MG, VL, RF, GL), and on primary flexor muscles (TA, MH). Additionally, we tested whether the stimulation frequency applied was significantly different between conditions of assisted or independent standing. In particular, paired comparisons between conditions of hips assisted – knees assisted and hips assisted – knees independent (subjects number = 8) were performed by Wilcoxon test. Also, comparisons among standing with hips assisted – knees assisted, hips assisted – knees independent, and hips independent – knees independent (subjects number = 5) were performed by either Repeated Measures Anova (and following multiple comparisons by Bonferroni’s post hoc test) or by Friedman Test (and following multiple comparisons by Dunn’s post hoc test). Finally, when one lower limb (i.e. left side) achieved independent extension while the other lower limb (i.e. right

side) required external assistance, paired comparisons (subjects number = 7) between the assisted and independent side were performed by Wilcoxon test.

C. Results

a. Standing motor patterns with and without scES

Research participants required external assistance for lower limb extension when scES was not provided. Limited EMG activity was generally observed in response to the sit-to-stand transition, and negligible EMG was recorded during assisted standing (Fig 4.2 A).

When scES optimized for standing was applied, little activity and no movement was directly induced in sitting (Fig 4.2 B); On the other hand, without any change in stimulation parameters, sensory information related to the sit-to-stand transition and loading of the legs resulted in the generation of activation patterns with different characteristics. We have consistently observed that standing with independence of hip and knee extension is enabled by overall continuous (i.e. non-rhythmic) EMG activity (Fig 4.2 B). However, continuous EMG patterns can also be insufficient for achieving independent standing (Fig 4.2 C, top). On the other hand, the alternation between EMG bursts and negligible activity in lower limb muscles always resulted in assisted standing (Fig 4.2 C, bottom).

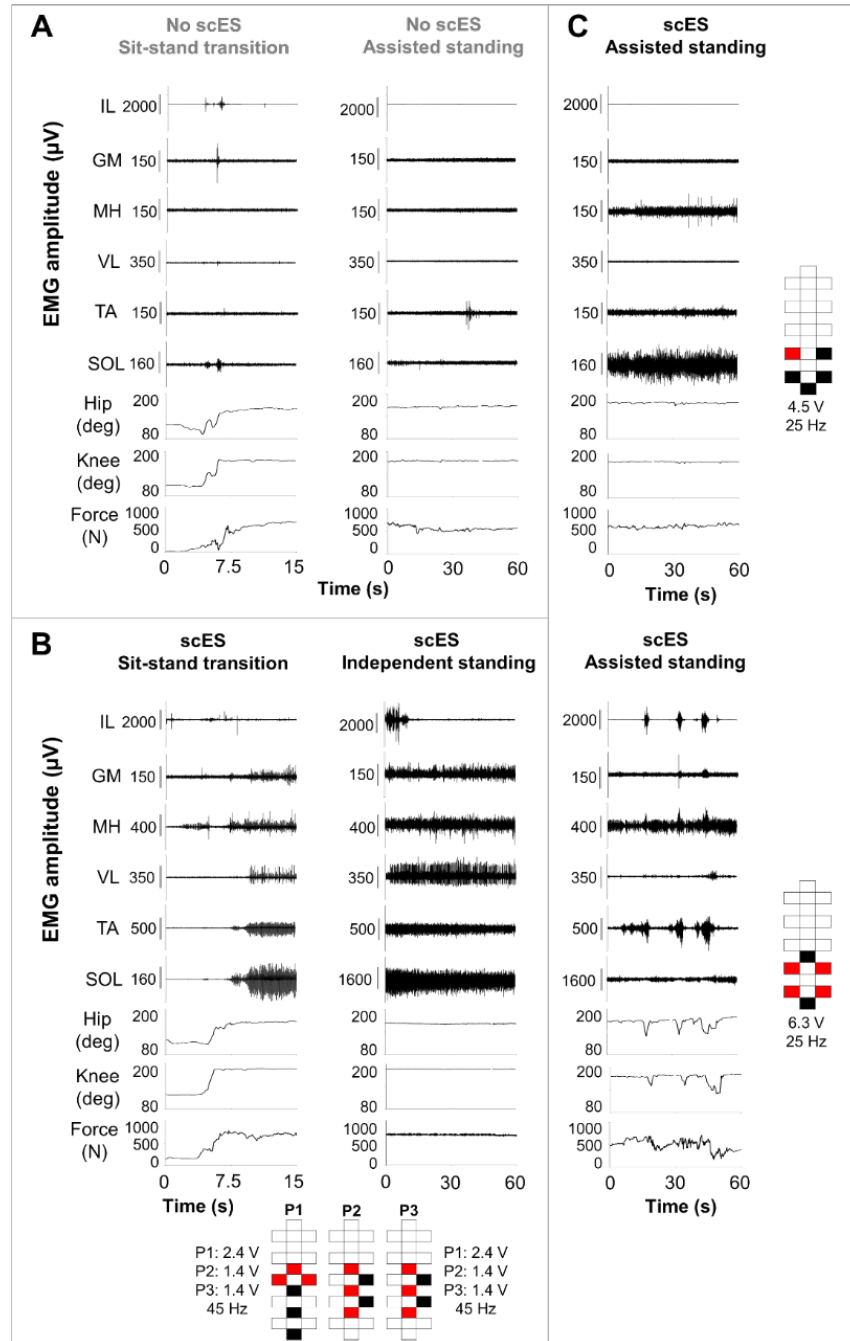


Fig 4.2 Electromyography (EMG), hip and knee joint angle, and ground reaction forces recorded from research participant A59 during: (A) sit-to-stand transition and standing with external assistance for hips and knees extension (assisted standing) without spinal cord epidural stimulation (scES); (B) sit-to-stand transition and independent standing using scES. The participant held the hands of a trainer for balance control; (C) assisted standing with scES resulting from an overall continuous activation pattern (top) and from an EMG pattern characterized by the alternation of EMG bursts and little activation.

Stimulation amplitude, frequency and electrode configuration (cathodes in black, anodes in red, and inactive in white) are reported for each participant. In **B**, the participant was stimulated with 3 programs delivered sequentially at 15 Hz, resulting in an ongoing 45 Hz stimulation frequency. EMG was recorded from the following muscles of the right lower limb: IL, iliopsoas; GL, gluteus maximus; MH, medial hamstring; VL, vastus lateralis; TA, tibialis anterior; SOL, soleus.

b. Time- and frequency-domain EMG features can accurately classify assisted versus independent standing

In order to identify EMG activation characteristics resulting in independent or assisted standing, we initially included two time-domain EMG variables (total power and pattern variability) in the proposed data processing framework aimed at classifying assisted and independent standing. This approach led to classification accuracy equal to 83.7% for assisted and independent standing when all investigated muscles were considered for analysis. To improve this classification accuracy, we explored the inclusion of frequency-domain EMG features in the computational model. An initial step was devoted to the selection of an effective analysis method for EMG activity promoted by scES. When exemplary EMG signals recorded during assisted and independent standing were considered for analysis (Fig 4.3 A), Fast Fourier Transform (FFT) and, to a less extent, Short-Time Fourier Transform (STFT) primarily highlighted the content of frequencies related to epidural stimulation frequency (25 Hz) and its harmonics (Fig 4.3 B). On the other hand, Continuous Wavelet Transform (CWT) showed relevant frequency content that was not related to scES frequency. Also, the power of EMG signal collected during independent standing tended to be shifted toward lower frequency bins compared to that recorded during assisted standing.

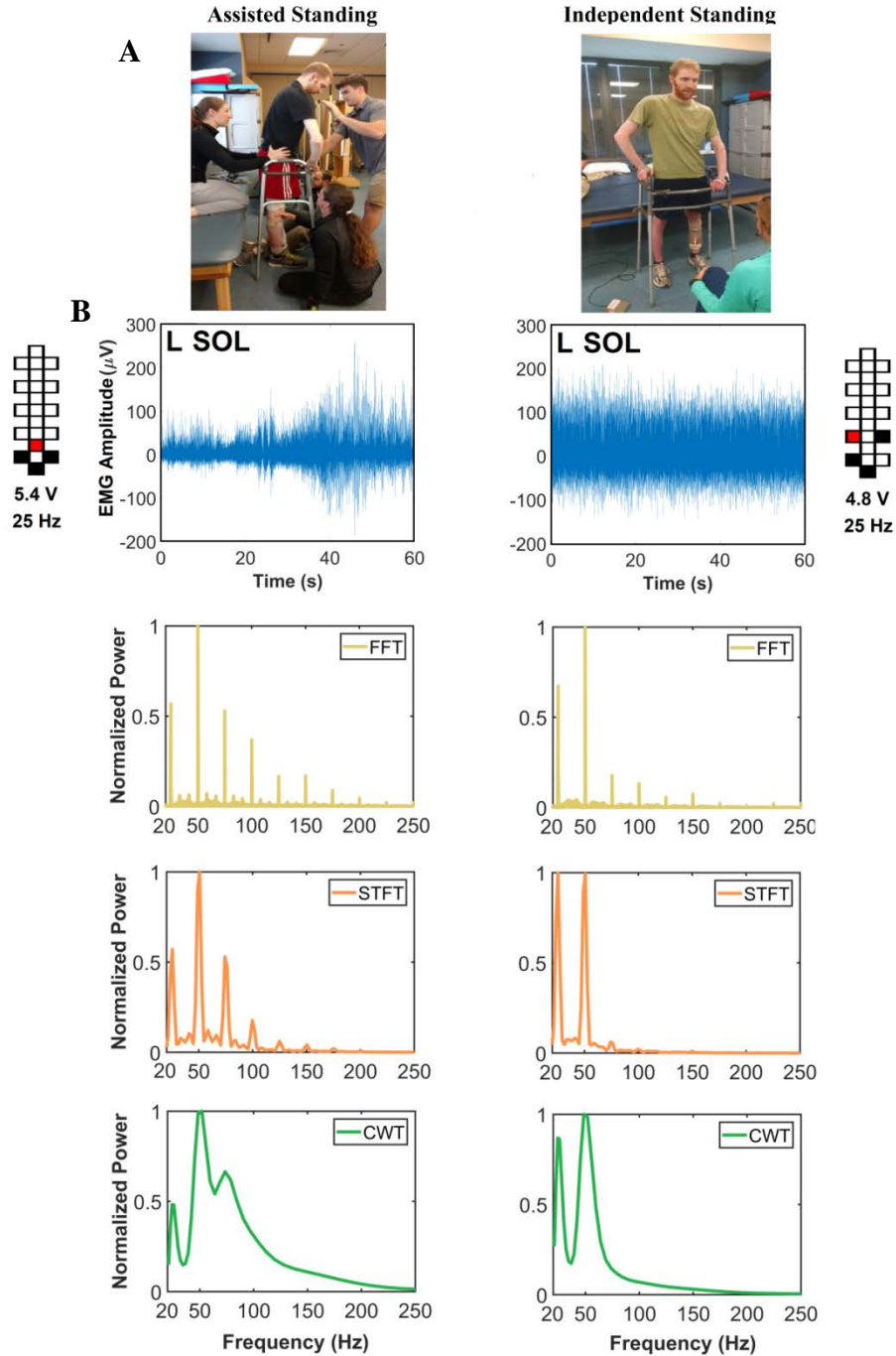


Fig 4.3 (A) Exemplary images of assisted standing (left) and independent standing (right). (B) EMG activity recorded from the left soleus (L SOL) of research participant A45 during assisted standing (left) and independent standing (right) with epidural stimulation, and related spectral power density calculated by Fast Fourier Transform (FFT), Short-Time Fourier Transform (STFT) and Continuous Wavelet Transform

(CWT) are plotted. Stimulation amplitude, frequency and electrode configuration (cathodes in black, anodes in red, and inactive in white) are reported

We then applied these three signal analysis methods on all EMG data collected during assisted and independent standing events from the 11 subjects that were considered in this study.

After normalization, dimension reduction and logarithmically transforming the EMG spectral feature values, the first three dimensions of standing data points (blue: independent standing; red: assisted standing) derived from the tested spectral analysis methods are plotted in Fig 4.4 A. It can be noted that the three analysis methods result in different distribution of the data points, and that CWT tends to present a clearer visual discrimination between assisted and independent standing data points. These feature values were subsequently used as input for KNN classification. As expected from the exemplary data analysis and from the data points presented in Fig 4.4 A, we observed that CWT-derived features promoted the highest classification accuracy for assisted versus independent standing compared to STFT- and particularly FFT-derived features (Fig 4.4 B).

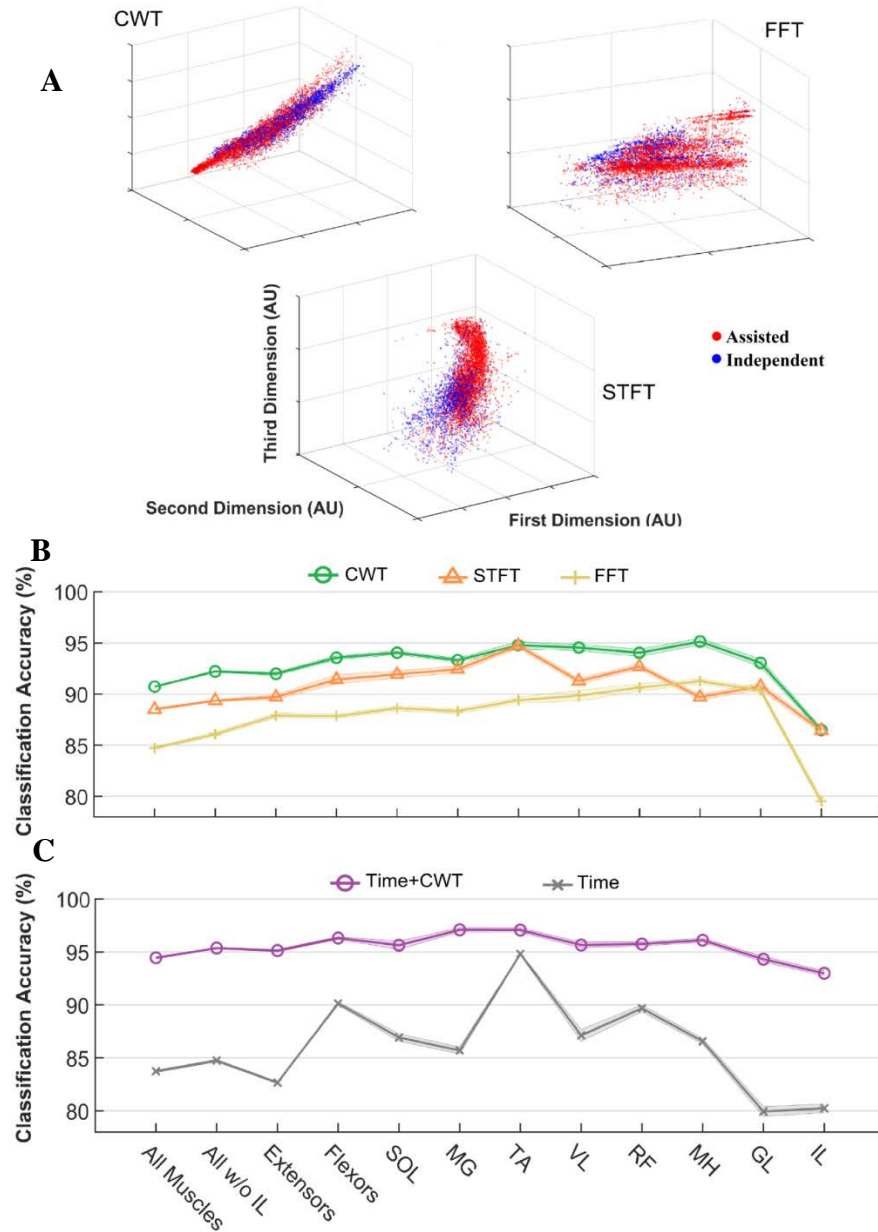


Fig 4.4 (A) The first three dimensions of standing data points (blue: independent standing; red: assisted standing) after normalization, dimension reduction and logarithmically transforming the EMG spectral feature vectors extracted from CWT, STFT and FFT. (B) Classification accuracy for feature vectors extracted from CWT, STFT and FFT and (C) classification accuracy for the combination of time features and CWT-extracted features versus time features only, when considering all muscles, all muscles except IL, flexor muscles, extensor muscles, and each muscle (left and right), separately.

Hence, CWT-derived data were integrated with time-domain EMG features (EMG total power and pattern variability), resulting in a classification accuracy for assisted versus independent standing ranging from 94.4% to 97.1%, depending on the considered muscle(s) (Fig 4.4 C). This classification accuracy is higher and more consistent across examined muscles compared to when either frequency- or particularly time-domain EMG features alone were considered (Fig 4.3 B and C). Based on the results reported in this section, CWT-derived data were also considered for further analysis aimed at describing the physiological characteristics of muscle activation during standing with scES.

c. Physiological characteristics of muscle activation resulting in assisted or independent standing

Higher values of EMG pattern variability can characterize the muscle activation pattern consisting of alternation between EMG bursts and silence periods (Fig 4.5 A and D, pattern variability = 0.68), which results in poor, assisted standing. On the other hand, this feature does not discriminate between overall continuous EMG patterns resulting in assisted standing (Fig 4.5 B and E; pattern variability equal to 0.23) or independent standing (Fig 4.5 C and F; pattern variability equal to 0.22). CWT can provide additional information based on instantaneous EMG time- and frequency-domain features. For example, in case of the alternation between EMG bursts and silence periods, the maximum power variability is also relevant (Fig 4.5 G, EMG maximum power variability = 1.35) compared to the condition of assisted standing with overall continuous EMG pattern (Fig 4.5 I, EMG maximum power variability = 0.35).

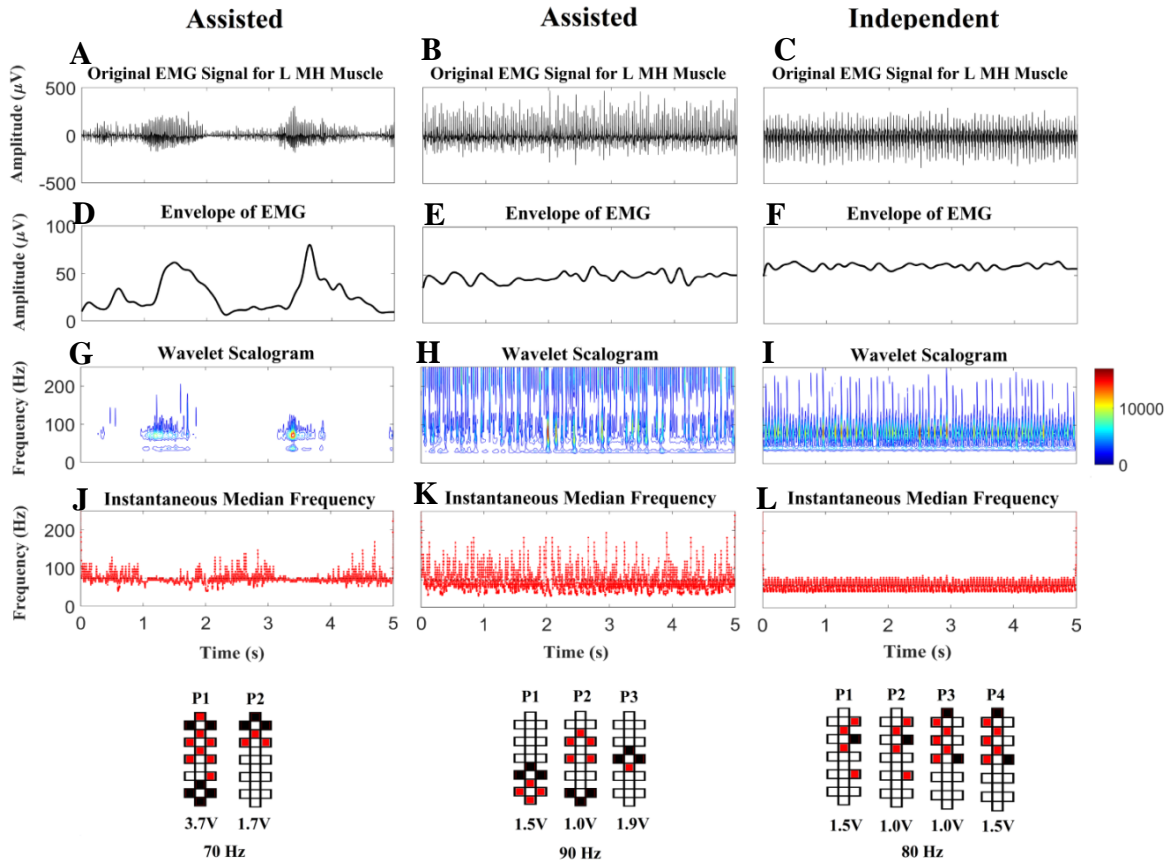


Fig 4.5 (A) EMG signal recorded from left MH muscle during assisted standing with alternating bursting pattern; (B) EMG signal recorded from left MH muscle during assisted standing with continuous pattern; (C) EMG signal recorded from left MH muscle during independent standing with continuous pattern; (D-F) Low frequency envelopes of EMG signals presented in A-B; (G-H) Contour plots of the wavelet scalogram calculated for EMG signals presented in A-B; (J-L) Instantaneous median frequency feature extracted from the scalogram of EMG signals presented in A-B.

Interestingly, differences in the CWT pattern can be observed also between the two similar continuous raw EMG activity recorded from the same individual during assisted and independent standing (Fig 4.5 B and C, respectively). In particular, assisted standing tended to present greater EMG maximum power variability (0.48; Fig 4.5 G), higher median frequency (70 Hz; Fig 4.5 K) and greater variability of median frequency

(median frequency SD = 32 Hz; Fig 4.5 K) compared to EMG activity that resulted in independent standing (0.35, 59 Hz, and 20 Hz, respectively; Fig 4.5 I and L).

Paired statistical comparisons among individuals (n = 8) that achieved both standing with assisted and independent knees extension show that independent knees extension was promoted by significantly higher EMG total power, lower pattern variability, lower maximum power variability, lower median frequency variability, and lower median frequency as compared to assisted standing (Fig 4.6). These differences were more marked when all investigated muscles and primary extensors muscles were considered as compared to primary flexor muscles. It is also worth noting that the average stimulation frequency was similar between the two conditions (51 ± 22 Hz for knees assisted and 55 ± 26 Hz for knees independent; $p = 0.98$).

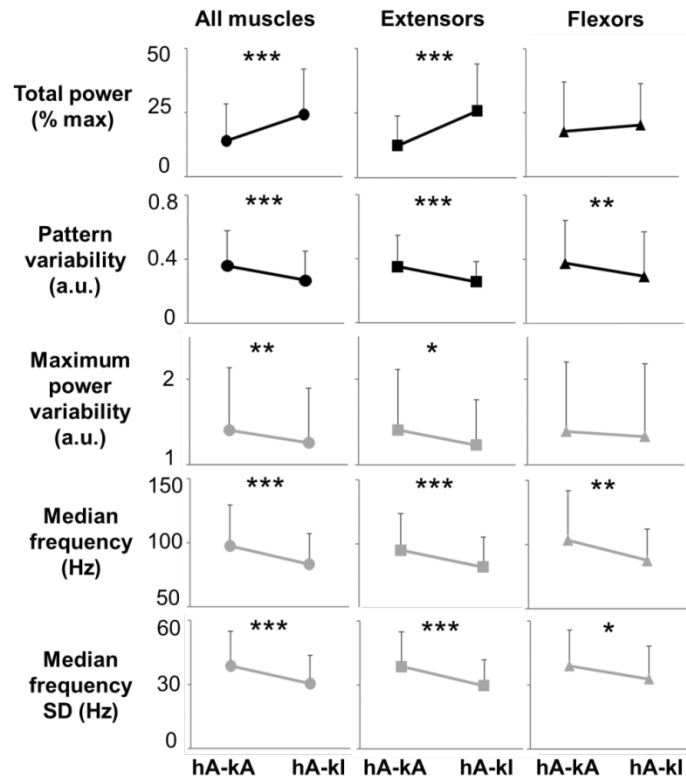


Fig 4.6 Paired statistical comparisons among individuals that achieved both standing with assisted and independent knees extension while their hip was assisted based on extracted total power, pattern variability, maximum power variability, average median frequency and median frequency standard deviation. Hip assisted (hA); knee assisted (kA); knee independent (kI).

We then performed a similar comparison including the 5 individuals who achieved standing with assistance at both hips and knees, with assistance at hips and independent knees extension, and with independent hips and knees extension (Fig 4.7). In summary, no substantial differences were observed between standing conditions of hips assisted – knees independent and hips independent – knees independent. On the other hand, these two standing conditions with independent knees extension were characterized by higher EMG total power, lower pattern variability, lower median frequency variability, and lower median frequency compared to standing with knees assisted, showing the same trend already reported in Fig 5. Also, the stimulation frequency was similar across these three standing conditions (58 ± 24 in hips and knees assisted; 61 ± 29 Hz in hips assisted-knees independent; 62 ± 33 Hz in hips and knees independent; $p = 0.182$).

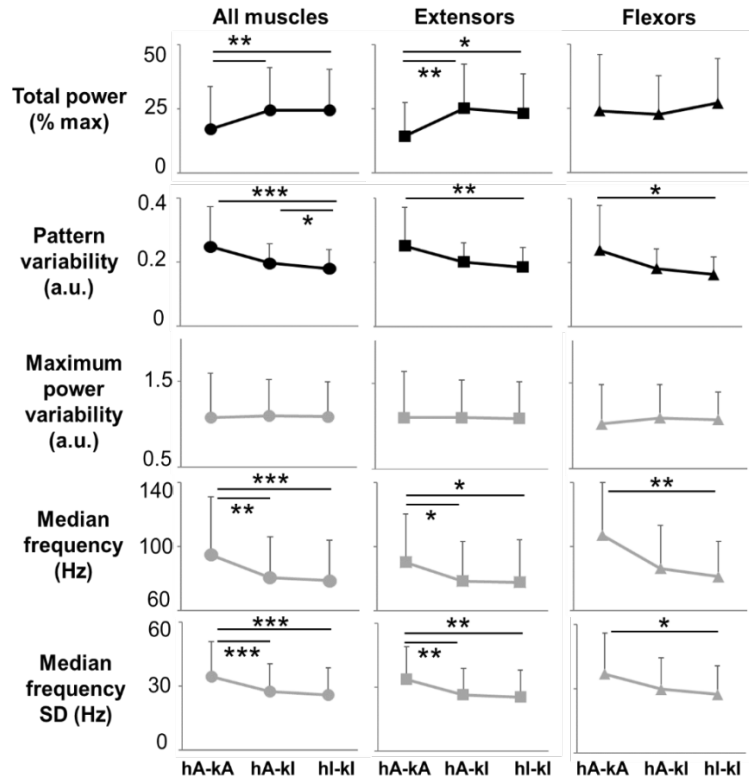


Fig 4.7 Paired statistical comparisons among individuals that achieved standing with assisted and independent knees extension while hip was assisted, and independent hip and knees extension based on extracted total power, pattern variability, maximum power variability, average median frequency and median frequency standard deviation. Hip assisted (hA); hip independent (hI); knee assisted (kA); knee independent (kI).

Also, in standing conditions during which one lower limb (i.e. left side) achieved independent extension while the other lower limb (i.e. right side) required external assistance, higher EMG total power, lower pattern variability, lower maximum power variability, lower median frequency variability, and lower median frequency were also detected from the limb with independent extension (Fig 4.8). This trend showed more consistent statistical significance when all investigated muscles were pooled together for analysis.

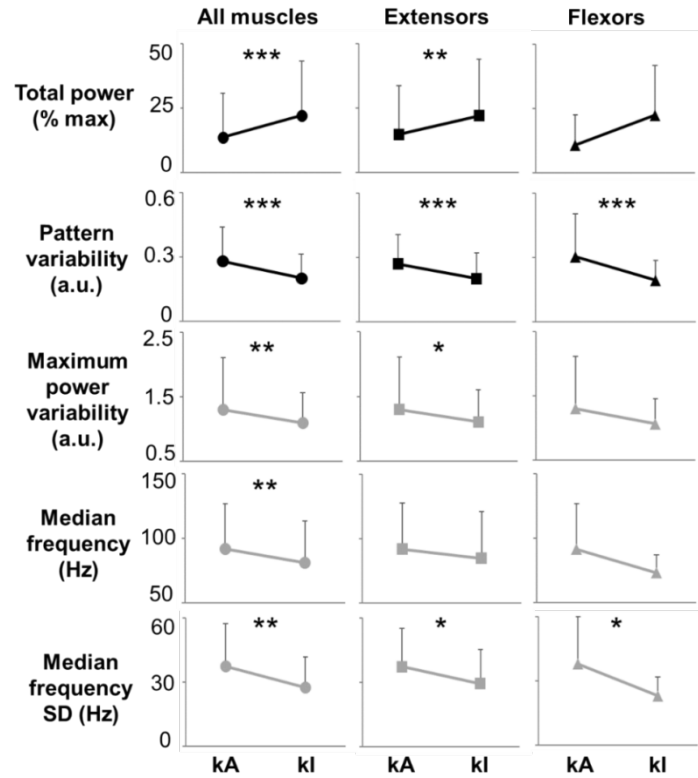


Fig 4.8 Paired statistical comparisons for standing with assisted and independent knees extension based on extracted total power, pattern variability, maximum power variability, average median frequency and median frequency standard deviation. Knee assisted (kA); knee independent (kI).

It is worth noting that the higher median frequency and median frequency SD values observed during assisted standing can be attributed, at least partially, to the sharper peak shape of spinal cord evoked responses (Fig 4.9, dark red arrows), which results in relevant increments of the instantaneous median frequency. Conversely, the smoother peaks of spinal cord evoked responses detected during independent standing contain more power at lower frequencies and result in a smaller instantaneous median frequency modulation.

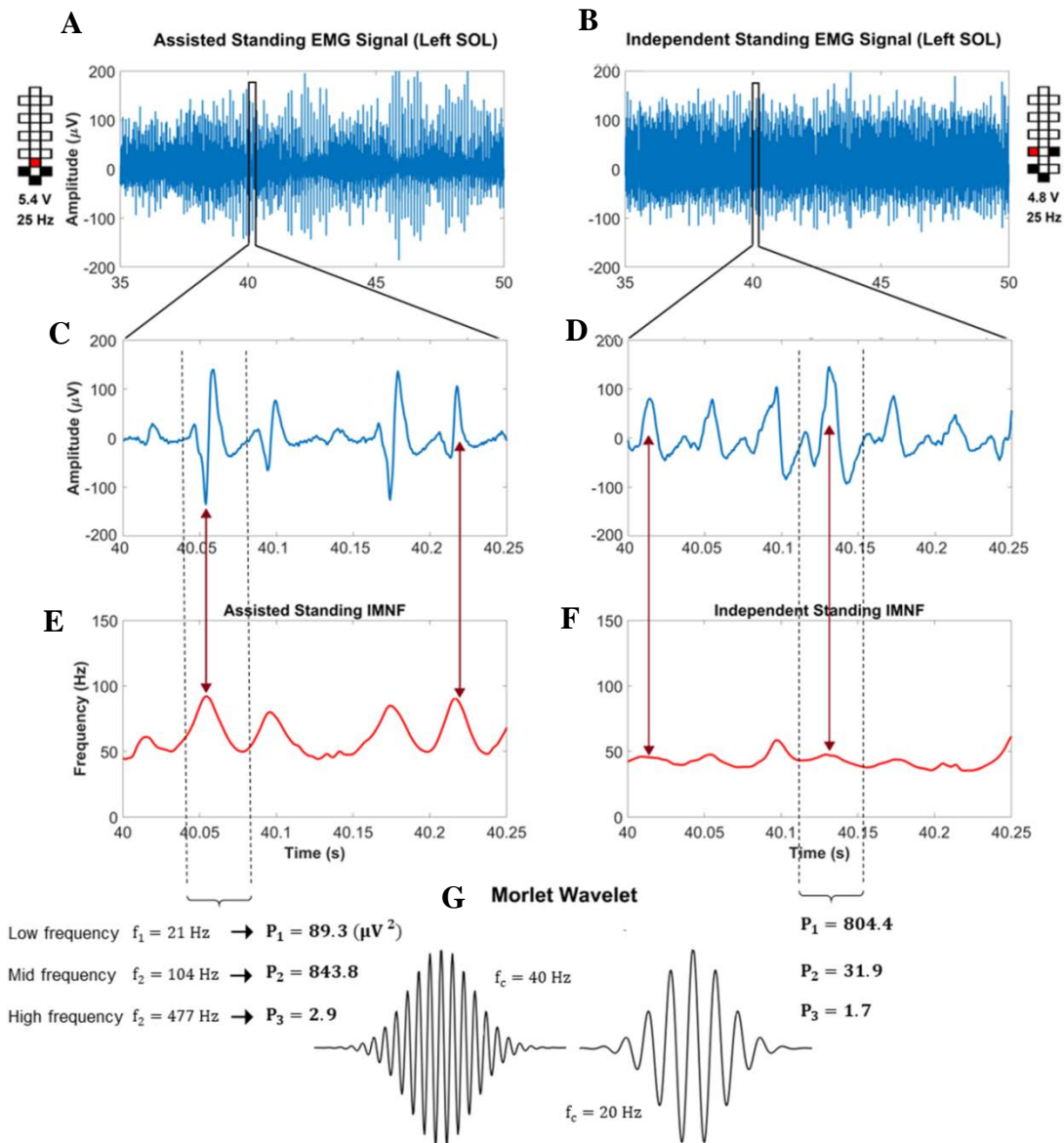


Fig 4.9 Recorded EMG signals from left SOL during assisted (A) and independent (B) standing conditions, their 25 milliseconds zoomed-in view (C and D) and the corresponding instantaneous median frequency values (E and F). (G) Exemplary Morlet wavelet signals with high (40 Hz) and low (20 Hz) central frequencies (f_c).

d. Ranking the effectiveness of EMG activity for standing

The high classification accuracy for assisted versus independent standing provided by our framework (Fig 4.4 C) led us to develop a further computational step aimed at ranking the effectiveness of muscle activation patterns generated during

standing. We initially trained muscle-specific KNN models based on assisted and independent standing data set (Fig 4.10). We then fed the prediction algorithm with a total of 48 standing events performed by 6 individuals while different stimulation parameters were tested to search for optimal stand-scES parameters (Fig 4.10). The prediction algorithm correctly labeled as “assisted” (i.e. score between 0 and 0.5) most of the standing events (95.8%). More importantly, its ranking scores varied substantially among stimulation parameters applied and investigated muscles.

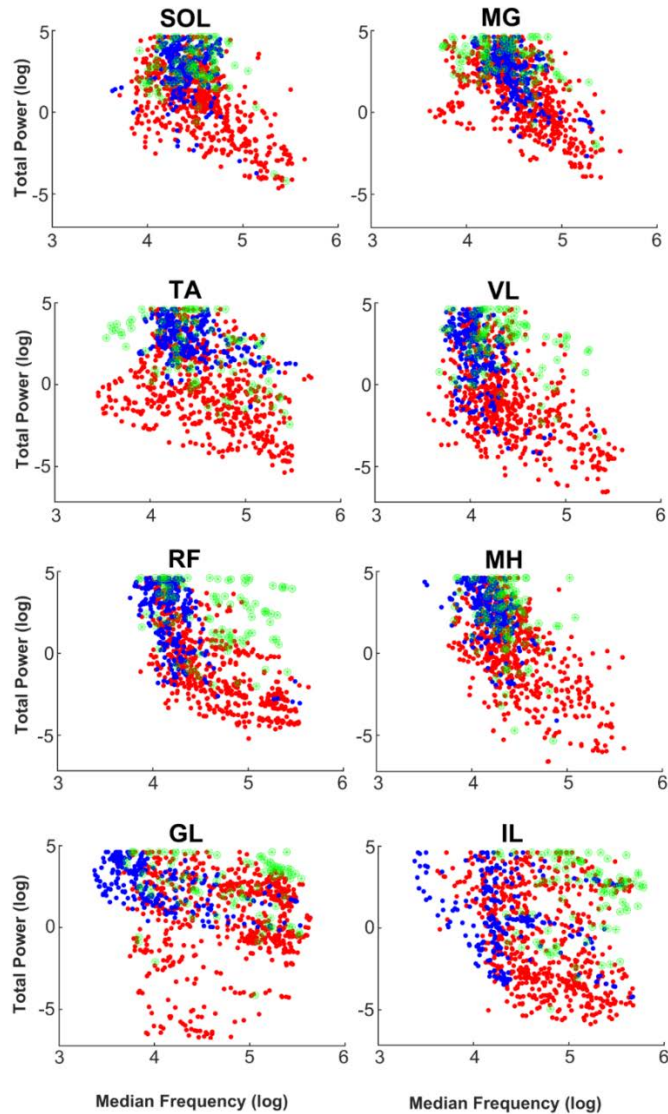


Fig 4.10 Two representative features (total power and median frequency) of the EMG data sets used to train assisted (red) and independent (blue) standing KNN models are plotted against each other for each investigated muscle. Trends of assisted and independent standing data points are overall similar across muscles, while the distribution pattern shows some inter-muscle variability (i.e. between SOL and TA). EMG data collected from 6 individuals during a total of 48 standing events aimed at testing the effectiveness of different stimulation parameters (green stars) were then fed to the prediction algorithm. While all these attempts resulted in assisted standing, the related EMG data points are spread across the plots, with some of them partially overlapping independent standing data points.

For example, participant A68 tested 9 different scES parameters during the monitored standing session, obtaining average prediction scores ranging between 0.14 and 0.49 (Fig 4.11 A). In particular, during the standing attempt characterized by the lower score, only R IL and TA muscles showed EMG activity characteristics closer to independent standing. On the other hand, the standing attempt with the higher score was characterized by independent standing-like EMG characteristics of several muscles (i.e. posterior thigh muscles and anterior muscles of the left lower limb). Also, EMG activity score of bilateral plantar flexor muscles was low in both standing conditions.

We then exemplified that the proposed prediction algorithm may be used also for ranking EMG activity collected during standing with different levels of assistance. For instance, it correctly labeled two events as “independent”, and suggested that independent standing can be achieved even when activation characteristics of few muscles are ranked as “assisted” (Fig 4.11 B). Also, when the algorithm is trained with the proper data set, it can rank the effectiveness of EMG activity generated by the lower limb assisted for knee extension (i.e. right side) while the other leg maintained independent extension (left side) (Fig 4.11 C).

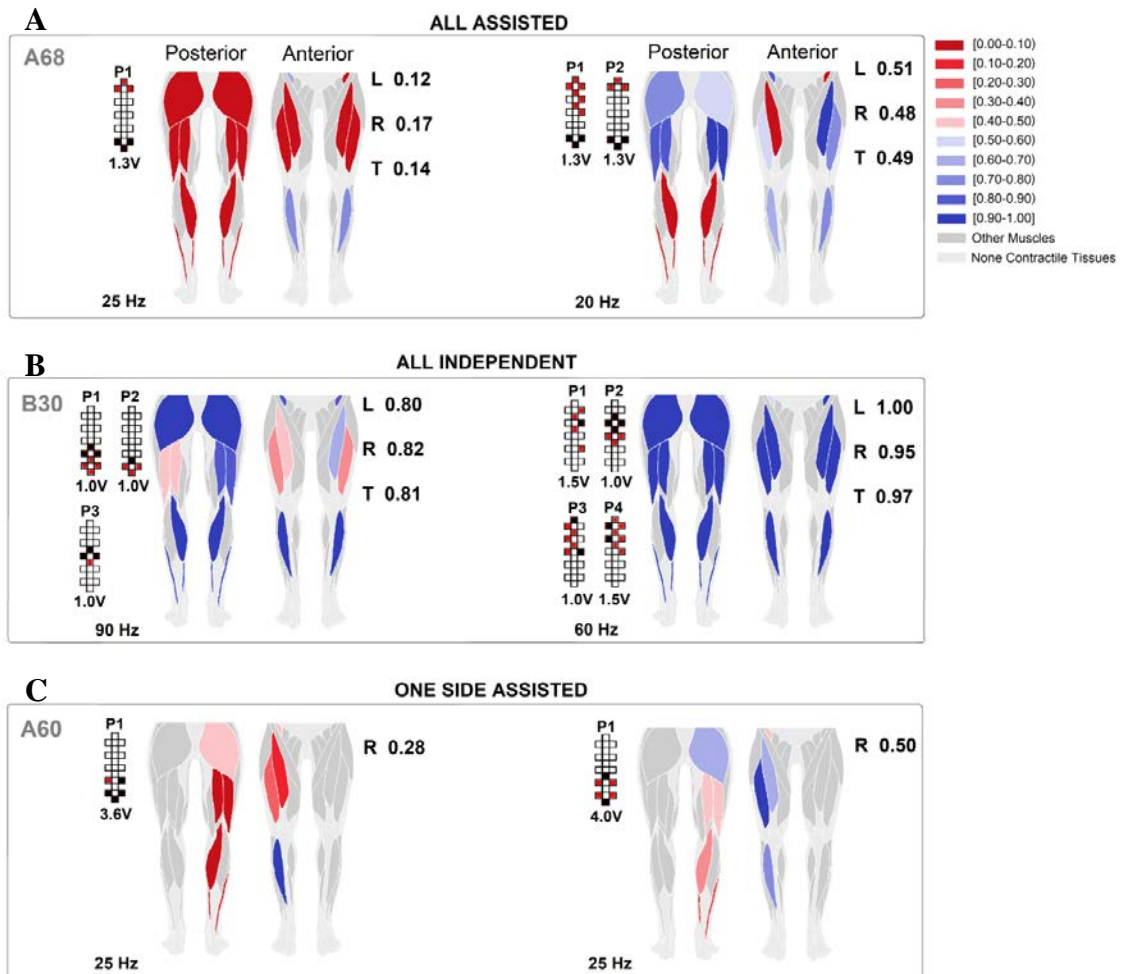


Fig 4.11 Ranking of individual muscle performances presented as colormaps (shades of red related to assisted standing and shades of blue related to independent standing). (A) Examples of two assisted standing events from subject A68 with 0.14 total prediction score (left) and 0.48 total prediction score (right). (B) Examples of two independent standing events from subject B30 with 0.81 total prediction score (left) and 0.97 total prediction score (right). (C) Examples of two partially assisted (one knee assisted and one knee independent) standing events from subject A60 with 0.28 total prediction score (left) and 0.50 total prediction score (right).

D. Discussion

In this study, we developed a novel data processing framework for EMG activity promoted by spinal epidural stimulation during standing in individuals with severe SCI. This approach allowed us to uncover the physiological characteristics of neuromuscular activation resulting in independent standing. Additionally, we showed that, for each investigated muscle, the proposed machine learning algorithm can rank the effectiveness of EMG activity generated during standing. We discuss the implications of these findings in the context of mechanisms of motor pattern generation, and for the contribution this framework can provide during the selection of scES parameters, suggesting that it can facilitate the clinical translation of scES for standing motor rehabilitation.

Frequency-domain EMG features have been widely considered to study central motor control strategies during voluntary muscle activation [130-133], and the more recent development of technology for decomposing surface EMG signals has resulted in further insights on this topic [134-136]. On the other hand, EMG spectral features have been substantially neglected when the generation of activation patterns is promoted by scES. Gerasimenko and colleagues proposed a qualitative interpretation of spectral analysis (by FFT) performed on EMG signals collected from flexor and extensor muscles during stepping with scES [137]. In particular, they suggested that the dominant spectral peaks related to the stimulation frequency and its harmonics observed during the extension phase in extensor muscles reflected a predominance of monosynaptic-evoked responses. Conversely, the lack of consistent dominant peaks detected from the tibialis anterior during the flexion phase of the gait cycle was interpreted as a predominance of polysynaptic-evoked responses. It is plausible that the marked dominant FFT spectral peaks related to the epidural stimulation frequency (i.e. Fig 4.3 A; Gerasimenko et al.

[137]) have been often interpreted as features without relevant physiological meaning, thus discouraging further efforts aimed at quantifying scES-promoted EMG spectral parameters. Our approach was initially focused on understanding which spectral analysis method is more effective for identifying frequency-domain EMG features that characterize standing promoted by scES. This is important because, for example, FFT presents some intrinsic limitations such as poor time resolution, assuming the stationarity of EMG signal, and being unable to localize frequency content of the signal in the time domain, which may result in insufficient representation of the frequency content of scES-promoted muscle activation. Our results suggest that CWT is a spectral analysis method that can provide relevant frequency content not related to scES frequency (Fig 4.3) as well as features resulting in the most accurate classification of assisted and independent standing (Fig 4.4). This may be due to its high time and frequency resolution by decomposing the signal using numerous multi-resolution wavelets [47, 48], which leads to an accurate characterization of the short time component within non-stationary signals [49]. Conversely, the resolution of STFT in time and frequency domain depends on the selected window size: longer window size increases the frequency resolution but impairs time resolution, which is not ideal for non-stationary signals like EMG [138].

To date, little is known about the characteristics of scES-promoted muscle activation resulting in the recovery of independent standing with self-assistance for balance after clinically motor complete SCI. We previously observed that the alternation between EMG bursts and little EMG activity (i.e. Fig 4.2 C, bottom) results in poor standing pattern and the need of external assistance [11]. Conversely, the overall continuous (i.e. non-rhythmic) co-activation of several lower limb muscles was

demonstrated when motor complete SCI individuals were able to maintain independent lower limb extension using spinal cord stimulation [11, 12, 116, 139, 140]. In this study, we identified additional EMG features that can discriminate the effectiveness of EMG activity for standing beyond the mere variability of the EMG pattern over time. In particular, independent standing events were promoted by EMG activity characterized by lower median frequency, lower variability of median frequency, lower variability of instantaneous maximum power as well as higher total power as compared to assisted standing (Figs 4.6-4.8). It is worth noting that the frequency-domain features can differentiate assisted and independent standing also when the raw EMG signals are both overall continuous and demonstrate similar amplitude (Figs 4.5 and 4.9). We then examined the evoked responses generated during standing (Fig 4.9), and observed that the higher median frequency and higher variability of median frequency detected during assisted standing reflect, at least partially, the sharper peaks of evoked responses, which carry more power at higher frequencies. On the other hand, the smoother peaks of evoked responses detected during independent standing do not induce relevant increments in instantaneous median frequency. Partial desynchronization of motor units and/or greater involvement of polysynaptic responses, among others, may explain the smoother peaks of evoked responses detected during independent standing. Further studies involving the application of multi-channel surface EMG and dedicated signal processing may be useful for assessing the concurrent activity of many different motor units and investigating their firing pattern [141].

Presently, the prevailing view is that scES facilitates motor pattern generation by recruiting primarily large myelinated fibers associated with somatosensory information,

and particularly with proprioceptive and cutaneous feedback circuits, at their entry into the spinal cord as well as along the longitudinal portions of the fiber trajectories, altering the excitability of lumbosacral spinal circuits [9, 142-150]. It is also important to consider that stimulation parameters play a crucial role in determining extent and proportion of the modulation of sensory-motor pathways impacted by scES [151]. For example, it is suggested that different stimulation frequencies may access different inhibitory and/or excitatory pathways within spinal circuitry [152], and that higher stimulation frequencies may promote a progressive integration of additional afferent inputs through the greater involvement of interneurons [116, 153, 154]. Hence, an effort was devoted to understand whether the differences in EMG features observed in the present study between assisted and independent standing, and particularly the frequency-domain features, were associated with the application of different scES frequencies. Interestingly, the average stimulation frequencies delivered during assisted and independent standing were very similar (see description of Fig 4.6). Moreover, consistent differences in EMG features were also observed between the one lower limb achieving independent extension and the contralateral lower limb requiring external assistance, while the same stimulation parameters were applied (Fig 4.8). Taken together, these findings suggest that the characteristics of EMG activity result from the complex interaction among the stimulation parameters applied, the characteristics of spinal circuitry, which undergoes extensive individual-specific reorganization after severe SCI [155, 156], the somatosensory information as well as residual supraspinal influence [8, 157].

The integration of novel CWT-derived features with EMG total power and pattern variability enabled the machine learning (KNN) algorithm to accurately classify assisted

versus independent standing (Fig 4.4). We took advantage of this high classification accuracy to develop a prediction algorithm capable of ranking the activation of the investigated muscles for standing (Fig 4.11). This approach results in a real-time feedback on the effectiveness of scES-promoted muscle activation for standing, which can support researchers and clinicians during the process of selection of stimulation parameters. For example, the data reported in Fig 4.11 A suggests that left and right plantar flexors presented poor activation with both sets of stimulation parameters, being one of the possible factors limiting the achievement of independent standing (Fig 4.11 A, right). While the present framework does not propose the specific stimulation parameters adjustment for optimizing muscle activation, it can substantially improve the application of the guidelines previously developed for adjusting scES for standing [116]. For instance, information on the individualized map of motor pools activation [158, 159] may be retrieved and used to determine the electrode field of an additional interleaving program aimed at targeting primarily the location of the spinal circuitry related to plantar flexors. Then, a much smaller cohort of cathode-anode combinations as well as amplitude and frequency settings can be tested, thus increasing the likelihood of achieving an improved activation pattern in a reduced amount of time. The second important contribution of the proposed framework is that it can identify which of the tested set of stimulation parameters promotes the activation pattern more effective for standing. This can be of particular interest when different sets of parameters result in the same level of external assistance (i.e. total score of Fig 4.11 A and C), and the decision on which parameters would be applied for stand training needs to be made.

E. Study Outcomes

The preliminary results of this study have been published as a full research paper in 2018 IEEE International Symposium on Signal Processing and Information Technology (ISSPIT). The journal manuscript of the complete framework and findings is submitted to Nature Communication journal and is under review for publication. The results of this study have also been presented as oral and poster presentations in 2018 ISSPIT and 2018 BMES conferences, respectively.

CHAPTER V

CONCLUSIONS AND FUTURE DIRECTIONS

In this chapter, the summary and conclusion of the research that has been presented in this dissertation in the areas of signal and image processing, machine learning and deep learning, and their applications in spinal cord injury (SCI) research will be presented. The future directions for expanding the current work will be proposed in the last section.

A. Conclusion

In this dissertation, we have developed several engineering tools and offered neurotechnological advancements to address issues that researchers, clinicians and patients are facing in various aspects of spinal cord injury (SCI) research.

In the first part of this research, the automatic framework for segmentation of muscle groups and adipose tissue of MRI thigh volumes is proposed to quantify the effects of SCI on skeletal muscle atrophy and adipose tissue infiltration that can result in compromised muscle mechanical output and lead to health-related complications. This framework can measure the effectiveness of training interventions to stop or reverse this process. The novel automatic approach segments the thigh volumes of subcutaneous adipose tissue, inter-muscular adipose tissue and muscle tissue using an intensity-based algorithm. Also, three muscle groups can be segmented utilizing proposed Joint Markov Gibbs Random Field model that integrates first order appearance, spatial information, and

shape model to localize the muscle groups. The accuracy of the automatic segmentation method was tested both on SCI (N=16) and on non-disabled (N=14) individuals, showing an overall $92.35 \pm 6.99\%$ accuracy for adipose tissue and $90.79 \pm 5.32\%$ for muscle compartments segmentation based on Dice Similarity Coefficient. The proposed framework showed an overall higher accuracy than ANTS and STAPLE, two validated atlas-based segmentation methods and multi-modal 3-D CNN-based segmentation method. The comparison with CNN shows that the stochastic methods are still powerful tools for segmenting medical images and their accuracy are comparable to those obtained by deep learning structures while their processing time is far less than CNN. The proposed method can provide fast and accurate quantification of adipose and muscle tissues that have important health and functional implications in the SCI population, thus facilitating the use of MRI to assess individual characteristics and possibly the effects of different interventions. Our results have shown that the proposed automatic framework shows very similar characteristics and trends to those obtained by manual segmentation (ground truth) in 30 individuals and therefore, it is a reliable method that substantially reduces labor work and processing time.

In the second part of this dissertation, we have developed a novel EMG-based framework for de-noising, activation detection, feature extraction and visualization of the motor evoked potentials during the mapping process of the epidural stimulation in order to facilitate the identification of the appropriate stimulation parameters (intensity, frequency and anode/cathode assignment). The purpose of this work was to develop a novel approach to automatically detect the occurrence of evoked potentials, quantify the attributes of the signal and visualize the effects across a high number of scES parameters.

Using this framework, raw EMG signals are successfully converted into two/three dimensional images and de-noised using GGMRF image smoothing technique. Additionally, the occurrence of scES induced muscle activation is automatically detected along with the ability to extract key features in the EMG signal and generate the visual output for user interpretation. Each of these five novel algorithms has several advantages over conventional methodologies, which make them indispensable for the data analysis application. For instance, the first algorithm converts the signal into an image, which enables clear illustration of the latencies for all activations as well as the overall onset of the scES induced motor responses. By converting the raw signal into image, this algorithm also prepares the data for the next step that is GGMRF image smoothing method to get a de-noised signal without affecting the shape and latency of muscle activations. As it is shown in the results adding the GGMRF method to the framework is also noticeably advantageous for the performance of the activation detection step. In the activation detection algorithm, we developed a statistically optimal decision method by applying MLE together with comparing the probability density functions of the muscle activations to the background noise utilizing LLR and calculating the dynamic activation threshold. In comparing the automatic method for activation threshold detection vs. manual detection (ground truth) on 700 EMG signals, the new automated approach developed here demonstrated average accuracy of 98.28% based on the errors of combined false positive and false negative data. Finally, the combination of the modified AGLR method and GGMRF has proven to have minimum sensitivity to the changes in the signal to noise ratio compared to the other well-known EMG onset detection methods i.e. AGLR method without smoothing and TKEO method using both simulated EMG

signal and real EMG signals. Comparing the three methods on the recorded EMG signals indicates the robustness in the accuracy of the presented activation method in the situation where no information about the noise level in the signal is known. In addition, the feature extraction and visualization steps of the framework help us to make accurate and quick connections between the desired EMG features and the scES parameters like intensity, electrode configuration and frequency. In conclusion, this study clearly demonstrates the advantages of implementing a set of algorithms for improving the accuracy and speed in complex EMG data analysis.

In the last part of this research, we introduced an EMG time-frequency analysis framework that implements EMG spectral analysis and machine learning tools to characterize EMG patterns resulting in independent or assisted standing enabled by spinal cord epidural stimulation. In this framework, the EMG signals that are recorded during standing task with spinal cord epidural stimulation in individuals with motor complete spinal cord injury were used to examine whether the spectral content of the EMG activity reveal beneficial information about the quality of the standing performance. We compared the classification performance of the three spectral transforms: FFT, STFT and CWT to find which method provides more information regarding the standing conditions. The results of this work have shown that CWT represents more in-depth details about the frequency content of the EMG signals recorded during standing with spinal cord epidural stimulation compared to FFT and STFT in SCI population. The classification step shows that these extra details provided by CWT helps to classify the data based on the quality of standing with higher accuracy than STFT and FFT or the time-domain features alone. The steps that were taken prior to classification including normalization of the extracted

features, dimension reduction, and particularly the logarithmic transform step, are crucial in the classification process to present the advantages of CWT over other methods. Finally, we have only extracted physiologically relevant features from the EMG spectral because these features can be helpful in gaining insights about the neurophysiological differences between different standing conditions which are also related to the stimulation parameter selection. The signal processing framework that is presented in this study can be helpful in facilitating the efforts of adjusting the stimulation parameters to achieve independent standing in individuals with severe SCI. In conclusion, we have demonstrated that the proposed data analysis framework can characterize time- and frequency-domain EMG features resulting in the recovery of independent standing with self-assistance for balance in individuals with motor complete SCI using spinal cord epidural stimulation. This allowed us to develop a machine learning algorithm capable of ranking the effectiveness of muscle-specific activation for standing, which can significantly facilitate the process of selection of stimulation parameters for standing motor rehabilitation. Future studies should be aimed at investigating the effects of stimulation parameters modulation on the EMG features related to standing ability. Also, the application of a similar framework on EMG activity collected during stepping with epidural stimulation may provide novel insights on mechanisms of motor pattern generation and selection of epidural stimulation parameters.

It is also important to note that the engineering advancements proposed in this dissertation have greatly benefited SCI research by accelerating the efforts to quantify the effects of SCI on muscle size and functionality, expanding the knowledge regarding the neurophysiological mechanisms involved in re-enabling motor function with epidural

stimulation, fast-tracking the selection of optimum stimulation parameters for performing motor tasks and consequently considerably reducing costs and labor work while helping the patients with complete paralysis to achieve faster motor recovery.

B. Future Directions

The proposed frameworks that have been presented in image and signal processing fields for assessing anatomy and functional aspects of human skeletal muscles after SCI can be improved and expanded further as following:

- For the MRI image segmentation framework, in addition to segmenting relevant muscle groups, we can attempt to segment each muscle volume individually by attaining the recorded MRI slices with higher resolution than 1.5 mm in order to capture individual muscle borders, and improve the accuracy of the segmentation method by using convolutional networks. We can also expand the segmentation from 50 central slices to the whole thigh (approximately 300 slices) by manually segmenting once every six slices (total of 50 slices) and use the cylindrical shape information of the thigh muscles to predict the shape of the middle slices.
- For the EMG signal processing framework in the time domain, we can automate the process of epidural stimulation parameter selection by applying proper predictive models to answer questions such as:
 - Which stimulation parameters would selectively target desired muscles without activating their antagonist muscles?
 - Which parameter selections cause symmetric or asymmetric outputs on left and right leg muscles?

- Which parameter selections cause consistently higher/lower/faster/slower response in certain muscles?
- Which parameter selections cause no activations in the muscles and keep the blood pressure at normal range?
- Which parameter selections are less variable over time during training sessions?
- For the EMG signal processing in time-frequency domain, we can take advantage of deep neural networks for finding the underlying patterns in the data and classifying the EMG signals based on the quality of motor performance.
- In addition to analyze each muscle response separately, we can find the mutual activation patterns between muscle pairs in order to assess synergistic patterns in muscle activations. To achieve this goal, the coherence of paired EMG signals can be calculated in the frequency domain and using dimension reduction approaches such as non-negative matrix factorization or deep auto encoder networks the most prominent frequency bands for paired muscle responses can be found.

REFERENCES

1. Armour, B.S., et al., *Prevalence and Causes of Paralysis-United States, 2013*. Am J Public Health, 2016. **106**(10): p. 1855-7.
2. NSCIS, *SCI Facts and Figures at a Glance*. 2018: Birmingham, Alabama.
3. Sezer, N., S. Akkus, and F.G. Ugurlu, *Chronic complications of spinal cord injury*. World J Orthop, 2015. **6**(1): p. 24-33.
4. Giangregorio, L. and N. McCartney, *Bone loss and muscle atrophy in spinal cord injury: epidemiology, fracture prediction, and rehabilitation strategies*. J Spinal Cord Med, 2006. **29**(5): p. 489-500.
5. Cragg, J.J., et al., *Spinal cord injury and type 2 diabetes: results from a population health survey*. Neurology, 2013. **81**(21): p. 1864-8.
6. Rejc, E., C. Angeli, and S. Harkema, *Effects of Lumbosacral Spinal Cord Epidural Stimulation for Standing after Chronic Complete Paralysis in Humans*. PLoS One, 2015. **10**: p. e0133998.
7. Rejc Enrico, A.C.A., Bryant Nicole, and Harkema Susan J., *Effects of Stand and Step Training with Epidural Stimulation on Motor Function for Standing in Chronic Complete Paraplegics*. Journal of Neurotrauma, 2016. **34**(9).
8. Angeli, C.A., et al., *Recovery of Over-Ground Walking after Chronic Motor Complete Spinal Cord Injury*. N Engl J Med, 2018.
9. Angeli, C.A., et al., *Altering spinal cord excitability enables voluntary movements after chronic complete paralysis in humans*. Brain, 2014. **137**(Pt 5): p. 1394-1409.
10. Harkema, S., et al., *Effect of epidural stimulation of the lumbosacral spinal cord on voluntary movement, standing, and assisted stepping after motor complete paraplegia: a case study*. Lancet, 2011. **377**(9781): p. 1938-47.
11. Rejc, E., et al., *Effects of Stand and Step Training with Epidural Stimulation on Motor Function for Standing in Chronic Complete Paraplegics*. J Neurotrauma, 2017. **34**(9): p. 1787-1802.
12. Gill, M.L., et al., *Neuromodulation of lumbosacral spinal networks enables independent stepping after complete paraplegia*. Nat Med, 2018.

13. Harkema, S., et al., *Effect of Epidural stimulation of the lumbosacral spinal cord on voluntary movement, standing, and assisted stepping after motor complete paraplegia: a case study*. Lancet, 2011. **377**: p. 1938-1974.
14. Angeli, C., et al., *Altering spinal cord excitability enables voluntary movements after chronic complete paralysis in humans*. Brain, 2014. **137**: p. 1394-409.
15. Kim, T.Y., J. Son, and K.G. Kim, *The recent progress in quantitative medical image analysis for computer aided diagnosis systems*. Healthc Inform Res, 2011. **17**(3): p. 143-9.
16. Urricelqui, L., A. Malanda, and A. Villanueva, *Automatic segmentation of thigh magnetic resonance images*. International Journal of Medical, Health, Biomedical, Bioengineering and Pharmaceutical Engineering, 2009. **3**(10): p. 314-320.
17. Canny, J., *A computational approach to edge detection*. IEEE Trans Pattern Anal Mach Intell, 1986. **8**(6): p. 679-98.
18. Lin, G.C., et al., *Multispectral MR images segmentation based on fuzzy knowledge and modified seeded region growing*. Magn Reson Imaging, 2012. **30**(2): p. 230-46.
19. Ng, H.P., et al. *Medical Image Segmentation Using K-Means Clustering and Improved Watershed Algorithm*. in *2006 IEEE Southwest Symposium on Image Analysis and Interpretation*. 2006.
20. Pohle, R. and K.D. Toennies, *Segmentation of medical images using adaptive region growing*. Medical Imaging 2001. Vol. 4322. 2001: SPIE.
21. Cootes, T.F., G.J. Edwards, and C.J. Taylor, *Active Appearance Models* %J *IEEE Trans. Pattern Anal. Mach. Intell.* 2001. **23**(6): p. 681-685.
22. Song, W., Z. Weiyu, and L. Zhi-Pei. *Shape deformation: SVM regression and application to medical image segmentation*. in *Proceedings Eighth IEEE International Conference on Computer Vision. ICCV 2001*. 2001.
23. Alirezaie, J., E. Jernigan, and C. Nahmias, *Neural network-based segmentation of magnetic resonance images of the brain*. Vol. 3. 1997. 194-198.
24. Mohamed, N.A., M.N. Ahmed, and A. Farag. *Modified fuzzy c-mean in medical image segmentation*. in *Proceedings of the 20th Annual International Conference of the IEEE Engineering in Medicine and Biology Society. Vol.20 Biomedical Engineering Towards the Year 2000 and Beyond (Cat. No.98CH36286)*. 1998.
25. Koon-Pong, W., et al., *Segmentation of dynamic PET images using cluster analysis*. IEEE Transactions on Nuclear Science, 2002. **49**(1): p. 200-207.

26. Kuo-Sheng, C., L. Jzau-Sheng, and M. Chi-Wu, *The application of competitive Hopfield neural network to medical image segmentation*. IEEE Transactions on Medical Imaging, 1996. **15**(4): p. 560-567.
27. Maksimovic, R., S. Stankovic, and D. Milovanovic, *Computed tomography image analyzer: 3D reconstruction and segmentation applying active contour models--'snakes'*. Int J Med Inform, 2000. **58-59**: p. 29-37.
28. Cohen, L.D., *On active contour models and balloons*. CVGIP: Image Understanding, 1991. **53**(2): p. 211-218.
29. Chenyang, X. and J.L. Prince, *Snakes, shapes, and gradient vector flow*. IEEE Transactions on Image Processing, 1998. **7**(3): p. 359-369.
30. Selvikvåg Lundervold, A. and A. Lundervold, *An overview of deep learning in medical imaging focusing on MRI*. Zeitschrift für Medizinische Physik, 2018.
31. Krizhevsky, A., I. Sutskever, and G.E. Hinton, *ImageNet classification with deep convolutional neural networks*, in *Proceedings of the 25th International Conference on Neural Information Processing Systems - Volume 1*. 2012, Curran Associates Inc.: Lake Tahoe, Nevada. p. 1097-1105.
32. Kamnitsas, K., et al., *Efficient multi-scale 3D CNN with fully connected CRF for accurate brain lesion segmentation*. Med Image Anal, 2017. **36**: p. 61-78.
33. Prason, A., Petersen, K. , Igel, C. , Lauze, F. , Dam, E. , Nielsen, M. , *Deep feature learning for knee cartilage segmentation using a triplanar convolutional neural network*, in *Medical Image Computing and Computer-Assisted Intervention–MICCAI*. 2013, Springer.
34. Roth, H.R., Lu, L. , Seff, A. , Cherry, K.M. , Hoffman, J. , Wang, S. , Liu, J. , Turkbey, E. , Summers, R.M., *A new 2.5D representation for lymph node detection using random sets of deep convolutional neural network observations*, in *Medical Image Computing and Computer-Assisted Intervention–MICCAI*. 2014, Springer.
35. Li, R., Zhang, W. , Suk, H.-I. , Wang, L. , Li, J. , Shen, D. , Ji, S., *Deep learning based imaging data completion for improved brain disease diagnosis*, in *Medical Image Computing and Computer-Assisted Intervention–MICCAI*. 2014, Springer.
36. Khezri, M. and M. Jahed, *A Neuro–Fuzzy Inference System for sEMG-Based Identification of Hand Motion Commands*. IEEE Transactions on Industrial Electronics, 2011. **58**(5): p. 1952-1960.
37. Nazmi, N., et al., *A Review of Classification Techniques of EMG Signals during Isotonic and Isometric Contractions*. Sensors (Basel), 2016. **16**(8).

38. Reaz, M., M. Hussain, and F. Mohd-Yasin, *Techniques of EMG signal analysis: detection, processing, classification and applications*. Biological Procedures Online, 2006. **8**: p. 11-35.
39. Li, X., P. Zhou, and A. Aruin, *Teager–Kaiser Energy Operation of Surface EMG Improves Muscle Activity Onset Detection*. Annals of biomedical engineering, 2007. **35**: p. 1532-1538.
40. Solnik, S., et al., *Teager–Kaiser energy operator signal conditioning improves EMG onset detection*. Eur J Appl Physiol, 2010. **110**: p. 489–498.
41. Solnik, S., et al., *Teager–Kaiser Operator improves the accuracy of EMG onset detection independent of signal-to-noise ratio*. Acta Bioeng Biomech, 2008. **10**: p. 65-68.
42. Azzerboni, B., et al., *A New Approach to Detection of Muscle Activation by Independent Component Analysis and Wavelet Transform*, in *13th Italian Workshop on Neural Nets*. 2002, Springer Berlin Heidelberg. p. 109-116.
43. Liu, J., et al., *Robust Muscle Activity Onset Detection Using an Unsupervised Electromyogram Learning Framework*. PLoS One, 2015. **10**: p. e0127990.
44. Abdallah, S. and M. Plumbley. *Unsupervised onset detection: a probabilistic approach using ICA and a hidden Markov classifier*. in *Proceedings of the Cambridge Music Processing Colloquium*. 2003.
45. Staude, G. and W. Wolf, *Objective motor response onset detection in surface myoelectric signals*. Med Eng Phys, 1999. **21**: p. 449–467.
46. Basseville, M. and I. Nikiforov, *Detection of abrupt changes: theory and application*. 1993, Upper Saddle River, NJ, USA: Prentice-Hall.
47. Kleissen, R.F., et al., *Electromyography in the biomechanical analysis of human movement and its clinical application*. Gait Posture, 1998. **8**(2): p. 143-158.
48. Laterza, F.O., G., *Analysis of EMG signals by means of the matched wavelet transform*. Electron. Lett., 1997. **33**: p. 357–359.
49. Al-Mulla, M.R., F. Sepulveda, and M. Colley, *A review of non-invasive techniques to detect and predict localised muscle fatigue*. Sensors (Basel), 2011. **11**(4): p. 3545-94.
50. Kumar, D.K.P., N.D.; Bradley, A., *Wavelet analysis of surface electromyography to determine muscle fatigue*. IEEE Trans. Neural Syst. Rehabil. Eng., 2003. **11**: p. 400–406.

51. Al-Mulla, M.R., F. Sepulveda, and M. Colley, *Evolved pseudo-wavelet function to optimally decompose sEMG for automated classification of localized muscle fatigue*. Med Eng Phys, 2011. **33**(4): p. 411-7.
52. Karlsson, S., J. Yu, and M. Akay, *Time-frequency analysis of myoelectric signals during dynamic contractions: a comparative study*. IEEE Trans Biomed Eng, 2000. **47**(2): p. 228-38.
53. Karlsson, J.S., B. Gerdle, and M. Akay, *Analyzing surface myoelectric signals recorded during isokinetic contractions*. IEEE Eng Med Biol Mag, 2001. **20**(6): p. 97-105.
54. Subasi, A., *Classification of EMG signals using PSO optimized SVM for diagnosis of neuromuscular disorders*. Comput Biol Med, 2013. **43**(5): p. 576-86.
55. Rogers, D.R. and D.T. MacIsaac, *A comparison of EMG-based muscle fatigue assessments during dynamic contractions*. J Electromyogr Kinesiol, 2013. **23**(5): p. 1004-11.
56. Rechy-Ramirez, E.J. and H. Hu, *Bio-signal based control in assistive robots: a survey*. Digital Communications and Networks, 2015. **1**(2): p. 85-101.
57. Yan, T., et al., *Review of assistive strategies in powered lower-limb orthoses and exoskeletons*. Robotics and Autonomous Systems, 2015. **64**: p. 120-136.
58. Englehart, K., et al., *Classification of the myoelectric signal using time-frequency based representations*. Med Eng Phys, 1999. **21**(6-7): p. 431-8.
59. Asghari Oskoei, M. and H. Hu, *Myoelectric control systems—A survey*. Biomedical Signal Processing and Control, 2007. **2**(4): p. 275-294.
60. Khushaba, R. and A. Al-Jumaily, *Fuzzy Wavelet Packet Based Feature Extraction Method for Multifunction Myoelectric Control*. Vol. 2. 2007.
61. Hiraizumi, Y., E. Fujimaki, and T. Tachikawa, *Long-term morphology of spastic or flaccid muscles in spinal cord-transected rabbits*. Clin Orthop Relat Res, 1990(260): p. 287-96.
62. Durozard, D., C. Gabrielle, and G. Baverel, *Metabolism of rat skeletal muscle after spinal cord transection*. Muscle Nerve, 2000. **23**(10): p. 1561-8.
63. Landry, E., J. Frenette, and P.A. Guertin, *Body weight, limb size, and muscular properties of early paraplegic mice*. J Neurotrauma, 2004. **21**(8): p. 1008-16.
64. Shah, P.K., et al., *Lower-extremity muscle cross-sectional area after incomplete spinal cord injury*. Arch Phys Med Rehabil, 2006. **87**(6): p. 772-8.

65. Gorgey, A. and G. Dudley, *Skeletal muscle atrophy and increased intramuscular fat after incomplete spinal cord injury*. Spinal Cord, 2007. **45**: p. 304–309.
66. Nery, M., S. Driver, and K. Vanderbom, *Systematic Framework to Classify the Status of Research on Spinal Cord Injury and Physical Activity*. Archives of Physical Medicine and Rehabilitation, 2013. **94**(10): p. 2027-2031.
67. Shields, R.K., *Fatigability, relaxation properties, and electromyographic responses of the human paralyzed soleus muscle*. J Neurophysiol, 1995. **73**(6): p. 2195-206.
68. Shields, R.K., *Muscular, skeletal, and neural adaptations following spinal cord injury*. J Orthop Sports Phys Ther, 2002. **32**(2): p. 65-74.
69. Gorgey, A.S., et al., *The effects of electrical stimulation on body composition and metabolic profile after spinal cord injury – Part II*. The Journal of Spinal Cord Medicine, 2015. **38**(1): p. 23-37.
70. Gorgey, A.S., et al., *Neuromuscular electrical stimulation attenuates thigh skeletal muscles atrophy but not trunk muscles after spinal cord injury*. Journal of Electromyography and Kinesiology, 2013: p. 977–984.
71. Schick, F., *Tissue segmentation: a crucial tool for quantitative MRI and visualization of anatomical structures*. Magn Reson Mater Phys Biol Med., 2016. **29**(2): p. 89–93.
72. Gorgey, A.S. and G.A. Dudley, *Spasticity may defend skeletal muscle size and composition after incomplete spinal cord injury*. Spinal Cord, 2008. **46**(2): p. 96-102.
73. Barra, V., et al. *Automatic assessment of muscle/fat temporal variations on MR images of the thigh*. in *Proceedings of 18th Annual International Conference of the IEEE Engineering in Medicine and Biology Society*. 1996. Amsterdam.
74. Barra, V. and J. Boire, *Segmentation of fat and muscle from MR images of the thigh by a possibilistic clustering algorithm*. Computer Methods and Programs in Biomedicine, 2002. **68**(3): p. 185-193.
75. Positano, V., et al., *Accurate Segmentation of Subcutaneous and Intermuscular Adipose Tissue From MR Images of the Thigh*. JOURNAL OF MAGNETIC RESONANCE IMAGING, 2009(29): p. 677–684.
76. Andrews, S. and G. Hamarneh, *The Generalized Log-Ratio Transformation: Learning Shape and Adjacency Priors for Simultaneous Thigh Muscle Segmentation*. IEEE TRANSACTIONS ON MEDICAL IMAGING, 2015. **34**(9): p. 1773-1787.

77. Baudin, P.Y., et al. *Prior knowledge, random walks and human skeletal muscle segmentation*. in *MICCAI*. 2012. Springer.
78. Baudin, P., et al. *Discriminative Parameter Estimation for Random Walks Segmentation*. in *Medical Image Computing and Computer-Assisted Intervention (MICCAI)*. 2013. Springer.
79. Ahmad, E., et al. *Atlas-registration based image segmentation of MRI human thigh muscle in 3-D space*. in *Proceedings of SPIE*. 2014. The International Society for Optical Engineering.
80. Le Troter, A., et al., *Volume measurements of individual muscles in human quadriceps femoris using atlas-based segmentation approaches*. *J of Magn Reson MAtter Phy*, 2016. **29**: p. 245–257.
81. Fatehi, F., et al., *Long-term follow-up of MRI changes in thigh muscles of patients with Facioscapulohumeral dystrophy: A quantitative study*. *PLoS ONE* 2017. **12**(8).
82. Kemnitz, J., et al., *Validation of an active shape model-based semi-automated segmentation algorithm for the analysis of thigh muscle and adipose tissue cross-sectional areas*. *Magn Reson Mater Phy*, 2017. **30**: p. 489–503.
83. Hinton, G.E., Srivastava, N., Krizhevsky, A., Sutskever, I., Salakhutdinov, *Improving neural networks by preventing co-adaptation of feature detectors*. arXiv, 2012.
84. Deniz, C.M., et al., *Segmentation of the Proximal Femur from MR Images using Deep Convolutional Neural Networks*. *Scientific Reports*, 2018. **8**(1): p. 16485.
85. Liu, F., et al., *Deep convolutional neural network and 3D deformable approach for tissue segmentation in musculoskeletal magnetic resonance imaging*. *Magn Reson Med*, 2018. **79**(4): p. 2379-2391.
86. Norman, B., V. Pedoia, and S. Majumdar, *Use of 2D U-Net Convolutional Neural Networks for Automated Cartilage and Meniscus Segmentation of Knee MR Imaging Data to Determine Relaxometry and Morphometry*. *Radiology*, 2018. **288**(1): p. 177-185.
87. Waring, W.P., 3rd, et al., *_ 2009 review and revisions of the international standards for the neurological classification of spinal cord injury*. *J Spinal Cord Med*, 2010. **33**(4): p. 346-52.
88. Farag, A., A. El-baz, and G. Gimelfarb, *Precise segmentation of multi-modal images*. *IEEE Trans. Image Process.*, 2006. **15**(4): p. 952-968.

89. Glocker, B., et al., *Deformable medical image registration: Setting the state of the art with discrete methods*. Annual Review of Biomedical Engineering, 2011. **13**: p. 219-244.
90. El-Baz, A., G. Gimel'farb, and J.S. Suri, *Stochastic Modeling for Medical Image Analysis*. 2016: Taylor & Francis, ISBN.
91. Khalifa, F., et al., *Accurate automatic analysis of cardiac cine images*. IEEE Trans Biomed Eng, 2012. **59**(2): p. 445-55.
92. Dice, L.R., *Measures of the Amount of Ecologic Association Between Species*. Ecology, 1945. **26**(3): p. 297-302.
93. Huttenlocher, D.P. and W.J. Rucklidge. *A multi-resolution technique for comparing images using the Hausdorff distance*. in *Proceedings of IEEE Conference on Computer Vision and Pattern Recognition*. 1993.
94. Avants, B.B., et al., *A reproducible evaluation of ANTs similarity metric performance in brain image registration*. Neuroimage, 2011. **54**(3): p. 2033-44.
95. Akhondi-Asl, A. and S.K. Warfield, *Simultaneous truth and performance level estimation through fusion of probabilistic segmentations*. IEEE Trans Med Imaging, 2013. **32**(10): p. 1840-52.
96. Warfield, S.K., K.H. Zou, and W.M. Wells, *Simultaneous truth and performance level estimation (STAPLE): an algorithm for the validation of image segmentation*. IEEE Transactions on Medical Imaging, 2004. **23**(7): p. 903-921.
97. Konstantinos Kamnitsas, L.C., Christian Ledig, Daniel Rueckert, Ben Glocker. *Multi-Scale 3D Convolutional Neural Networks for Lesion Segmentation in Brain MRI*. in *ISLES-MICCA*. 2015.
98. Ogawa, M., et al., *Quantification of intermuscular and intramuscular adipose tissue using magnetic resonance imaging after neurodegenerative disorders*. Neural Regen Res, 2017. **12**(12): p. 2100-2105.
99. Imamoglu, N., et al. *Unsupervised muscle region extraction by fuzzy decision based saliency feature integration on thigh MRI for 3D modeling*. in *2015 14th IAPR International Conference on Machine Vision Applications (MVA)*. 2015.
100. Kovacs, W., et al. *Identification of muscle and subcutaneous and intermuscular adipose tissue on thigh MRI of muscular dystrophy*. in *2016 IEEE 13th International Symposium on Biomedical Imaging (ISBI)*. 2016.
101. Irmakci, I., et al., *A Novel Extension to Fuzzy Connectivity for Body Composition Analysis: Applications in Thigh, Brain, and Whole Body Tissue Segmentation*. IEEE Trans Biomed Eng, 2018.

102. Ogier, A., et al. *Individual muscle segmentation in MR images: A 3D propagation through 2D non-linear registration approaches*. in *39th Annual International Conference of the IEEE Engineering in Medicine and Biology Society (EMBC)*. 2017.
103. Garrow, J.S. and J. Webster, *Quetelet's index (W/H²) as a measure of fatness*. *Int J Obes*, 1985. **9**(2): p. 147-53.
104. Shin, H.C., et al., *Deep Convolutional Neural Networks for Computer-Aided Detection: CNN Architectures, Dataset Characteristics and Transfer Learning*. *IEEE Trans Med Imaging*, 2016. **35**(5): p. 1285-98.
105. Elder, C., et al., *Intramuscular fat and glucose tolerance after spinal cord injury – a cross-sectional study*. *Spinal Cord*, 2004: p. 711–716.
106. Addison, O., et al., *Intermuscular fat: a review of the consequences and causes*. *Int J Endocrinol*, 2014. **2014**: p. 309570.
107. Ichiyama, R.M., et al., *Step Training Reinforces Specific Spinal Locomotor Circuitry in Adult Spinal Rats*. *The Journal of Neuroscience*, 2008: p. 7370-7375.
108. Courtine, G., et al., *Transformation of nonfunctional spinal circuits into functional states after the loss of brain input*. *Nature Neuroscience*, 2009: p. 1333 - 1342.
109. Sayenko, D., et al., *Neuromodulation of evoked muscle potentials induced by epidural spinal cord stimulation in paralyzed individuals*. *journal of neurophysiology*, 2014. **111**: p. 5, 1088-1099.
110. Staude, G., et al., *Onset detection in surface electromyographic signals: a systematic comparison of methods*. *EURASIP Journal of Applied Signal Processing*, 2001. **2001**(1): p. 67-81.
111. Bouman, C. and K. Sauer, *A Generalized Gaussian Image Model for Edge-Preserving MAP Estimation*. *IEEE Transactions On Image Processing*, 1993. **2**(3): p. 1057-7149.
112. Mulder, R., J. Rucklidge, and S. Wilkinson, *Why has increased provision of psychiatric treatment not reduced the prevalence of mental disorder?* *Aust N Z J Psychiatry*, 2017. **51**(12): p. 1176-1177.
113. Khalifa, F., et al., *Accurate Automatic Analysis of Cardiac Cine Images*. *IEEE TRANSACTIONS ON BIOMEDICAL ENGINEERING*, 2012. **59**: p. 445-455.
114. Davison, A. and D. Hinkley, *Bootstrap Methods and Their Application*. 1997, Cambridge: Cambridge University Press.

115. Indrayan, A. and R. Chawla, *Clinical agreement in quantitative measurements*. Natl Med J India, 1994. **7**(5): p. 229-34.
116. Rejc, E., C. Angeli, and S. Harkema, *Effects of Lumbosacral Spinal Cord Epidural Stimulation for Standing after Chronic Complete Paralysis in Humans*. PLoS One, 2015. **10**(7): p. e0133998.
117. Angeli, C.A., et al., *Recovery of Over-Ground Walking after Chronic Motor Complete Spinal Cord Injury*. N Engl J Med, 2018. **379**(13): p. 1244-1250.
118. Mesbah, S.S., A; Stills, S; Soliman, A; Willhite, A; Harkema, S; Rejc, E; El-baz, A.; *A Novel Automatic Segmentation Method to Quantify the Effects of Spinal Cord Injury on Human Thigh Muscles and Adipose Tissue.*, in *Medical Image Computing and Computer-Assisted Intervention – MICCAI 2017*, M.-H.L. Descoteaux M., Franz A., Jannin P., Collins D., Duchesne S. , Editor. 2017, Lecture Notes in Computer Science, Springer.
119. Graham, R.B., M.P. Wachowiak, and B.J. Gurd, *The Assessment of Muscular Effort, Fatigue, and Physiological Adaptation Using EMG and Wavelet Analysis*. PLOS ONE, 2015. **10**(8): p. e0135069.
120. Reaz, M.B., M.S. Hussain, and F. Mohd-Yasin, *Techniques of EMG signal analysis: detection, processing, classification and applications (Correction)*. Biol Proced Online, 2006. **8**: p. 163.
121. Oppenheim, A.V., Ronald W. Schaffer, John R. Buck, *Discrete-Time Signal Processing*. Second Edition ed. 1999, Upper Saddle River, NJ: Prentice Hall.
122. Berry, M.W., et al., *Algorithms and applications for approximate nonnegative matrix factorization*. Computational Statistics & Data Analysis, 2007. **52**(1): p. 155-173.
123. Glantz, S. and B. Slinker, *Primer of Applied Regression & Analysis of Variance*. 2000: McGraw-Hill Education.
124. Mitchell, T.M., *Machine Learning*. 1997: McGraw-Hill, Inc. 432.
125. Hastie, T., R. Tibshirani, and J. Friedman, *The Elements of Statistical Learning*. Second Edition ed. 2008, NY: Springer.
126. Scholkopf, B., and A. Smola, *Learning with Kernels: Support Vector Machines, Regularization, Optimization and Beyond, Adaptive Computation and Machine Learning*. 2002, Cambridge, MA: The MIT Press.
127. Friedman, J.H., Trevor; Tibshirani, Robert, *Additive logistic regression: a statistical view of boosting* Ann. Statist, 2000. **28**(2): p. 337-407.

128. Snoek, J., H. Larochelle, and R.P. Adams, *Practical Bayesian optimization of machine learning algorithms*, in *Proceedings of the 25th International Conference on Neural Information Processing Systems - Volume 2*. 2012, Curran Associates Inc.: Lake Tahoe, Nevada. p. 2951-2959.
129. MATLAB(R2017b), *Statistics and Machine Learning Toolbox*. Natick, Massachusetts: The MathWorks, Inc.
130. De Luca, C.J., *Use of the surface EMG signal for performance evaluation of back muscles*. Muscle Nerve, 1993. **16**(2): p. 210-6.
131. Arendt-Nielsen, L. and M. Zwarts, *Measurement of muscle fiber conduction velocity in humans: techniques and applications*. J Clin Neurophysiol, 1989. **6**(2): p. 173-90.
132. Solomonow, M., et al., *Electromyogram power spectra frequencies associated with motor unit recruitment strategies*. J Appl Physiol (1985), 1990. **68**(3): p. 1177-85.
133. Allison, G.T. and T. Fujiwara, *The relationship between EMG median frequency and low frequency band amplitude changes at different levels of muscle capacity*. Clin Biomech (Bristol, Avon), 2002. **17**(6): p. 464-9.
134. Farina, D., M. Fosci, and R. Merletti, *Motor unit recruitment strategies investigated by surface EMG variables*. J Appl Physiol (1985), 2002. **92**(1): p. 235-47.
135. Farina, D., R. Merletti, and R.M. Enoka, *The extraction of neural strategies from the surface EMG: an update*. J Appl Physiol (1985), 2014. **117**(11): p. 1215-30.
136. De Luca, C.J. and E.C. Hostage, *Relationship between firing rate and recruitment threshold of motoneurons in voluntary isometric contractions*. J Neurophysiol, 2010. **104**(2): p. 1034-46.
137. Gerasimenko, Y., R.R. Roy, and V.R. Edgerton, *Epidural stimulation: comparison of the spinal circuits that generate and control locomotion in rats, cats and humans*. Exp.Neurol., 2008. **209**(2): p. 417-425.
138. Merletti, R.P., PA., *Electromyography: Physiology, Engineering and Non-Invasive Applications*. 2004, New York, NY, USA: John Wiley and sons, Inc.
139. Grahn, P.J., et al., *Enabling Task-Specific Volitional Motor Functions via Spinal Cord Neuromodulation in a Human With Paraplegia*. Mayo Clin Proc, 2017. **92**(4): p. 544-554.
140. Sayenko, D., et al., *Self-assisted standing enabled by non-invasive spinal stimulation after spinal cord injury*. J Neurotrauma, 2018.

141. Farina, D., et al., *Principles of Motor Unit Physiology Evolve With Advances in Technology*. Physiology (Bethesda), 2016. **31**(2): p. 83-94.
142. Gaunt, R.A., et al., *Intraspinal microstimulation excites multisegmental sensory afferents at lower stimulus levels than local alpha-motoneuron responses*. Journal of Neurophysiology, 2006. **96**(6): p. 2995-3005.
143. Gerasimenko, Y.P., et al., *Spinal cord reflexes induced by epidural spinal cord stimulation in normal awake rats*. J Neurosci.Methods., 2006. .
144. Musienko, P., et al., *Multi-system neurorehabilitative strategies to restore motor functions following severe spinal cord injury*. Exp Neurol, 2012. **235**(1): p. 100-9.
145. Hofstoetter, U.S., et al., *Periodic modulation of repetitively elicited monosynaptic reflexes of the human lumbosacral spinal cord*. J Neurophysiol, 2015. **114**(1): p. 400-10.
146. Danner, S.M., et al., *Human spinal locomotor control is based on flexibly organized burst generators*. Brain, 2015. **138**(Pt 3): p. 577-88.
147. Wenger, N., et al., *Spatiotemporal neuromodulation therapies engaging muscle synergies improve motor control after spinal cord injury*. Nat Med, 2016. **22**(2): p. 138-45.
148. Moraud, E.M., et al., *Mechanisms Underlying the Neuromodulation of Spinal Circuits for Correcting Gait and Balance Deficits after Spinal Cord Injury*. Neuron, 2016. **89**(4): p. 814-28.
149. Rattay, F., K. Minassian, and M.R. Dimitrijevic, *Epidural electrical stimulation of posterior structures of the human lumbosacral cord: 2. quantitative analysis by computer modeling*. Spinal Cord, 2000. **38**: p. 473-489.
150. Capogrosso, M., et al., *A computational model for epidural electrical stimulation of spinal sensorimotor circuits*. J.Neurosci., 2013. **33**(49): p. 19326-19340.
151. Gad, P., et al., *Development of a multi-electrode array for spinal cord epidural stimulation to facilitate stepping and standing after a complete spinal cord injury in adult rats*. J.Neuroeng.Rehabil., 2013. **10**: p. 2.
152. Jilge, B., et al., *Initiating extension of the lower limbs in subjects with complete spinal cord injury by epidural lumbar cord stimulation*. Exp.Brain Res., 2004. **154**(3): p. 308-326.
153. Minassian, K., et al., *Stepping-like movements in humans with complete spinal cord injury induced by epidural stimulation of the lumbar cord: electromyographic study of compound muscle action potentials*. Spinal Cord., 2004. **42**(7): p. 401-416.

154. Jilge, B., et al., *Frequency-dependent selection of alternative spinal pathways with common periodic sensory input*. Biol.Cybernetics, 2004. **91**: p. 359-376.
155. Beauparlant, J., et al., *Undirected compensatory plasticity contributes to neuronal dysfunction after severe spinal cord injury*. Brain, 2013. **136**(Pt 11): p. 3347-61.
156. Hiersemenzel, L.P., A. Curt, and V. Dietz, *From spinal shock to spasticity: neuronal adaptations to a spinal cord injury*. Neurology, 2000. **54**(8): p. 1574-1582.
157. Wagner, F.B., et al., *Targeted neurotechnology restores walking in humans with spinal cord injury*. Nature, 2018. **563**(7729): p. 65-71.
158. Sayenko, D.G., et al., *Neuromodulation of evoked muscle potentials induced by epidural spinal-cord stimulation in paralyzed individuals*. J Neurophysiol, 2014. **111**(5): p. 1088-99.
159. Mesbah, S., et al., *A novel approach for automatic visualization and activation detection of evoked potentials induced by epidural spinal cord stimulation in individuals with spinal cord injury*. PloS one, 2017. **12**(10): p. e0185582.

CURRICULUM VITAE

FULL NAME

Samineh Mesbah



PERSONAL INFORMATION

Nationality: Iranian.

Date of Birth: September 21, 1987.

Place of Birth: Iran.

Home Address: 4103 Waterford Circle Apt 03,
Louisville, KY, 40207, USA

Phone: +1 (917) 327-8822

E-mail: samineh.mesbah@louisville.edu

Homepage: <https://www.linkedin.com/in/samineh-mesbah-49474859/>

EDUCATION

• **Ph.D.**, Electrical and Computer Engineering, University of Louisville, KY, USA,

Expected graduation date: Spring 2019.

Thesis: Signal and Image-based Machine Learning Systems for Assessments of Spinal Cord Injury and Treatment Interventions.

Supervisor: Prof. Ayman El-baz.

GPA: 3.86.

- **M.Sc.**, Biomedical Engineering, Majoring in Bioelectronics, Tehran Polytechnic, Tehran, Iran, 2014

Thesis: Dynamical Analysis and Feedback Control Design of Synchronization in Oscillatory Neuronal Systems for Modeling Parkinson Disease.

Supervisors: Prof. Farzad Towhidkhah, Dr. Shahriar Gharibzadeh.

GPA: 18.61/20.

- **B.Sc.**, Electrical Engineering, Majoring in Control Systems, Ferdowsi University of Mashhad, Mashhad, Iran, 2010.

GPA: 15.16/20.

PROFESSIONAL AND WORK EXPERIENCE

- Kentucky Spinal Cord Research Center, Research Assistant, Jan 2015-present.

- BioImaging Lab, Bioengineering Department, University of Louisville, Research Assistant, Sept. 2014-Jan. 2015

- Polytechnic Biological Systems Modeling Lab, Research Assistant, Oct. 2011 – May 2014.

- Parto Electronic Toos Internship, Electrical Engineer Intern, May 2008 – Aug. 2008.

JOURNAL PUBLICATIONS

- **Samineh Mesbah**, Federica Gonnelli, Claudia Angeli, Ayman El-Baz, Susan Harkema, Enrico Rejc. Neurophysiological Markers Predicting Recovery of Standing in Humans with Chronic Motor Complete Spinal Cord Injury, Nature Communications, Under review.

- **Samineh Mesbah**, Ahmed Shalaby, Sean Stills, Ahmed Soliman, Andrea Willhite, Susan Harkema, Enrico Rejc, Ayman El-baz. Novel Stochastic Framework for Automatic

Segmentation of Human Thigh MRI Volumes and Its Application in Quantification of the Effects of Spinal Cord Injury, PLoS ONE, Accepted.

• **Samineh Mesbah**; Claudia Angeli; Robert Keynton; Susan Harkema; Ayman El-baz. A Novel Approach for Automatic Visualization and Activation Detection of Evoked Potentials Induced by Epidural Spinal Cord Stimulation in Individuals with Spinal Cord Injury, PLoS ONE 12(10): e0185582. <https://doi.org/10.1371/journal.pone.0185582>

• **Samineh Mesbah**, Andrew Switala, Claudia A. Angeli, Enrico Rejc, Ayman El-baz, Susan J. Harkema. Repeatability Measurements for Epidurally Induced Motor Evoked Potentials in Individuals with Spinal Cord Injury, Journal of Electromyography and Kinesiology, Under review.

• **Samineh Mesbah**, Motahareh Moghtadaei, Mohammad Reza Hashemi Golpayegani, Farzad Towhidkhan, Onedimensional Map-based Neuron Model: A Logistic Modification, Journal of Chaos, Solitons and Fractals, Apr. 2014, 10.1016/j.chaos.2014.04.006.

• **Samineh Mesbah**, Shahriar Gharibzadeh, Farzad Towhidkhan, Using Brain Network Graph Modeling to Explore the Cause of Non-Motor Symptoms in Parkinsons Disease, The Journal of Neuropsychiatry and Clinical Neurosciences, 2013; 25:E60-E60.

• Hisham Abdeltawab, Mohamed Shehata, Fahmi Khalifa, Ahmed Shalaby, **Samineh Mesbah**, Mohamed Abou-Elghar, Amy Dwyer, Moumen El-Melegy, Ayman Elbaz, "A Novel CNN-based CAD System for Early Assessment of Transplanted Kidney Dysfunction", Scientific Reports, Under review.

CONFERENCE PUBLICATIONS

• **Samineh Mesbah**, Federica Gonnelli, Claudia Angeli, Ayman El-Baz, Susan Harkema, Enrico Rejc. Spectral Analysis of Lower Limb EMG Activity in Individuals with Motor Complete SCI during Standing with Epidural Stimulation, ISSPIT Conference 2018.

• **Samineh Mesbah**; Ahmed Shalaby; Andrea Willhite; Enrico Rejc; Susan Harkema; Ayman El-baz. Automatic 3-D Muscle and Fat Segmentation of Thigh MRI Volumes in Individuals with Spinal Cord Injury, ICIP Conference 2017.

• **Samineh Mesbah**; Ahmed Shalaby; Andrea Willhite; Sean Stills, Enrico Rejc; Susan Harkema; Ayman El-baz. A Novel Automatic Segmentation Method to Quantify the Effects of Spinal Cord Injury on Human Thigh Muscles and Adipose Tissue, In: Descoteaux M., Maier-Hein L., Franz A., Jannin P., Collins D., Duchesne S. (eds) Medical Image Computing and Computer-Assisted Intervention (MICCAI) 2017 Lecture Notes in Computer Science, vol 10434. Springer, Cham.

• Hisham Abdeltawab, Mohamed Shehata, Ahmed Shalaby, **Samineh Mesbah**, Maryam El-Baz, Mohammed Ghazal, Yasmina Al Khalil, Mohamed Abou El-Ghar, Amy C. Dwyer, Moumen El-Melegy, and Ayman El-Baz, A New 3D CNN-based CAD System for Early Detection of Acute Renal Transplant Rejection”, ICPR 2018

• Heba Kandil, Ahmed Soliman, Guruprasad Giridharan, **Samineh Mesbah**, Ali Mahmoud, Ahmed Shalaby, Mohammed Ghazal, Adel Elmaghraby, Ayman El-Baz A Novel MRA-Based Framework for Detecting Correlation Between Cerebrovascular Changes and Mean Arterial Pressure), 2018 IEEE International Conference on Imaging Systems and Techniques (IST).

POSTER AND ORAL PRESENTATIONS

• **Samineh Mesbah**, Federica Gonnelli, Claudia Angeli, Ayman El-Baz, Susan Harkema, Enrico Rejc. Spectral Analysis of Lower Limb EMG Activity in Individuals with Motor Complete SCI during Standing with Epidural Stimulation, ISSPIT 2018, Oral Presentation.

• **Samineh Mesbah**, Claudia Angeli, Robert Keynton, Ayman El-baz, Susan Harkema, A Novel Approach for Automatic Visualization and Activation Detection of Evoked Potentials Induced by Epidural Spinal Cord Stimulation in Individuals with Spinal Cord Injury, BMES 2018, Oral Presentation.

- **Samineh Mesbah**, Federica Gonnelli, Enrico Rejc, Susan Harkema, Ayman El-baz, Frequency Analysis of EMG Signals of Individuals with Spinal Cord Injury: Comparison Between FFT, STFT and Wavelet Methods, BMES 2018, Poster Presentation.
- **Samineh Mesbah**, Ahmad Shalaby, Susan Harkema, Enrico Rejc, Ayman El-baz, A Novel Automatic Segmentation Method to Quantify the Effects of Training Interventions on the Thigh Muscles and Adipose Tissue of Spinal Cord Injured Patients: A Case Study, Speed School Exposition 2018, Poster Presentation.
- **Samineh Mesbah**, Ahmad Shalaby, Susan Harkema, Enrico Rejc, Ayman El-baz, A Novel 3D Automatic Framework for Muscle and Fat Segmentation of Thigh MRI Volumes in SCI Subjects, BMES 2017, Poster Presentation.
- **Samineh Mesbah**, Ahmad Shalaby, Susan Harkema, Enrico Rejc, Ayman El-baz, A Novel Automatic Segmentation Method to Quantify the Effects of Training Interventions on the Thigh Muscles and Adipose Tissue of Spinal Cord Injured Patients: A Case Study, KSCHIRT Symposium 2017, Poster Presentation.
- **Samineh Mesbah**, Claudia Angeli, Robert Keynton, Ayman El-baz, Susan Harkema, A Novel Approach for Automatic Visualization and Activation Detection of Evoked Potentials Induced by Epidural Spinal Cord Stimulation in Individuals with Spinal Cord Injury, Research Louisville 2016, Poster Presentation.
- AN Herrity, CA Angeli, **S Mesbah**, SJ Harkema, CH Hubscher, Mapping with spinal cord epidural stimulation for bladder function after human spinal cord injury. SPARC Initiative: Translational Partnerships & New Indications, NIH SPARC Annual Awardee Meeting, April 5-7th 2018, Bethesda, MD, Poster Presentation.

BOOK CHAPTER

- A. Shalaby , A. Mahmoud, **S. Mesbah**, M. El-Baz, J. Suri and A. El-Baz, “Accurate Unsupervised 3D Segmentation of Blood Vessels using Magnetic Resonance

Angiography,” in Cardiovascular Imaging and Image Analysis, Taylor and Francis Group, 2018.

PATENTS

- S. Harkema, A.El-baz, C. Angeli, **S. Mesbah**, “Methods for Detecting and Mapping Spinal Cord Epidurally-evoked Potentials” U.S. Provisional Patent Application Serial No. 62/432,908, Jan 12, 2017.
- A. El-baz, S. Harkema, E. Rejc, **S. Mesbah**, A. Shalaby, “3-D Muscle/fat Segmentation Technology”, U.S. Provisional Patent Application Serial No. 62/596,941, December 11, 2017.

HONORS AND AWARDS

- The Winner of University of Louisville Speed School Exposition 2018 in Ph.D. Category.
- The Recipient of Electrical and Computer Engineering Department 2018 Outstanding Graduate Student Award at University of Louisville.
- The Recipient of Electrical and Computer Engineering Department 2018 Scholarship Theobald Award at University of Louisville.
- The Recipient of Ph.D. Scholarship from Kentucky Spinal Cord Research Center, 2015-present.
- Ranked 1st GPA Amongst Bioelectric Graduate Students Class of 2014 in Biomedical Engineering Department, Tehran Polytechnic University.

REFERENCES

Prof. Ayman El-baz, Bioengineering Department Chair, BioImaging Lab, University of Louisville, Louisville, KY. Ayman.elbaz@louisville.edu (502) 852-5092

Prof. Susan Harkema, Director of Kentucky Spinal Cord Injury Research Center, University of Louisville, Louisville, KY. SusanHarkema@KentuckyOneHealth.org (502) 852-8060